AFRL-RQ-WP-TR-2018-0161

BLUNT CONE, HIFiRE-1 AND HIFiRE-5 BOUNDARY LAYER TRANSITION

Roger Kimmel, David Adamczak, and Matthew Borg
Hypersonic Sciences Branch
High Speed Systems Division

Joseph S. Jewell
Spectral Energies, LLC

Matthew Tufts
Ohio Aerospace Institute

Richard Kennedy and Stuart Laurence
University of Maryland

JULY 2018
Interim Report

AIR FORCE RESEARCH LABORATORY
AEROSPACE SYSTEMS DIRECTORATE
WRIGHT-PATTERSON AIR FORCE BASE, OH 45433-7542
AIR FORCE MATERIEL COMMAND
UNITED STATES AIR FORCE

NOTICE AND SIGNATURE PAGE

AFRL-RQ-WP-TR-2018-0161 has been reviewed and is approved for publication in accordance with assigned distribution statement.

REPORT DOCUMENTATION PAGE

Form Approved
OMB No. 0704-0188

1. REPORT DATE ***(DD-MM-YY)*** July 2018	**2. REPORT TYPE** Interim	**3. DATES COVERED** ***(From - To)*** 01 July 2016 – 01 July 2018

4. TITLE AND SUBTITLE
BLUNT CONE, HIFiRE-1 AND HIFiRE-5 BOUNDARY LAYER TRANSITION

5a. CONTRACT NUMBER
In-house

5b. GRANT NUMBER

5c. PROGRAM ELEMENT NUMBER
61102F

6. AUTHOR(S)
Roger Kimmel, David Adamczak, and Matthew Borg (AFRL/RQHF)
Joseph S. Jewell (Spectral Energies, LLC)
Matthew Tufts (Ohio Aerospace Institute)
Richard Kennedy and Stuart Laurence (University of Maryland)

5d. PROJECT NUMBER
3002

5e. TASK NUMBER

5f. WORK UNIT NUMBER
Q1FN

7. PERFORMING ORGANIZATION NAME(S) AND ADDRESS(ES)

Hypersonic Sciences Branch (AFRL/RQHF)
High Speed Systems Division
Air Force Research Laboratory, Aerospace Systems Directorate
Wright-Patterson Air Force Base, OH 45433-7542
Air Force Materiel Command, United States Air Force

Spectral Energies, LLC
4065 Executive Dr
Beavercreek, OH 45430

Ohio Aerospace Institute
5100 Springfield St # 308
Beavercreek, OH 45431

University of Maryland
College Park, MD 20742

8. PERFORMING ORGANIZATION REPORT NUMBER
AFRL-RQ-WP-TR-2018-0161

9. SPONSORING/MONITORING AGENCY NAME(S) AND ADDRESS(ES)
Air Force Research Laboratory
Aerospace Systems Directorate
Wright-Patterson Air Force Base, OH 45433-7542
Air Force Materiel Command
United States Air Force

10. SPONSORING/MONITORING AGENCY ACRONYM(S)
AFRL/RQHF

11. SPONSORING/MONITORING AGENCY REPORT NUMBER(S)
AFRL-RQ-WP-TR-2018-0161

12. DISTRIBUTION/AVAILABILITY STATEMENT
DISTRIBUTION STATEMENT A. Approved for public release. Distribution is unlimited.

13. SUPPLEMENTARY NOTES
PA Clearance Number: 88ABW-2018-5344; Clearance Date: 24 October 2018

14. ABSTRACT

This interim technical report summarizes technical activity on AFRL 6.1 laboratory task LRIR 15RQCOR102 during fiscal year 2017. The objective of this task is to better understand boundary layer transition in hypersonic flowfields with spanwise nonuniformity. Several advances were made under this task during FY18. The HIFiRE-1 and -5b body of ground and flight data were further analyzed, producing some general recommendations on the prediction and ground test of hypersonic boundary layer transition. As a precursor to testing transition on the spanwise nonuniform boundary layer on a cone, the transition mechanisms for blunt cones were measured in the AFRL high Reynolds Mach 6 wind tunnel. These measurements are the first of their type made in this facility

15. SUBJECT TERMS
boundary layer transition, hypersonic, flight test

16. SECURITY CLASSIFICATION OF:			**17. LIMITATION OF ABSTRACT:**	**18. NUMBER OF PAGES**	**19a. NAME OF RESPONSIBLE PERSON** (Monitor)
a. REPORT	**b. ABSTRACT**	**c. THIS PAGE**			
Unclassified	Unclassified	Unclassified	SAR	76	Roger L. Kimmel **19b. TELEPHONE NUMBER** (Include Area Code) N/A

Section

List of Figures

List of Tables

Acknowledgments

This work was supported by the Air Force Office of Scientific Research under Laboratory Research Initiation Request 15RQCOR102. A very large number of organizations and people contributed to the HIFiRE-1 and -5 research programs. The authors wish to thank the AFRL Aerospace Systems Directorate and its precursor organizations, and Ivett Leyva and her predecessors at the Air Force Office of Scientific Research, including John Schmisseur and Pon Ponnapan for their sponsorship. Douglas Dolvin of the AFRL Aerospace Systems Directorate provided program management. Flight tests were executed by the Air Vehicles Division, Brisbane, of the Defence Science and Technology Organisation and the Defence Science and Technology Group, Royal Australia Navy Ranges and Assessing Unit, Aerospace Operational Support Group, Royal Australian Air Force, White Sands Missile Range, Kratos, and DLR Moraba. Ground test support and analysis was provided by the NASA Langley Research Center, Purdue University, Texas A&M University and CUBRC. Many individuals, too numerous to mention, provided valuable advice and feedback.

Joseph E. Wehrmeyer of AEDC generously arranged a loan of the Cavilux laser used in this work. The authors also thank Brian K.-Y. Lam, Jim Hayes, Servane Altman, and Benjamin Hagen of AFRL/RQVX for assistance running the Mach 6 High-Reynolds Facility. The authors also thank Dr. Ross Wagnild of Sandia for his patient advice on the use of the STABL code. A substantial portion of this research was performed while J. S. Jewell held a National Research Council Research Associateship Award at the Air Force Research Laboratory. R. E. Kennedy was supported by the National Defense Science and Engineering Graduate Fellowship.

1. Summary

This interim technical report summarizes technical activity on AFRL 6.1 laboratory task LRIR 15RQCOR102 during fiscal year 2017. The objective of this task is to better understand boundary layer transition in hypersonic flowfields with spanwise nonuniformity. Several advances were made under this task during FY18. The HIFiRE-1 and -5b body of ground and flight data were further analyzed, producing some general recommendations on the prediction and ground test of hypersonic boundary layer transition. As a precursor to testing transition on the spanwise nonuniform boundary layer on a cone, the transition mechanisms for blunt cones were measured in the AFRL high Reynolds Mach 6 wind tunnel. These measurements are the first of their type made in this facility. Sections 2, 3 and 4 were originally published as references [1, 2, 3].

2. HIFiRE-1 and -5 Flight and Ground Tests

2.1. HIFiRE-5b Flight Overview

The Hypersonic International Flight Research Experimentation (HIFiRE) program is a hypersonic flight test program executed by the Air Force Research Laboratory (AFRL) and the Australian Defence Science and Technology Organization (DSTO). [4, 5] Its purpose is to develop and validate technologies critical to next generation hypersonic aerospace systems. Candidate technology areas include, but are not limited to, propulsion, propulsion-airframe integration, aerodynamics and aerothermodynamics, high temperature materials and structures, thermal management strategies, guidance, navigation, and control, sensors, and system components. The HIFiRE program consists of extensive ground tests and computation focused on specific hypersonic flight technologies. Each technology program culminates in a flight test.

Two HIFiRE flights focused on boundary layer transition. HIFiRE-1 created an extensive knowledge base regarding transition on axisymmetric bodies that was summarized in numerous prior publications. [6-20] HIFiRE-5 was devoted to measuring transition on a three-dimensional (3D) body. The results of this flight were summarized in a number of technical papers. [21-26] Preflight research was described in numerous publications.[27-43]

Both HIFiRE transition flight experiments were successful, with some minor anomalies. HIFiRE-1 launched 22 March 2010 at the Woomera Prohibited Area in South Australia. This vehicle entered the atmosphere at higher-than-intended angle-of-attack, but was otherwise successful. Low angle-of-attack (AoA) hypersonic transition data were obtained on ascent, and high AoA transition was measured during descent. The HIFIRE-5a mission launched 23 April 2012 from Andoya, Norway.[44-47] The second stage of HIFiRE-5a failed to ignite, preventing the payload from attaining hypersonic speeds. Despite the failure of the HIFiRE-5a second stage, the payload acquired supersonic transition data. However, since this did not satisfy mission objectives to acquire hypersonic transition measurements, a new payload, essentially identical to the first, was constructed and flown at Woomera, Australia, on 18 May 2016. This mission, HIFiRE-5b, was entirely successful.

The HIFiRE-1 and -5 primary experimental objectives were to measure transition on smooth bodies in hypersonic flight. Although previous tests had measured transition during hypersonic flight tests, these tests were subject to some ambiguity due to surface roughness, as-flown nosetip geometry, vehicle motion, ablation, wall temperature and so on. Schneider provides a survey paper of previous hypersonic flight tests. [48] The HIFiRE goal was to remove this ambiguity by flying heavily-instrumented test articles with smooth, unablating moldlines. The singular flight test product that could not be derived from ground test was transition measurements in a quiet environment. Transition locations measured in flight would be converted to transition Reynolds numbers and *N*-factors, and compared to ground test results to assess the influence of wind tunnel noise, and to provide some calibration of *N*-factor prediction methods. Subsequent sections of this paper will demonstrate that this goal was achieved, and will summarize conclusions regarding ground test and computation that could be derived from the flight data.

The HIFiRE research program obtained data on numerous aspects of hypersonic transition, including roughness-dominated transition and the phenomenology of transition in flight. To limit the scope of this paper, only smooth-body results are discussed, with a focus on comparison to ground test and computation. The research campaign also contributed a huge amount of computational work. For brevity, discussion of computational results is limited to a few select computations that help elucidate the flight and ground transition results.

2.2. Flight Experiments Description

The HIFiRE-1 and -5 configurations were described in prior papers. [19, 44] Both configurations consisted of an instrumented test article mounted atop a two-stage, ground-launched sounding rocket. The payloads remained attached to the second stage throughout flight. The vehicles were spun at a low rate to reduce trajectory dispersion. Cant-angle on the first and second-stage fins caused the vehicles to spin passively. Because of this, the vehicles were rolling throughout the entire trajectory. Both flights were launched with high elevations and flew lofted, ballistic trajectories, with short endoatmospheric flight times, and with relatively long exoatmospheric stages and high exoatmospheric apogees. Data were obtained on ascent and descent, with descent being the primary test window.

Neither flight possessed active control surfaces on the upper stage, and relied solely on the static aerodynamic stability of the stack to maintain low angle-of-attack during ascent. During relevant ascent flight periods, angle-of-attack was less than 0.5°. On both flights, cold-gas thrusters were used during exoatmospheric flight to orient the vehicle along the descent flight path vector, in order to minimize angle of attack during descent. This maneuver was unsuccessful for HIFiRE-1, and the payload reentered the atmosphere at a relatively high angle of attack. The AoA damped in an oscillatory manner so that $5^\circ < \alpha < 13^\circ$ during descent transition. The HIFiRE-5b exoatmospheric thruster maneuver was successful, so that AoA during descent transition was less than 1°. Considerable effort was expended to ensure that the HIFiRE-1 and -5 instrumentation and post-flight analysis were able to resolve the effects of the vehicle motion.

The 7 ° half-angle cone geometry was chosen for HIFiRE-1 since this configuration had been the basis of extensive test and analysis for many years. The HIFiRE-5 configuration was chosen as the test-article geometry based on extensive previous testing and analysis on elliptic cones.[49-56] This prior work [49-51] demonstrated that the 2:1 elliptic cone would generate significant crossflow instability at hypersonic flight conditions and potentially exhibit leading-edge transition. Figure 1, taken from [19] and [21] illustrates the HIFiRE-1 and -5 geometries.

Both payloads consisted of aluminum frusta that served as the primary test surfaces, and had solid, uninstrumented nosetips built-up from several materials. To account for the differential coefficients of thermal expansion of the nosetip materials, the tips possessed backward-facing steps at each material interface when cold. The steps were sized to approach zero height when the nosetip was at working temperature in the test window during descent. The nosetips of both vehicles were slightly blunted. References describe the nosetip details and detailed surface roughness measurements. [13, 19, 21] For both HIFiRE-1 and -5, roughness did not demonstrably affect transition, and nose-bluntness effects were limited primarily to the first 300 mm of the test article.

The bulk of the instrumentation on both flights consisted of Medtherm coaxial thermocouples, hand-contoured to the outer mold line of the vehicle. The HIFiRE-1 test surface contained two rays of thermocouples. The secondary side of the vehicle possessed a diamond-shaped, discrete roughness element to assess tripped transition, and the primary side of the cone was smooth. The HIFiRE-5 configuration had one side that contained a closeout panel with fasteners. The primary test surface on the other side was smooth and devoid of fasteners. Ground tests verified on both vehicles that roughness-induced transition would not contaminate the test surface flow. Post flight analysis confirmed that this indeed was the case.

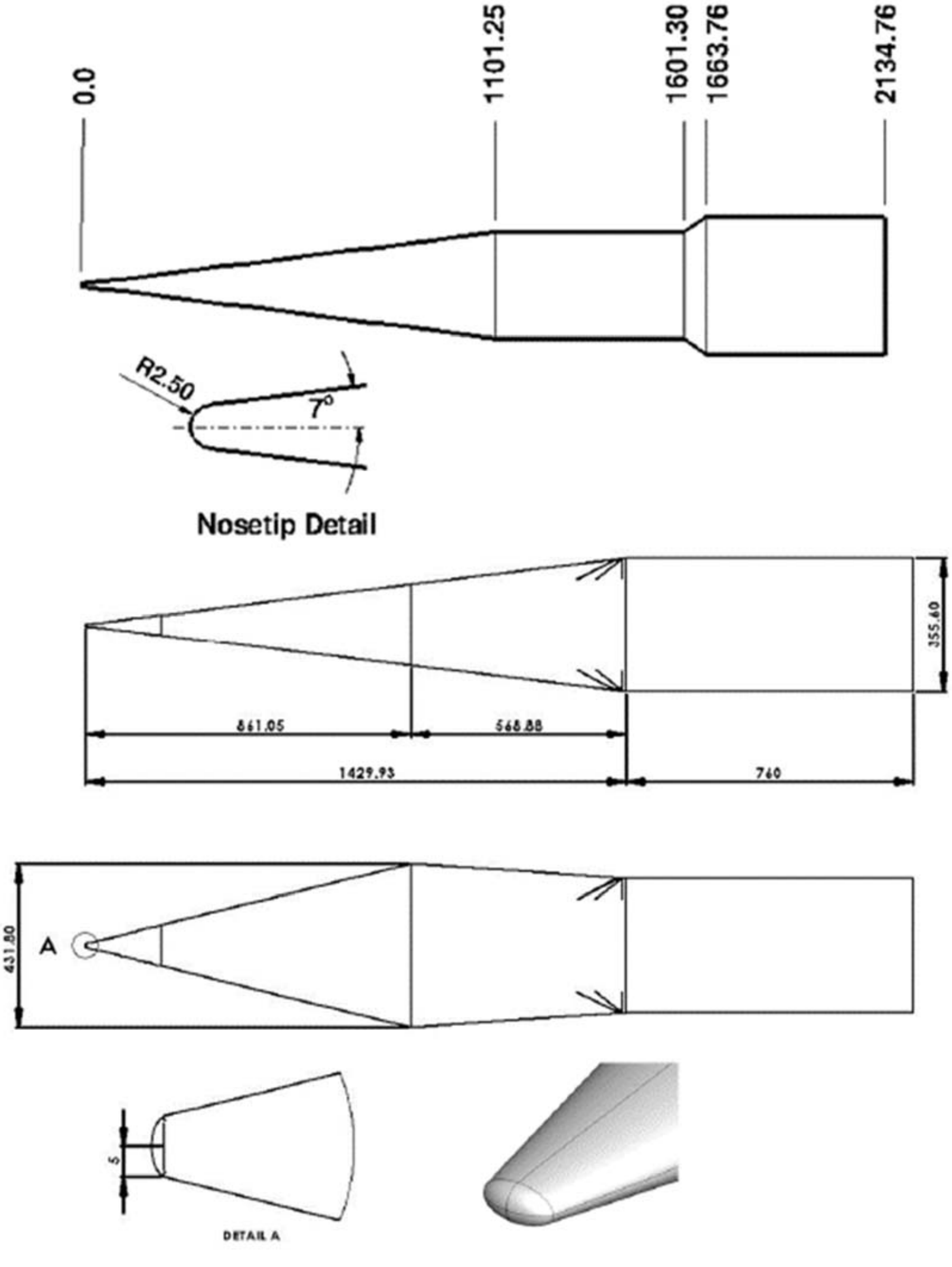

Figure 1 HIFiRE-1 (top, [19]) and HIFiRE-5 (bottom, [21]) flight vehicles. Dimensions mm.

2.3. Smooth-Body, Axisymmetric Transition – HIFiRE-1

HIFiRE-1 ascent phase transition is documented in detail in Kimmel et al. [19]. During ascent, flow over the HIFiRE-1 test article was turbulent immediately after launch. As the vehicle ascended, and Reynolds number dropped, transition moved aft over the vehicle. Ascent transition occurred in three phases. In phase one, for $t < 15$ s, roughness due to nosetip joint steps dominated transition. For $t > 15$ s, the combination of higher nose temperature, which reduced step heights, and lower Reynolds number and higher Mach number, which made the boundary layer less sensitive to roughness, lessened the influence of the steps. However, during phase two, $15 < t < 19$ s, nosetip roughness still appeared to affect transition somewhat, and transition behaved erratically. During phase three, $19 < t < 22$ s, transition on the primary test surface moved downstream in an orderly fashion, consistent with a smooth-body transition, with $10.4\times10^6 < \mathrm{Re}_x < 13.7\times10^6$ and free stream Mach number $4.5 < M < 5.2$. For $t > 22$ s during ascent, the primary test surface was entirely laminar. During phase three, AoA was estimated to be less than 0.5°, and the ratio of wall-temperature to stagnation-temperature was approximately 0.3. Flow downstream of the diamond-shaped trip on the secondary instrument ray remained turbulent until $t \sim 30$ s, after which it was laminar for the remainder of the ascent.

During phase three (smooth-body transition), transition occurred at conditions where Mack's second-mode was predicted to dominate. [57] Boundary layer stability analysis at intervals during $19 < t < 22$ s indicated second-mode N-factors at transition of $10.9 < N < 14.5$, with an average value of N=13.4. The frequency corresponding to the peak N-factor at transition during this period was calculated to be $400 < f < 725$ kHz. The transition N-factor calculated for t=19s (N=10.9) was low and slightly out-of-family with transition N-factors at later times. For $20 < t < 22$s, $13 < N < 14.5$.

The HIFiRE-1 ascent transition N-factors were broadly consistent with past hypersonic flight tests, that is to say, at the upper end of commonly-cited free-flight transition N-factors. Kimmel et al. [19] includes a brief comparison of HIFiRE-1 to previous tests. Stability calculations by multiple researchers for the Reentry-F and Sherman-Nakamura hypersonic flight tests indicated correlating transition N-factors of 3.7-15. [58, 59] The investigators ascribed much of this variation to uncertainty in the calculated boundary conditions. They noted that uncertainty in boundary conditions compounded as altitude decreased. With the lowest altitude Reentry-F transition case excluded, correlating transition N-factors for these two flights ranged from approximately 8-15.

The HIFiRE-1 transition measurements may be used, judiciously, to inform hypersonic transition design. The final transition prediction depends on the designer's risk tolerance. Based on the above data, it is reasonable to conclude that for a smooth, axisymmetric body, where ablation is not dominant, $8 < N < 15$ would be reasonable correlating N-factors for second-mode transition in hypersonic flight. This is an aggressive stance and probably approaches an upper limit on attainable laminar Reynolds number for these bodies under optimistic conditions. Depending on the desired level of conservatism, lower transition Reynolds numbers might be appropriate to account for uncertainty in flight conditions, surface geometry, or the potential for other bypass transition mechanisms.

A practical design question is the uncertainty in the transition location to which this *N*-factor uncertainty equates. This is situational, depending on the slope of *N*-factor versus *x*-location. Transition *x*-location is subject to more uncertainty at low Reynolds numbers than at high Reynolds numbers, due to the presumed spread in transition *N*-factor, since *N*-factor increases more quickly with *x* at high Reynolds numbers. Reference [57] tabulates this sensitivity about the measured transition location for HIFiRE-1 at various times. Transition *x* location sensitivity varies from $0.034 < \Delta x/\Delta N < 0.096$ (meters per unit *N*), for $19 < t < 22$ s. Taking into account nonlinearity in the *N*-factor versus *x* distribution, $8 < N < 15$ equates to an uncertainty of 35% of the cone length for HIFiRE-1 at $t = 22$ s.

Another concern regarding the assumed transition *N*-factor is the disturbance level, and variations thereof, in flight. Not enough hypersonic flight tests exist to develop a statistical sample of how flight disturbances affect transition. An *N*-factor of 14 (typical for HIFiRE-1 ascent transition) represents a million-fold amplification. This is not to say that the freestream disturbances were one-millionth of the boundary layer disturbances at transition. Freestream disturbances had to be processed, presumably, through some receptivity process and some subsequent linear and nonlinear amplification. It suffices to say that initial disturbance levels were probably quite low, perhaps immeasurable, and small scale. The second mode wavelength at $t = 22$ s was on the order of several millimeters. Indeed, the ultimate source of flight disturbances is unknown, and may remain unknown. Bushnell speculated on numerous sources of initial disturbances. [60] Fedorov et al. [61] have calculated that thermal molecular fluctuations (Brownian motion) might have engendered transition on HIFiRE-1.

Since disturbances amplify so rapidly, changes in the initial disturbance field do not necessarily translate into large differences in the transition location. Assuming that a disturbance breaks down after one-million fold amplification ($N = 13.8$), another disturbance beginning at half the initial amplitude of the first, would have to undergo a two-million fold amplification ($N = 14.5$), assuming that the disturbances undergo the same amplification process and break down at the same amplitude. For HIFiRE-1 at $t = 22$ s, the difference between $N = 13.8$ and $N = 14.5$ equates to only a 67 mm difference in transition location.

Besides prediction of the absolute transition location, it appears that stability theory is well-suited to analyze parametric trends on HIFiRE-1-type configurations. During its period of second-mode transition, the HIFiRE-1 flight experienced only small parametric variations. Ground tests, however, covered a wider range of Mach number, Reynolds number and nose bluntness. Transition from two wind tunnels were well-correlated across the parameter range by an average *N*-factor of 5.5, over a range $6 < M < 10$ and nose bluntness from sharp to 6.35 mm radius, although individual cases showed scatter around this value. [82] Later tests and analysis of similar configurations suggest that a variable *N*-factor for wind tunnel data that takes wind tunnel noise into account might be a better prediction method. [62] It should also be noted that a constant *N*-factor prediction method did not fare so well for correlating transition on HIFiRE-1 at AoA in ground tests. [82]

One goal of the HIFiRE experiments was to compare ground test transition to flight test transition. Figure 2 illustrates heat transfer data obtained in two wind tunnels and in flight. The flight time of $t = 22$ s was chosen since it was the lowest Reynolds number at which clean transition data was obtained, and thus closer to the wind tunnel Reynolds numbers. Data were normalized with edge conditions to minimize Mach number differences. The disparity between ground and flight test transition is evident. This disparity was also evident in calculated N-factors. For the cases shown in Figure 2, the NASA transition case was correlated with $N \approx 6$ [82], CUBRC with $N \approx 5.7$ [26], and the HIFiRE case with $N \approx 14.4$. [57]

Since the actual flight conditions varied from the preflight tests, it was not possible to make a one-to-one comparison among the wind tunnel tests and flight data. The wind tunnel tests were conducted at higher Mach numbers and with T_w/T_0 ratios different from the ascent transition conditions. Also, Reynolds numbers based on nose radius were different. By considering parametric trends, however, some conclusions may be derived. Figure 3 illustrates transition Reynolds numbers for the HIFiRE configuration as a function of the nose radius Reynolds number. Table 1 lists conditions for these tests. For comparison, and to illustrate the transition trend with nose radius, the smaller bluntness data from Stetson's 8° cone transition data [63] (replotted from [64]) are included on the graph. Transition Reynolds numbers were normalized with edge conditions to minimize effects from differing Mach numbers and cone angles. Edge values were based on Taylor-Maccoll solutions for sharp cones. Although nose bluntness certainly affected the edge conditions for some cases, the sharp cone edge conditions provided consistent and convenient reference values.

Despite the variations in conditions, the HIFiRE -1 flight data clearly trend higher than the wind tunnel data. The HIFiRE flight transition Reynolds number in Figure 3 is about 1.4 times higher than the Stetson Mach 6 data trend, and about twice the data trend for the HIFiRE-specific geometry.

Another potential confounding factor in comparing the wind tunnel to flight data is differences in wall cooling. However, Table 1 shows that the wind tunnel tests possessed wall temperature ratios either equivalent to or higher than the flight data. Assuming that transition was due to second-mode for all cases, decreasing T_w/T_0 for ground test, or increasing T_w/T_0 for the flight test, would only accentuate the differences between flight and wind tunnel transition Reynolds numbers, due to the destabilizing effect of wall-cooling on the second mode.

The effect of noise is clearer when *N*-factors are compared. The *N*-factor computations should take parametric differences between the flight and ground test into account. The correlating *N*-factors of 5.5 derived from wind tunnel tests [14] compared to the $N = 13\text{-}14$ correlating values observed in flight clearly demonstrate the dominance of wind tunnel noise in ground test.

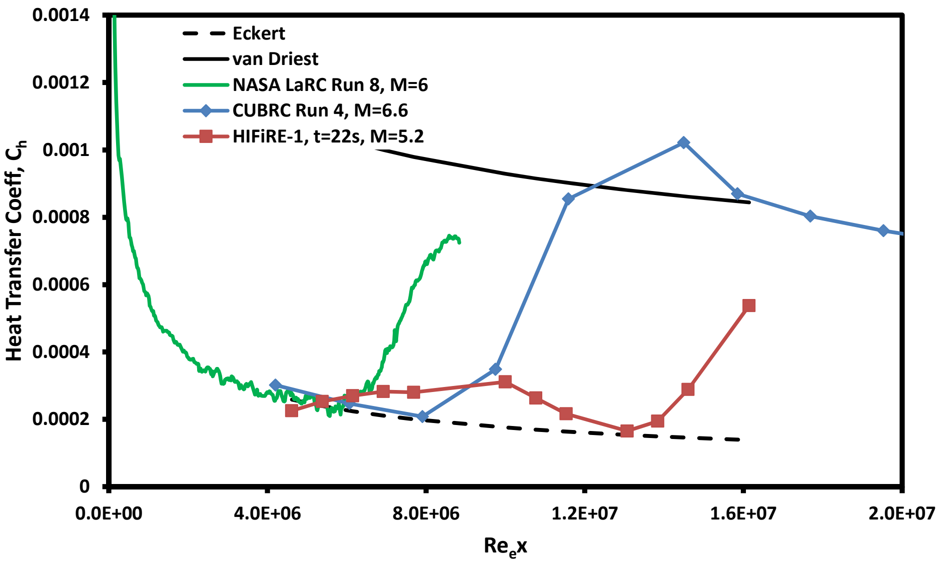

Figure 2 Heat transfer data from wind tunnel tests and flight.

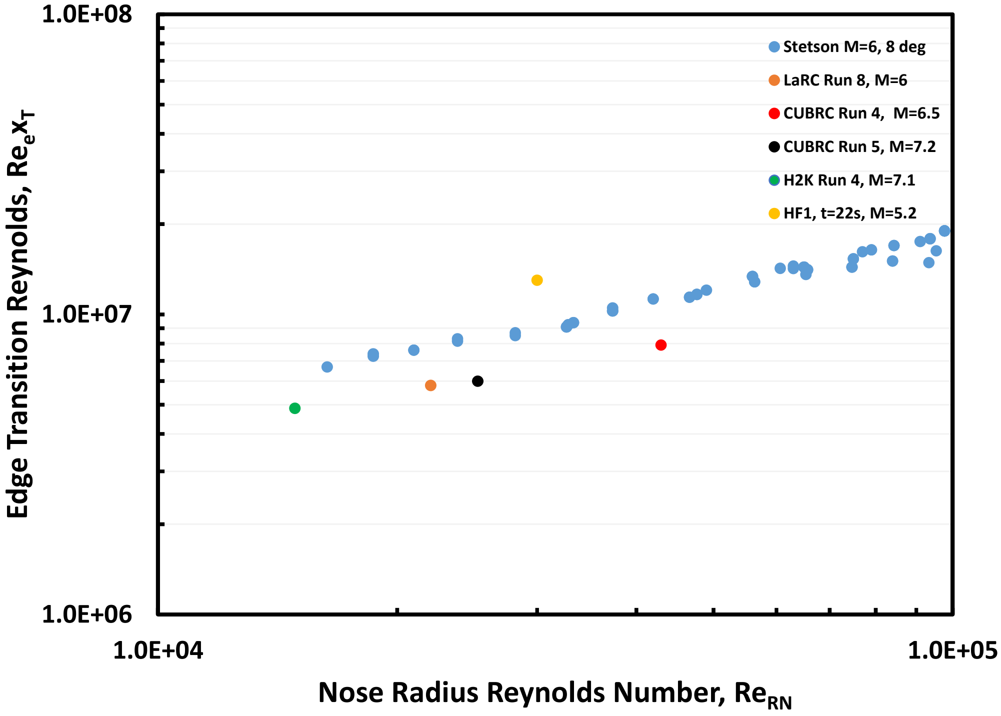

Figure 3 Transition Reynolds number based on edge conditions as function of nose radius Reynolds number.

Table 1 Ground Test Conditions.

	NASA Run 8	CUBRC Run 4	CUBRC Run 5	H2K Run 4	HIFiRE-1, t=22s	Stetson
M	6	6.6	7.2	7.1	5.2	6
Re/m	1.9E+07	1.7E+07	1.0E+07	9.3E+06	1.2E+07	3.07e+07 - 9.21E+07
Re_{RN}	22051	42968	25262	14880	30000	16333-97667
T_w/T_0	0.60	0.16	0.13	0.56	0.17	0.49

2.4. Transition in Three-Dimensional Flows – HIFiRE-1 Experimental Data

Both HIFiRE-1 and -5b flights provided information on hypersonic flight transition in fully three-dimensional flows. HIFiRE-5, because of its spanwise pressure gradient, possessed cross-flow even at zero AoA. HIFiRE-1 attained cross-flow data inadvertently during descent, due to its AoA. Although the HIFiRE-1 flight was not intended to acquire data at nonzero AoA, it was recognized that this might occur. To mitigate this risk, instrumentation was selected with sufficient frequency response to resolve fluctuations in the transition front due to vehicle attitude variations.

The HIFiRE-1 descent transition front was mapped out by determining the angular location and Reynolds number at which each transducer registered transition, as the spinning payload descended. The transition history recorded by each transducer may be visualized by assuming that the spatially nonuniform transition front was wind-fixed, and the transducer revolved beneath it. Early in the descent, at low Reynolds number, a transducer would indicate laminar flow continuously. As the Reynolds number increased, a transducer would register periods of laminar and turbulent flow during each revolution of the payload, due to the spatially nonuniform transition front. Finally, the transducer would be completely downstream of the transition front, and register continuously turbulent flow at all azimuthal locations. The highest bandwidth instrumentation, the Vatell heat transfer gauges and Kulite pressure transducers, registered the transition front with the highest temporal fidelity. The Medtherm coaxial thermocouples showed some evidence of the transition front nonuniformity, but this was greatly smeared due to their lower frequency response.

Transition data obtained in this fashion are presented as a function of transducer azimuthal location, relative to the windward attachment line, and Reynolds number based on freestream conditions and x-location. Formally, this presentation resembles typical x-ϕ maps of transition, for example those generated by Stetson. [65] It must be noted that HIFiRE-1 underwent significant variations in AoA ($5° < \alpha < 13°$)and freestream Reynolds number ($2x10^6 < Re < 8x10^6$ per meter) over the region covered by this map. Nevertheless, this presentation of the data permits general features of the transition front to be compared to static wind tunnel data and CFD, and the conclusions derived from the data are not invalidated.

Figure 4 (from [20]) illustrates the HIFiRE-1 transition front during descent, and the transition front measured in the DLR H2K wind tunnel. [66-68] Several notable features are apparent in this figure. First, data collected from three Kulite transducers (called out as PHBW in the figure), a Vatell heat transfer gauge (HT3) and Medtherm coaxial gauges (dot-dash line, Re_{TR}) are all consistent. Although the Medtherm gauges did not possess sufficient frequency response to resolve the transition front spatial nonuniformity, the transition location measured with the Medtherms falls at a Reynolds number that is the average transition Reynolds number observed with the higher bandwidth instruments.

Second, transition occurred at lower Reynolds numbers on the leeward centerline (Φ=180°), and higher Reynolds numbers on the attachment line (Φ=0°). This was expected and consistent with past wind tunnel results. [65, 69- 71]. A somewhat unexpected feature was that the highest transition Reynolds number occurred not on the windward or leeward symmetry meridians at Φ=0° and Φ=180°, but between them at about Φ=40° and Φ=300°. This multilobed transition front is probably the result of multiple instabilities, with traveling instabilities dominating transition on the windward and leeward meridians, and crossflow dominating between these meridians.

Third, the shape of the transition front measured in the H2K wind tunnel is somewhat similar to the shape of the flight transition front, with a low transition Reynolds number on the leeward meridian, and higher transition Reynolds number on the windward meridian. The H2K transition front does not appear to be sharply indented like the flight transition front, although the meager spatial resolution of the H2K measurements made this difficult to resolve.

Fourth, the leeward wind tunnel transition Reynolds numbers were lower than those measured in flight, as anticipated. Unexpectedly, however, wind tunnel transition on the windward meridian occurred at higher transition Reynolds numbers than in flight. Both this observation and the indented shape of the flight transition front are believed to be related to the higher wall-cooling of the flight article, as described below.

Various wind tunnel tests of smooth blunt cones, including the HIFiRE configuration itself, have shown contradictory trends of windward transition front movement with AoA. For HIFiRE-1 in H2K, the α=6° and α=12° windward transition Reynolds numbers ($Re_x=5.3\text{x}10^6$ and $Re_x=6.4\ \text{x}10^6$, respectively) were higher than the α=0° transition Reynolds number ($Re_x=3.9\ \text{x}10^6$), in contrast to the flight test trends. Similarly, tests of HIFiRE-1 in the NASA Langley Research Center (NASA LaRC) 20-Inch Mach 6 wind tunnel at α =0°, 3°, and 5° showed transition moving downstream on the windward meridian as AoA increased, although the change was modest. [17] Tests of HIFiRE-1 at Calspan University of Buffalo Research Center (CUBRC), however, displayed trends contrary to the H2K and LaRC tests. At α =0°, 1°, 2°, and 5°, and M= 6.6 and 7.2 in CUBRC, the windward transition front moved upstream with increasing AoA. [26] Some other wind tunnel tests have displayed upstream movement of the windward transition front with AoA on cones with small nose bluntness. [69-71] In all of the ground test cases, leeward transition also moved upstream with increasing AoA, and thus remained upstream of windward transition, as it did in the HIFiRE flight results.

The nature of the disturbances, and their interaction with wind tunnel noise and wall temperature, offers a possible explanation for these observations. High-bandwidth pressure transducers in the H2K experiment showed a strong instability on the windward centerline consistent with a second-mode transition. Computations also predicted second-mode windward transition in flight. [57] Second-mode instability is affected by wind tunnel noise, creating a trend toward lower transition Reynolds numbers in ground test, all else being equal. [72] However, second-mode is destabilized by wall-cooling, and the flight vehicle wall was more highly cooled than in ground test. The ratio of wall-to-total-temperature, T_w/T_0, was 0.56 in the H2K test, compared to 0.18 in flight. It is possible that increased wall-cooling in the flight test more than compensated for lower noise in the flight environment, leading to lower windward transition Reynolds number in flight compared to ground test. Wall temperature ratio for the CUBRC tests, which showed upstream windward transition movement like the flight, was $T_w/T_0 = 0.13$, relatively close to the flight value of 0.18. Also, the indented transition front observed on HIFiRE-1 in flight has been observed in ground test on highly cooled models. [70, 71, 73, 74]

It should also be noted that for swept cylinders tested at Mach 3.5, wind tunnel noise did not appear to affect leading edge transition. [75] In analogy to the swept cylinder attachment line, the cone attachment line may exhibit a similar lack of sensitivity to wind tunnel noise.

The apparent lesser effect of wind tunnel noise on transition around the shoulders of the model (Φ=90° and 270° on HIFiRE-1) might also be explained by the presence of crossflow instabilities. The putative second-mode spectral peak observed on the windward centerline in the H2K test was less prominent, or in some cases absent, away from the windward meridian. Infrared images in H2K also showed streaks consistent with a crossflow-induced transition. This evidence strongly suggests that transition on the shoulder of the model was crossflow-dominated. Since stationary crossflow instabilities are presumed to be less sensitive to wind tunnel noise, this might account for the lesser impact of wind tunnel noise on the shoulder transition in the H2K test, compared to zero AoA tests.

Wall-cooling is expected to stabilize stationary crossflow to a limited extent, but this effect is probably minimal. Gosse, for example, showed that wall-cooling reduced the crossflow Reynolds number on a sharp 2:1 elliptic cone at Mach 8. [76] Lakebrink [77] calculated that a reduction of approximately 5% in T_w/T_0 for HIFiRE-5 in a wind tunnel test would result in a reduction of peak stationary cross flow N-factor by 0.06. The relatively high shoulder transition Reynolds numbers on the flight article, compared to wind tunnel tests, might thus be due in part to increased wall-cooling, as well as lower noise.

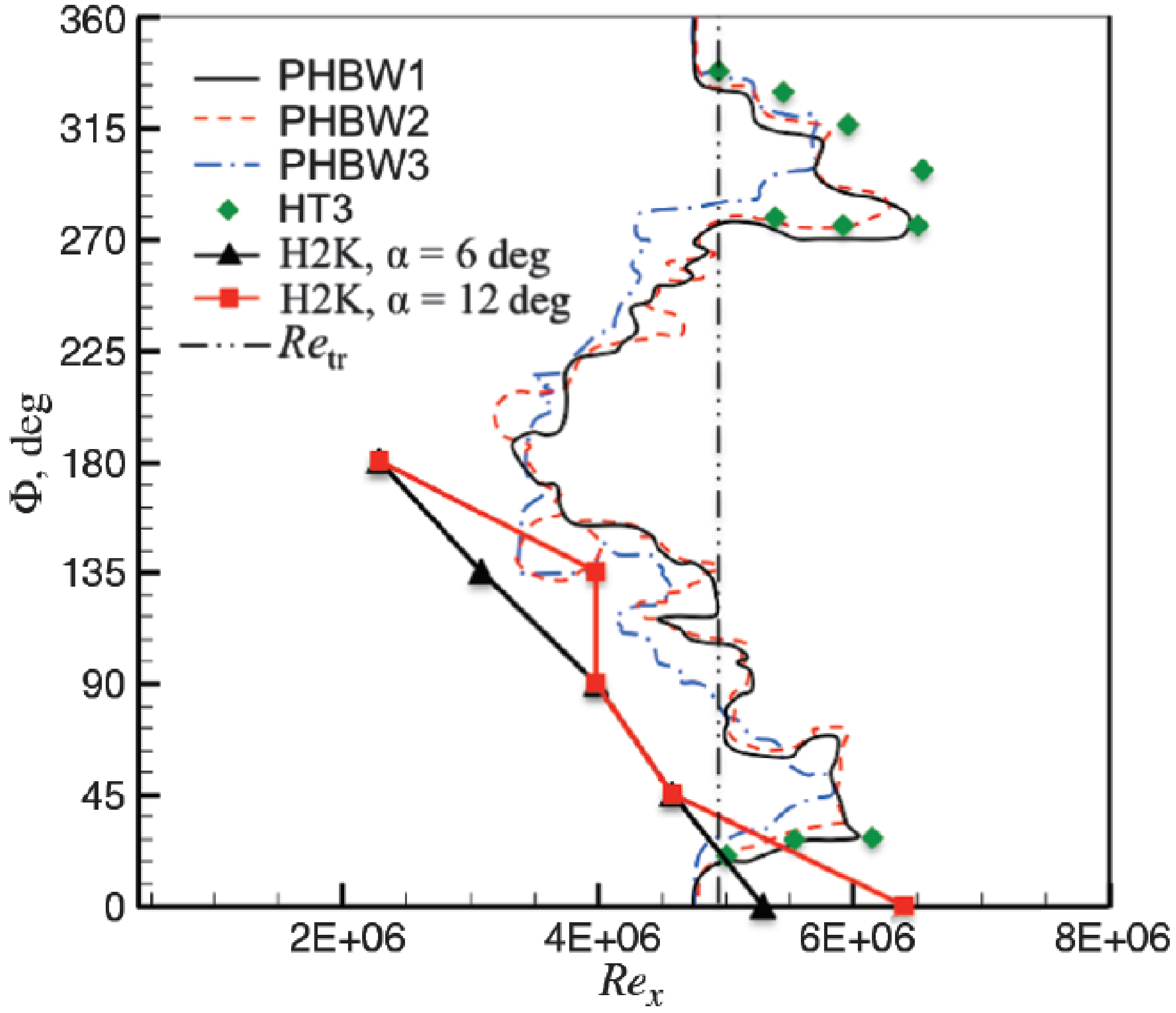

Figure 4 HIFiRE-1 descent transition map [20]. Φ=0°, 360°, windward, Φ=180°, leeward.

2.5. Transition in Three-Dimensional Flows – HIFiRE-5 Experimental Data

The results of this section were presented in modified form in prior publications, [21, 78] and are recapitulated here for completeness.

HIFiRE-5 data analysis faced a challenge similar to HIFiRE-1, namely, merging transition records from multiple transducers at various times during descent. Similar to HIFiRE-1, transition events derived from all transducers were synthesized into maps of the transition location in ϕ - Reynolds space. Also, like HIFiRE-1, this meant that when each transition event registered, the vehicle was at a different attitude. AoA was less than 1°, and the vehicle attitude did not have a major impact on transition Reynolds number on the centerline and leading edge meridians. However, at the maximum crossflow location, near the shoulder of the model (ϕ=45° on HIFiRE-5), transition was quite sensitive to yaw. Transition at the shoulder of the test article was promoted when that side was yawed into the wind. Therefore, some transducers registered multiple transition and laminarization events before recording continuously turbulent flow. The detailed effect of vehicle yaw is reserved for future analysis. The transition data presented in this section are based on first departure of a transducer from laminar heating. Therefore, they represent a transition Reynolds number for the most unstable attitude for that transducer.

Figure 5 (from [24]) shows flight transition Reynolds number as a function of spanwise location, at three different *x*-stations. This figure clearly shows three transitional lobes emanating from (top-to-bottom in the figure) leading edge, shoulder ($\phi = 45°$) and centerline. Undoubtedly, multiple instabilities led to this multi-lobed transition. The transition pattern is similar at each *x*-station. For each lobe, the transition Reynolds number varied less than 10% with streamwise location. In the two regions of delayed transition (centered near ϕ=25° and 70°), the transition Reynolds number and the azimuthal location of maximum transition Reynolds number varied more. As discussed above, the transition Reynolds numbers in Figure 5 near the ϕ=45° region are more representative of the condition where that side is yawed into the wind.

Currently, there is no wind tunnel test directly replicating flight conditions. Several wind tunnel tests of HIFiRE-5 exist at Mach 6 and 7, and for a sharp 2:1 elliptic cone at $M = 8$. HIFiRE-5 was tested at Purdue University, under quiet and noisy flow conditions [32-34, 36-38, 42], and at NASA LaRC [27, 39, 41], under noisy flow. The Purdue and LaRC tests used identically-scaled models. The sharp 2:1 elliptic cone was tested at M=8 under noisy conditions in Tunnel B of the Arnold Engineering Complex von Karman Facility (AEDC VKF-B). [49-51] Limited qualitative infrared imaging data were obtained at M =7 at CUBRC. [53]

The most comprehensive wind tunnel data were obtained in the Purdue Mach 6 quiet tunnel. Data included oil flows, temperature-sensitive paint, infrared imaging, and Kulite and PCB surface pressure measurements. Tests displayed stationary crossflow instabilities under quiet flow with oil flow, temperature-sensitive paint and IR. Figure 6 (from [37]) illustrates the heat transfer signature of stationary crossflow vortices and transition at M=6 and Re=12.3×10^6 /m under quiet flow. Stationary crossflow instabilities were only weakly evident under noisy flow. Traveling crossflow instabilities were measured in quiet flow, but could not be observed under noisy conditions. Kulite pressure transducer arrays permitted extraction of wave angle and phase velocity from traveling crossflow instabilities in quiet flow. Centerline and acreage transition was observed under both quiet and noisy conditions. The Purdue tunnel could not achieve a high-enough Reynolds number to produce leading edge transition under either noisy or quiet flow. Transition under quiet flow consisted of multiple lobes, with transition appearing most upstream on the centerline and the shoulder of the model. The lobe structure of the transition front was less well-defined under noisy flow, as discussed below.

Tests of HIFiRE-5 at LaRC under noisy flow focused on thermographic phosphor imagery. Noisy transition data were obtained for all locations on the model, from centerline to leading-edge, including data with sideslip and angle of attack. Testing at the Texas A&M University Actively-Controlled-Expansion wind tunnel explored wind tunnel noise effects. [35] Later testing in this tunnel showed transition patterns similar to those obtained in the Purdue tunnel, and evidence for stationary crossflow vortices. [79]

Figure 7 (from [78]) compares flight and wind tunnel transition. Except for tests at CUBRC, no ground tests replicated flight T_w/T_0, which is suspected to be significant, especially for attachment line transition. Wall-cooling destabilizes second-mode instabilities, but reduces crossflow Reynolds number. [76] Despite the dissimilarities among these tests and flight conditions, some general conclusions may be drawn regarding HIFiRE-5 transition in the wind tunnel versus flight.

First, centerline transition occurred at relatively low Reynolds number in flight, as in ground test. The strongly inflected centerline velocity profile dominated transition here, making the boundary layer susceptible to rapidly-amplifying traveling instabilities. The scenario is probably similar to leeside transition on HIFiRE-1 at AoA. HIFIRE-5 flight centerline transition occurred at $Re_x \sim 4.5\text{x}10^6$ at Mach 7.8. HIFiRE-1 leeward transition occurred at $Re_x \sim 3.2\text{x}10^6$ at Mach 7.0. This is contrasted with HIFiRE-1 zero AoA transition at M=5.3, which took place at $Re_x \sim 10^7$.

Second, for the wind tunnel cases, centerline transition under noisy flow occurred at much lower Reynolds numbers (about $1\text{x}10^6$) than in flight (approximately $4.5\text{x}10^6$). In quiet flow, centerline transition occurred at a Reynolds number of about $3.2\text{x}10^6$, much closer to the flight value. This transition Reynolds number decrement due to tunnel noise, a factor of approximately 3, is comparable to that seen for HIFiRE-1 at α=0° and $M \sim 5.2$. Multiple centerline transition points for the LaRC data represent different unit Reynolds number cases, with higher transition Reynolds number corresponding to higher unit Reynolds number. This effect is often attributed to the spectral distribution of wind tunnel noise. [62, 80]

Third, the distinct lobe near ϕ=45° present in flight and quiet wind tunnel flow was still evident in noisy flow. Linear stability calculations and wind tunnel tests indicated that transition near ϕ=45° was crossflow-dominated. TSP and IR imaging show that crossflow transition in the Purdue tunnel slightly preceded near-centerline transition in quiet flow, but under noisy flow, this was reversed, and near-centerline transition preceded crossflow transition. This earlier transition and lateral spreading of the near-centerline transition apparently made the transition-front indentation near ϕ=25° in quiet flow somewhat less prominent in noisy flow. The LaRC noisy tests also showed a transitional lobe near ϕ=45°. Figure 8 presents a thermographic phosphor image demonstrating this structure. Although a lobed structure was present in these images, the inboard portion of the transitional lobe was difficult to resolve from numerical heat transfer data, so Figure 7 shows only the outboard portion of the lobe for the LaRC data. The plot of the LaRC data incorporates both left and right sides of the model, creating some scatter due to left/right asymmetry. Although there is little overlap in the LaRC and the Purdue noisy data, the two data sets appear consistent. For comparison, Figure 9 shows heating contours obtained under noisy flow in the Purdue wind tunnel at conditions similar to those of the LaRC data in Figure 8. Since the Purdue and LaRC models were the same size, the similarity in the transition fronts is readily apparent.

The observation that wind tunnel noise affected near-centerline transition, which was dominated by traveling instabilities, slightly more than the crossflow transition, is consistent with the supposition that wind tunnel noise would affect traveling instabilities more strongly than stationary instabilities. That wind tunnel noise had this impact on crossflow transition is somewhat surprising, given the presence of stationary crossflow in this region. Traveling disturbances must develop somehow during the crossflow transition process however, as energy at zero frequency is distributed to nonzero frequencies, and wind tunnel noise may impact this process. Also, traveling crossflow waves were observed prior to transition in quiet flow, although the relative roles of traveling and stationary crossflow instability remains unclear. [36]

A fourth observation is that the flight case showed a distinct leading-edge transition lobe. Leading edge transition occurred in the LaRC tests, but it appeared to have a different character. Transition occurred on the leading edge, but it was the most downstream transition location on the model. Similar leading edge transition behavior occurred on the sharp elliptic cone at M=8. [51] In noisy flow, leading edge transition perhaps arose from spanwise contamination from adjacent turbulent regions. [39] Even so, wind tunnel noise did not seem to affect outboard ($\phi >$ 50°) and leading edge transition as radically as centerline transition. In the LaRC tests, leading edge transition occurred at $Re_x \sim 3.7 \times 10^6$, compared to about 4.5×10^6 in free flight. This result is somewhat reminiscent of the behavior of the HIFiRE-1 windward side transition when that test article was at angle of attack. In this case, windward transition Reynolds numbers in noisy flow were comparable to or even exceeded flight transition Reynolds numbers. At least part of this difference was ascribed to the higher wall cooling on the flight vehicle. [20]

The exception to these ground-test results for leading edge transition was the temperature-sensitive paint images obtained at CUBRC at about M=7. [53] In this study, at least one image showed a leading edge transition lobe where transition occurred at Reynolds numbers nearly identical to or lower than centerline transition.

On the other hand, wind tunnel noise would have acted to reduce ground-test transition Reynolds numbers in two ways. First, wind tunnel noise would be expected to promote transition in ground test, although higher second-mode frequencies on the attachment line (compared to the centerline) may have lessened the impact of noise, since freestream tunnel noise spectrum rolls off at higher frequencies. More significantly, in noisy flow, leading edge transition perhaps arose from spanwise contamination from adjacent turbulent regions, negating effects of wall-cooling. [39]

That the multi-lobed transition front was observed both in flight and in the quiet wind tunnel, and that the same trends in crossflow transition were observed in wind tunnel and flight, is a powerful indication that the quiet tunnel accurately represented the flight transition mechanism. This further reinforces the notion that the flight transition was the result of modal instabilities, as observed in the wind tunnel.

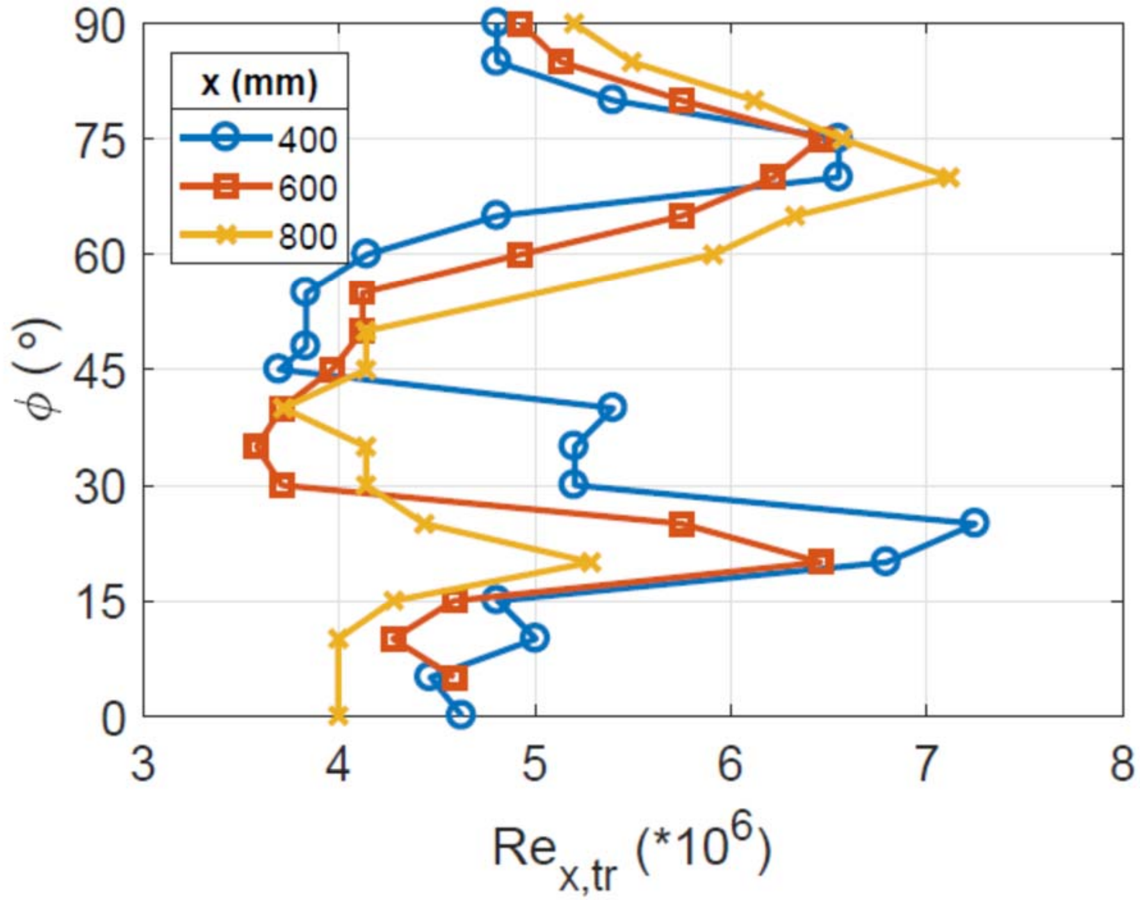

Figure 5 Transition Reynolds numbers at three streamwise locations (reproduced from [24]).

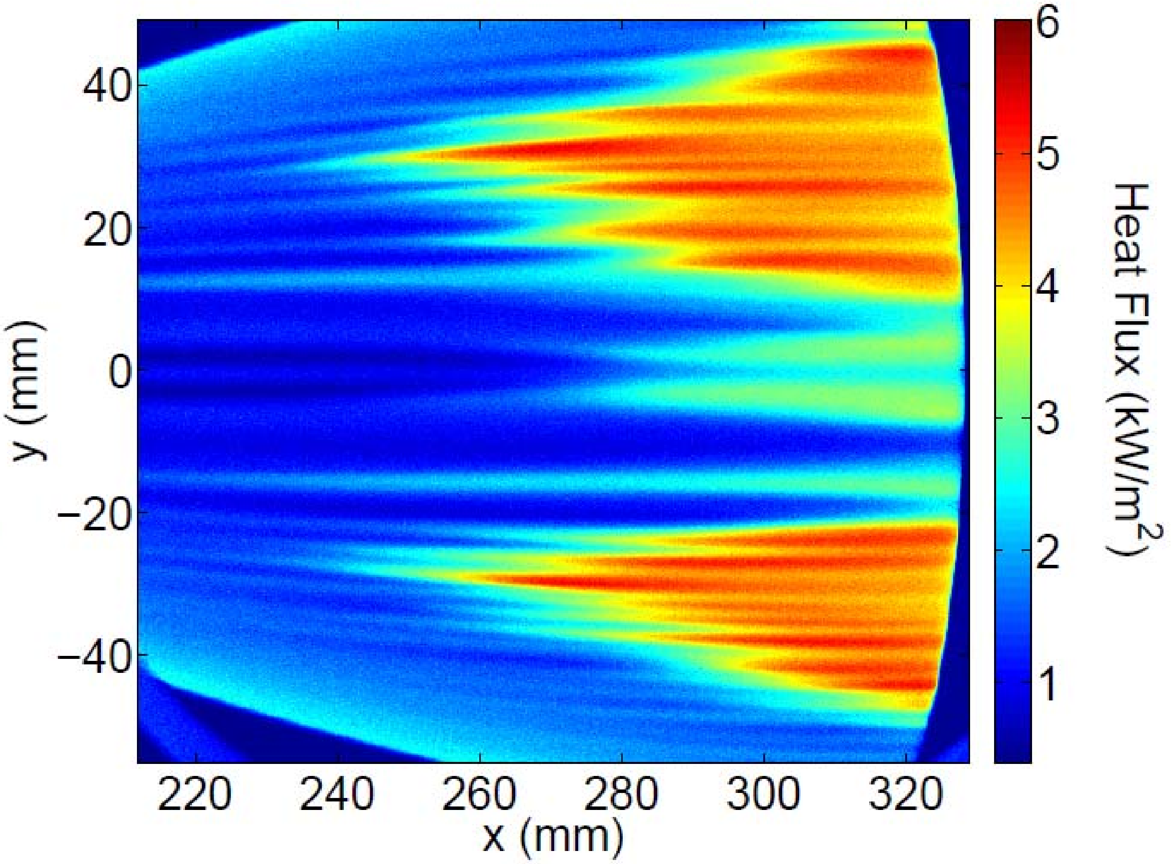

Figure 6 Heat transfer for HIFiRE-5 derived from infrared imaging, *M*=6, Re=12.3×10^6/m, quiet flow, Purdue wind tunnel (reproduced from [37]).

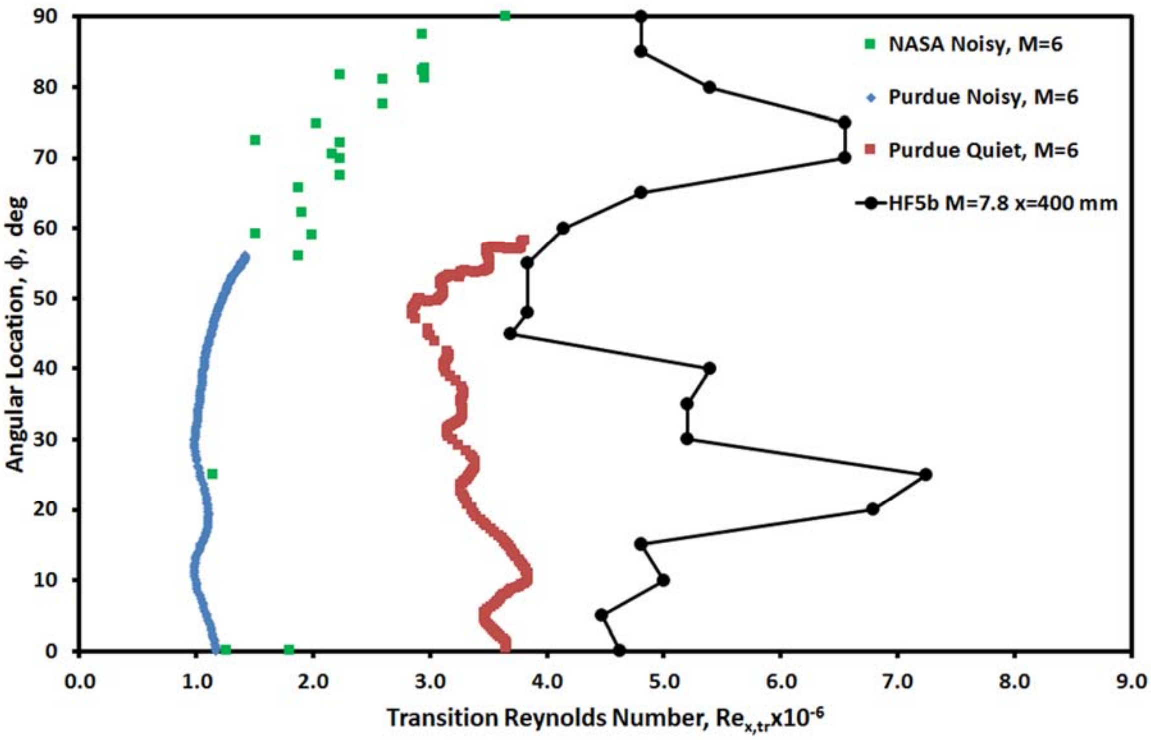

Figure 7 Noisy and quiet wind tunnel transition compared to flight transition (reproduced from [78]).

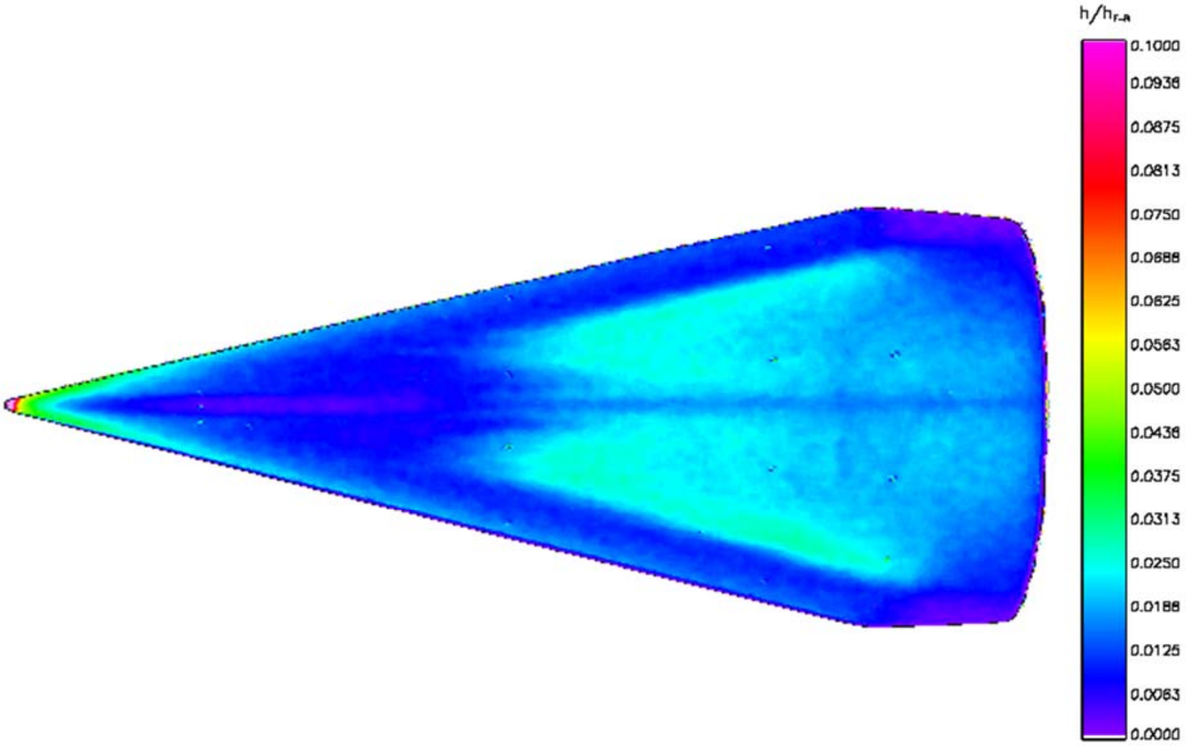

Figure 8 Heat transfer contours derived from thermographic phosphor image from LaRC Run 8. M=6, Re=9.5×10^6 /m, α=0°. Enlarged image extracted from [39].

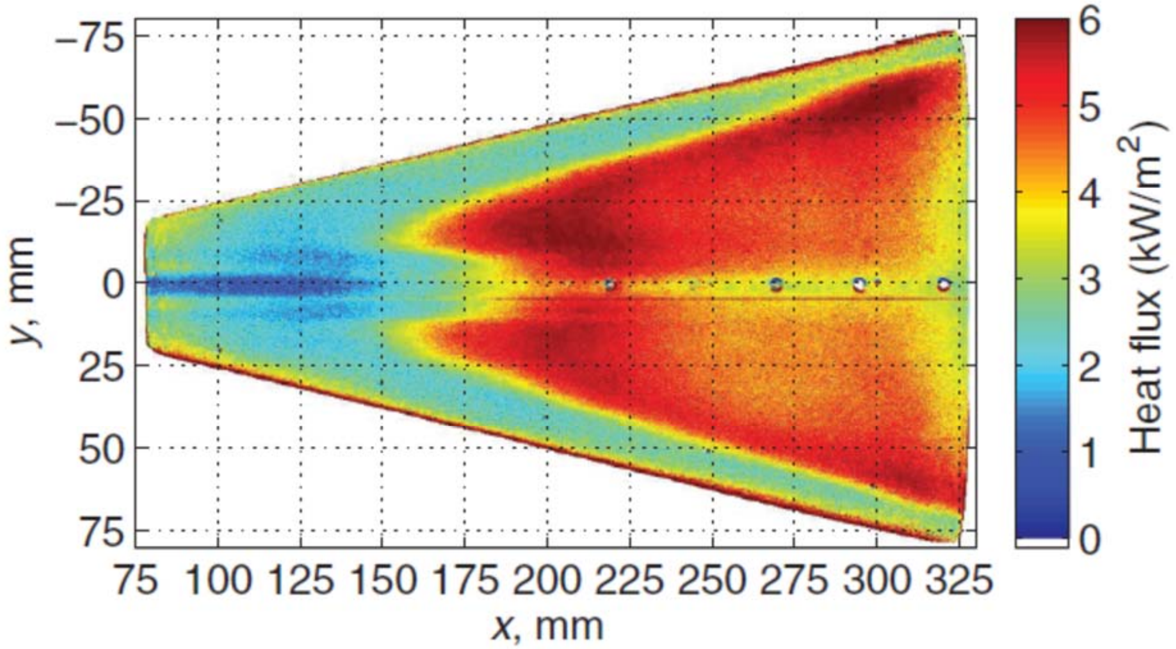

Figure 9 Heat transfer contours derived from temperature-sensitive paint image from Purdue wind tunnel *M*=6, Re=10.2×10^6 /m, α=0°, noisy flow (reproduced from [42]).

2.6. Transition in Three-Dimensional Flows – HIFiRE-1 and -5 Computations

Boundary layer stability calculations for HIFiRE-1 at angle of attack were generally successful in replicating flight transition phenomenology. Li et al. [81] executed post-flight stability calculations for several points in the descent trajectory, labeled R1-R4, with increasing time (Table 2). Each point represented a significant event. R1 (t = 481.3s) corresponded to a condition with fully laminar flow, but with periodic pressure fluctuations near the shoulder of the test article. These pressure fluctuations peaked at condition R2 (t = 483.7 s). Conditions R3 and R4 were for the same time (t = 485 s), but different angles of attack (α = 7.5° and 6.1° respectively). At conditions R3 and R4, flow had just become fully turbulent at all azimuthal locations at the x=850 mm, where most of the high bandwidth instrumentation was clustered.

Parabolized Stability Equation (PSE) second-mode calculations for R1 predicted a maximum *N*-factor on the windward centerline of 6.4, consistent with the laminar flow observed in flight at this time. For point R2, the *N*-factor at x=850 mm was 14, consistent with the first appearance of transition in flight on the windward centerline at t = 483.8 s. For condition R4, the *N*-factor at x = 850 mm exceeded 14, consistent the observation of turbulent flow in flight at this time. Interestingly, the *N*-factor at the aft-most portion of the test article was 23 on the windward meridian, but only 9.5 on the leeward meridian. Li et al. [81] attributed the relatively slow instability growth of traveling instabilities on the leeward meridian to the structure of the mean flow there.

No attempt was made to develop a correlating *N*-factor for crossflow transition in flight, but the computational observations were broadly consistent with flight observations. Stationary crossflow calculations indicated an *N*-factor of 9.5-10 at x = 850 mm for condition R1, which was shortly before flow at the shoulder of the test article became turbulent at this station. For condition R4, crossflow *N*-factors exceeding 14 were predicted for x = 850 mm, with *N*-factors attaining a value of 23 at the end of the cone. These results were consistent with observations of fully laminar flow in flight at condition R1, and fully turbulent at R4.

Tufts et al. [26] executed post-flight linear PSE computations for HIFiRE-5, examining leading edge and crossflow stability. *N*-factor contours presented a lobed appearance similar to the transition front data. Traveling instabilities dominated the leading edge, and crossflow instability dominated the acreage. By comparing the computed *N*-factors to flight transition data, Tufts estimated the *N*-factors at transition on the acreage and leading edge to be 10 and 18, respectively. The acreage flight transition data were affected by model yaw angle, however, so the *N*=10 value is probably more indicative of conditions where that side of the model was yawed into the wind.

Tufts et al. [26] also executed PSE computations for some post-flight wind tunnel cases. Again, computed *N*-factor contours resembled the transitional lobes displayed in the wind tunnel tests. The *N*-factor of 10 that correlated the flight crossflow transition also appeared to correlate wind tunnel crossflow transition. Movement of the *N*=10 contour with AoA also resembled the transition front movement observed in the wind tunnel with AoA. Moyes, et al. [82] also using linear PSE, determined crossflow *N*-factors at transition of 5-8 for flight.

Choudhari et al. [27] performed preflight stability calculations for HIFiRE-5 at anticipated flight conditions. These calculations included computations of centerline instabilities, as well as attachment line and crossflow. Notably, these computations indicated a strongly unstable leading edge, with *N*-factors similar to the unstable centerline boundary layer. Given that the leading edge transition in flight occurred at nearly the same Reynolds number as the centerline transition, it seems plausible that the computed stability behavior on these meridians accurately represented flight.

Despite the high amplification predicted for the leading edge in flight, uncontaminated leading edge transition was observed only in CUBRC, where the ratio of wall to stagnation temperature was closer to the flight test. In analogy to the attachment line flow on the cone at angle of attack, it is suspected that cooling is highly destabilizing to the HIFiRE-5 leading edge.

Table 2 HIFiRE-1 Descent Analysis Cases (transcribed from [81]).

Case	Time (s)	α (deg)
R1	481.3	13.6
R2	483.7	9.6
R3	485.0	7.5
R4	485.0	6.7

2.7. Conclusions

Perhaps the most significant conclusion from the HIFiRE-1 and -5 research campaigns was the success of boundary layer stability theory in reproducing transition trends and patterns, implying that the stability calculations and wind tunnel tests reproduced at least some of the transition physics observed in flight. Although boundary layer instabilities were not directly measured in flight, the correlation between flight transition trends and those observed in ground test and computation is persuasive evidence that modal instabilities were responsible for transition in flight. This is not a trivial conclusion. Given the small scale and high frequency expected for these instabilities, it was not clear that the flight environment would provide sufficient excitation to generate them. Although *N*-factor correlations and ground test were able to replicate some trends from prior hypersonic flight tests, these predictions may have merely been simulants for some other, undetermined, instability process that occurred in flight. We can now proceed with greater confidence to apply these tools to flight. Although these tools suffer recognized limits, they appear applicable to a wide range of flow scenarios.

The goal of using the HIFiRE flights to calibrate *N*-factor predictions and ground test was achieved, within the limits of the *N*-factor transition prediction approach. It is probably unrealistic to expect a single *N*-factor to correlate transition across a broad range of scenarios. Linear growth represents only a portion of the stability process. Variations in initial amplitudes, receptivity and nonlinear amplification probably all affect the best correlating *N*-factor. However, given the relatively high transition *N*-factors attained by the HIFiRE flights, the HIFiRE flight transition *N*-factors probably represent near-upper limits on attainable *N*-factors for smooth bodies. Since flight conditions, including disturbance levels and vehicle roughness, may vary from flight-to-flight, a statistical approach to transition prediction is probably warranted.

The subsidiary goal of calibrating ground test transition Reynolds numbers to flight was partially successful. In analogy to calibrating *N*-factor predictions, this goal was probably somewhat unrealistic, given the myriad parametric effects possible in ground test. This might be rectified in some cases by repeating ground tests with conditions tailored to flight. Despite this, some general conclusions could be reached. Axisymmetric, leeward and crossflow transition all showed lower transition Reynolds numbers or *N*-factors in the wind tunnel compared to flight. The impact of noise on HIFiRE-5 leading edge transition was not as great as for the other transition scenarios. Windward attachment line transition was an even more dramatic exception. HIFiRE-1 windward transition actually occurred at a lower Reynolds number in flight compared to the wind tunnel. The implication from this observation is that either attachment line transition is not as severely impacted by wind tunnel noise as the other transition mechanisms, or it is exceptionally sensitive to wall temperature differences. For attachment lines, the wind tunnel transition may not represent a worst case scenario, and designers should exercise due caution.

3. Collaboration between Flight Test, Ground Test, and Computation on HIFiRE-5

3.1. Introduction

The success of the HIFiRE-5 flight program was made possible in large part by the integration of ground test data and computational data in both the preflight experimental design, and in the post-flight data analyses. This paper describes how the synthesis of these three research tools permitted a well-designed experiment and created an understanding of hypersonic transition that was inaccessible to any one or two tools in isolation.

Research into boundary-layer transition, and particularly hypersonic boundary-layer transition, is in some sense dominated by a dynamic wherein any individual test, computation, or experiment provides only flawed or limited data. No one method available today is able to provide a picture of the full transition process due to limitations inherent to each.

In many external aerodynamics applications, the process of the boundary-layer naturally transitioning to turbulence (not tripped due to surface features) consists of several stages. In the first stage, environmental disturbances combine with geometric and flow features of the given geometry to introduce disturbances into the boundary layer. These disturbances are selectively amplified by the flow until reaching some critical amplitude, which in turn triggers parametric instabilities and nonlinear interactions leading to breakdown and turbulence. This is summarized in the ubiquitous Pathways to Turbulence illustration, here Figure 10, first presented by Morkovin et al. [83] For hypersonic external flows undergoing natural transition to turbulence (not intentionally tripped), it has been argued that only paths A-C are relevant, [84] and for reasonably slender and smooth vehicles such as HIFiRE-5, the focus has been on path A. In order to fully understand transition to turbulence, it follows that each step in the path to turbulence must be properly understood also. It is instructive therefore to examine why any given test or computation is in general insufficient in terms of this path.

3.2. Ground Test

While ground testing in wind tunnels is in many respects representative of flight test conditions, as is the case in hypersonic boundary-layer transition, one is often unable to completely match conditions that would be experienced in flight.

Consider four parameters:

1. Freestream-disturbance characteristics
2. Reynolds number
3. Wall-temperature ratio
4. Mach number

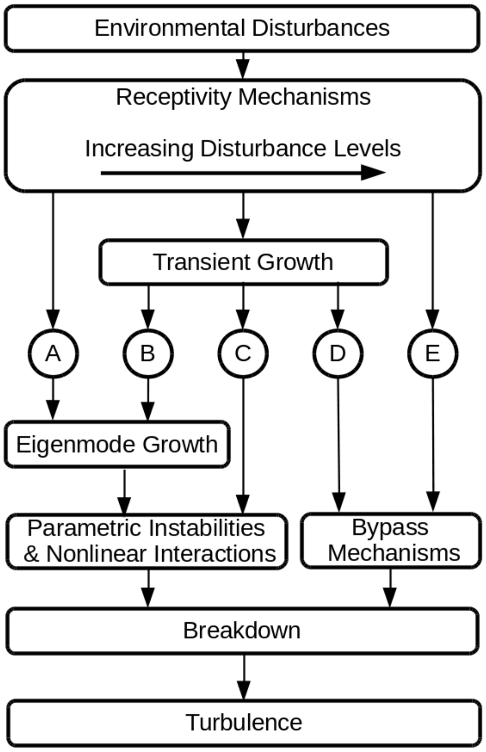

Figure 10 Pathways to Turbulence in Wall Layers

These four parameters cannot be simultaneously matched to hypersonic flight in any wind tunnel in existence today. Boundary-layer transition is, however, sensitive to all of the above parameters. The quantitative effect of each individual parameter is difficult to determine. For this reason, transitional behaviors observed in wind-tunnel tests often vary from the behavior seen in the flight scenarios meant to be studied.

Once a step in the path to turbulence has been misrepresented or modified, the subsequent steps must also be considered in the context of this change. It follows then, that the effect of not matching freestream-disturbance characteristics is perhaps the most problematic. Beyond an effect of amplitude of growth or location of transition, in some cases even the fundamental mechanisms governing transition to turbulence can be modified by differences in these parameters. In the context of paths to turbulence, this may change the primary eigenmodes responsible for transition (e.g. traveling vs stationary crossflow) or even change the path to transition (e.g. from A to C in Figure 10) In addition, the freestream disturbances present in hypersonic wind tunnels are in general not fully characterized, as to do so requires specification of more than a freestream turbulence amplitude. Full characterization implies specification of amplitudes, frequencies, length scales, and orientation of both acoustic and vortical disturbances. [85] Wind-tunnel results therefore may be ambiguous or misleading when taken on their own without the context of supporting calculation or flight test.

3.3. Computations

Computational studies by their nature allowed for very detailed, non-intrusive examination of the data returned by the simulation. However, currently the most advanced method of boundary layer transition in widespread use is some form of solution to the Linearized Navier-Stokes Equation set, coupled with a criterion on amplification of a given disturbance. The computational results in this paper focus on solutions to the Parabolized Stability Equations (PSE) coupled with a constant transitional *N*-factor. Although there have been some advances in DNS studies [86], as well as absolute-amplitude based methods [62], these methods are still immature in terms of production usage.

For the types of calculations presented in the current work, it is not possible to simulate the entire transition process outlined in **Figure 10**. Computations give detailed answers about eigenmode growth, and in the case of non-linear studies also about transient growth and parametric/nonlinear interactions. However, the receptivity and breakdown phases are only crudely accounted for through the choice of transition *N*-factor.

The necessity of calibrating and using this correlating factor introduces a large amount of uncertainty to computational predictions, particularly when the data set used to calibrate the choice of *N*-factor is limited, as is the case with hypersonic flight.

3.4. Flight Test

Many of the unique challenges posed by hypersonic flight testing arise because the majority of hypersonic flight vehicles are not reusable. The most obvious drawback of this fact is that a new vehicle must be built and instrumented for each flight. The number of tests able to be made for a given budget is therefore severely limited simply by material costs. In the case of both HIFiRE-5 flights it was known that the flight vehicle would likely not be recovered fully intact, thus recording flight data on the vehicle and recovering post-flight was not an option. This necessitated telemetered data collection, which limited the amount of data that can be collected due to bandwidth limitations. Also, HIFiRE possessed only discrete surface sensors. Transition imaging techniques like IR [87] were not feasible.

Another major consideration is that when performing flight test, measuring and quantifying even the basic parameters (e.g. Mach number, angle of incidence) is a non-trivial task. [88, 89] In the case of HIFiRE-5b for example the uncertainties estimated to be present in the Mach number and Reynolds number due to uncertainty in the altitude at a given time stamp are 2% and 3% respectively. [82] Also at the time of the HIFiRE-5 flights, it was not feasible to measure atmospheric fluctuations with bandwidth relevant to instability processes.

Flight testing in general, and hypersonic flight testing especially, therefore cannot provide the same amount and quality of data as ground test can. Given the limitations and cost of flight testing, flight tests must provide some crucial information that cannot be obtained from CFD or ground test. [90] The two preceding sections describe why, from computation and ground test alone it is not possible to fully understand and predict boundary-layer transition under flight conditions. In this case, flight testing is the only available method to obtain boundary-layer transition data under the conditions likely to be experienced by a full-scale flight vehicle.

Flight data is therefore limited in quantity and in scope. These data when taken in isolation, are therefore difficult to extrapolate accurately to general cases.

3.5. The Full Picture

In summary, ground testing is relatively affordable and can provide detailed and extensive data on transition processes, but is unable to replicate the full conditions experienced in flight. Computations provide fully replicated boundary conditions, but are unable to provide much, if any, data on the receptivity and breakdown processes. Flight tests fully duplicate the conditions of real-world vehicles, but are too expensive to perform regularly and return relatively limited data.

This dynamic, pictured in Figure 11, drives the need to have all three methods of study working together to provide the full picture of the hypersonic boundary-layer transition process.

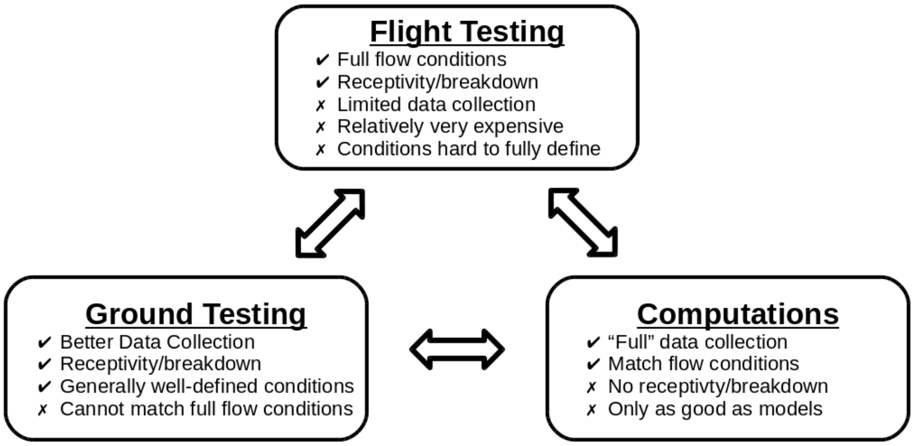

Figure 11 Research Triad

3.6. The HIFiRE Flight Series

The Hypersonic International Flight Research Experiment (HIFiRE) series of flights is a hypersonic flight research program administered by the United States Air Force Research Laboratory (AFRL) and the Australian Defence Science and Technology Group (DTSG). The purpose of the HIFiRE flight series in general is to provide demonstrations and validation data for technologies to be used in future hypersonic vehicles. The HIFiRE-5 was the fifth in the series and along with HIFiRE-1 is one of two with a focus on hypersonic boundary-layer transition.

The HIFiRE-5a mission launched 23 April 2012 from Andoya, Norway. [44-47] The second stage of HIFiRE-5a failed to ignite, preventing the payload from attaining hypersonic speeds. Despite the failure of the HIFiRE-5a second stage, the payload acquired supersonic transition data. However, since this did not satisfy mission objectives to acquire hypersonic transition measurements, a new payload, essentially identical to the first, was constructed and flown at Woomera, Australia, on 18 May 2016. This mission, HIFiRE-5b was entirely successful. [21-26, 82, 89]

3.7. Preflight Experimental Design

3.7.1. Flight Test Window Definition

HIFiRE-5 flew a high, lofted ballistic trajectory. [21] Therefore, freestream conditions varied rapidly throughout de- scent. The flight vehicle was required to be near zero angle of attack at the start of the descent test window, and to remain intact through most, if not all, of the window.

Preflight transition predictions determined the test window. The test window was defined as the time between the first transitional flow near the back of the test article, to the time when transition had moved upstream of the most forward transducer. Thermal and aerodynamic stress on the vehicle increased rapidly during descent. Overestimating the transition Reynolds number would complicate vehicle design, since it would be required to remain intact to an unnecessarily low altitude. Underestimation of the transition Reynolds number might lead to a design that would not remain intact through the test window.

The beginning of the test window affected vehicle flight path alignment requirements. A zero, or near-zero, angle-of-attack was desired to ease interpretation of transition results. To minimize cost and complexity, the vehicle possessed no active control system other than cold-gas thrusters for the so-called bang-bang maneuver. [21] The objective of the exoatmospheric bang-bang maneuver was to align the vehicle longitudinal axis with the expected descent flight path to limit aerodynamic stress on the vehicle, and maximize test time. Without this, the vehicle would enter the atmosphere at an extreme angle of attack. Since the vehicle was statically stable, it would oscillate and eventually converge on zero angle of attack (unless aerodynamic forces arising from the high angle-of-attack destroyed it first), but would probably still be oscillating during the test window. The bang-bang maneuver failed on the HIFiRE-1 flight, causing the vehicle to undergo damped oscillations between 6° and 13° in AoA as the payload transitioned. This AoA greatly complicated interpretation of the HIFiRE-1 transition data.

The beginning of the test window determined alignment accuracy and acceptable coning of the vehicle at the end of the bang-bang maneuver. Any small residual coning or misalignment at the end of the bang-bang maneuver would be removed through aerodynamic forces prior to the test window start. If the predicted transition Reynolds number was too high, this would result in overly relaxed tolerances for the maneuver, and AoA might be too high. If the predicted transition Reynolds number was unrealistically low, it might not be possible for the bang-bang maneuver to align the vehicle sufficiently prior to transition.

Figure 12 compares preflight predictions of the test window, compared to flight measurements. In this figure B denotes beginning of test window; E denotes end; F denotes flight; WT denotes wind tunnel; GNxx denotes Gosse preflight prediction for h = 21.8km, N=xx. This figure draws on three data sources: flight data, wind tunnel data from the NASA LaRC Mach 6 wind tunnel, [39] and PSE N-factor predictions [28] The actual flight test window is defined as the time when the most aft thermocouple on the centerline at $x = 0.85$ m transitioned, to the time when the thermocouple on the leading edge at $x = 0.3$ m transitioned.

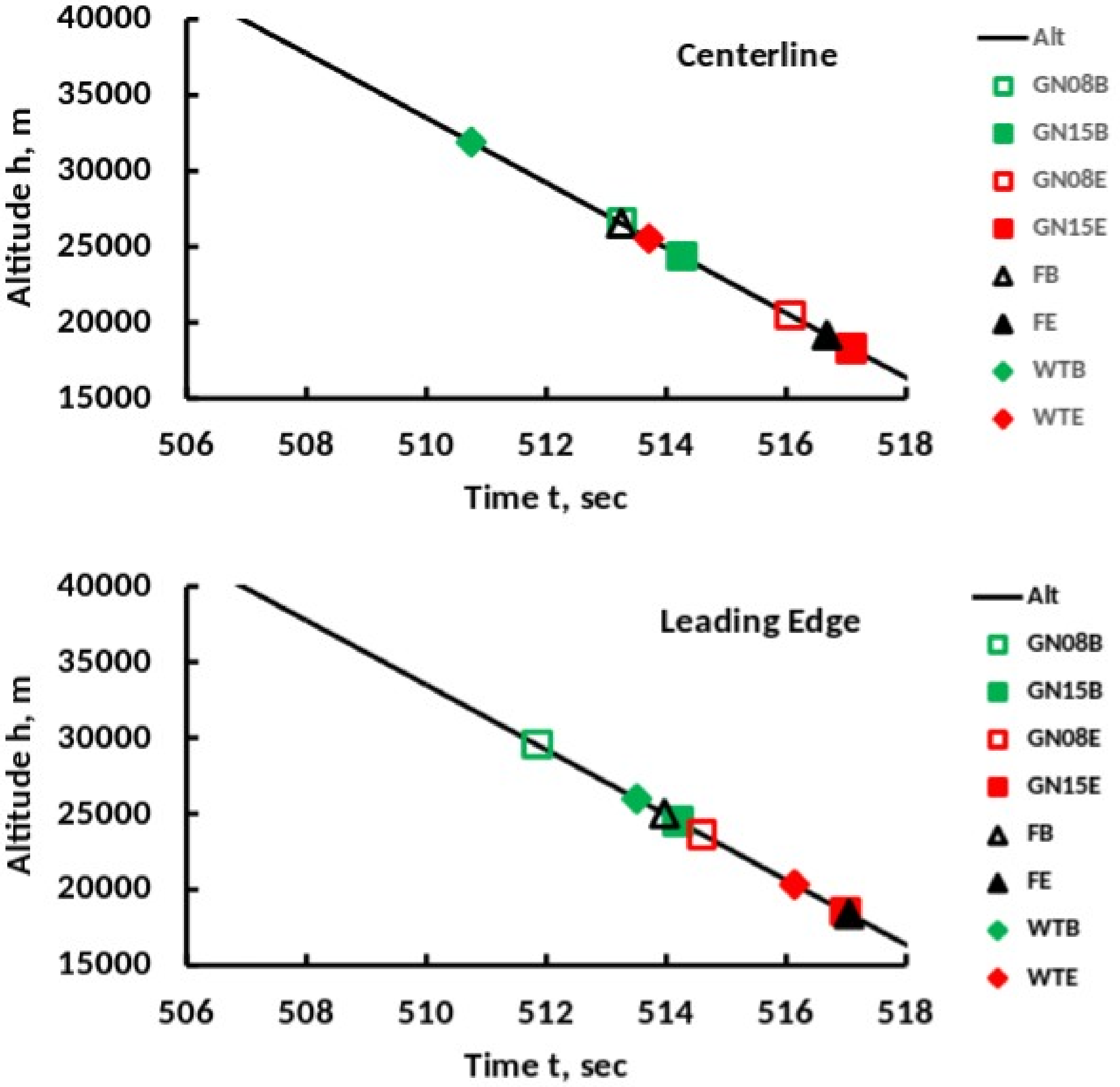

Figure 12 Preflight Predictions and Measured Transition.

Experiments were executed under conditions available in that facility, and PSE predictions were executed for a best-guess preflight trajectory. Neither experimental nor computational conditions matched flight conditions exactly, of course, as test planning evolved. This evolution is typical for any flight program. The transition Reynolds number based on freestream conditions and longitudinal distance was therefore used to translate preflight predictions to the actual trajectory. This is understood to be a very crude correlator, but in this case, its ease of application outweighed this drawback. It should be noted that for HIFiRE-5, the variation of *N*-factor with *x* was relatively linear downstream of the nose tip. For cases with transition near the nose, or where downstream flowfields are not similar, the variation of *N*-factor with *x* would not be so linear. In this case, a Reynolds number based on freestream conditions would not be a desirable correlator. Also, large excursions in parameters such as Mach number or angle of attack would make a correlation based on freestream Reynolds number less desirable.

Each prediction method, PSE or wind-tunnel-based, has a peculiar deficiency. For PSE predictions, this is the *N*-factor. A correlating *N*-factor of $8 < N < 15$ seemed appropriate, based on HIFiRE-1 and past hypersonic flight test data that were available prior to the HIFiRE-5b flight. [19] For wind tunnel measurements (in a conventional tunnel), this is wind tunnel noise, which generally tends to bias transition Reynolds number to values lower than flight.

Not only were wind tunnel transition Reynolds numbers biased by noise, they also varied with tunnel freestream unit Reynolds number. This trend is probably spurious and apparently arises from wind tunnel noise. [62] The flight comparison is based on data obtained at the highest unit Reynolds numbers. These transition Reynolds numbers were the highest, and presumably least-affected by wind tunnel noise.

A further consideration for the computational data was which computational case to use. Gosse et al. performed PSE analysis for altitudes of 21.8, 25, 28.3 and 33 km. Results for the highest altitude cases for both the leading edge and centerline exhibited peculiar behavior, with *x*-distributions of *N*-factor invariant with altitude. For the centerline at least, this behavior might have been related to the distorted boundary layer there. The h= 21.8 km case only was used to extract transition Reynolds numbers for comparison to flight for this reason. Also, it was the only case presented by Gosse et al [28] to attain $N > 15$. Choudhari et al. [27] also presented PSE computations for $h = 18$ km and 33 km. These are somewhat more difficult to interpret, since the 33 km case presented only low N-factors, and the 18 km case presented high *N*-factors immediately downstream of the nose tip.

Figure 12 illustrates how the wind tunnel tests grossly underpredict the centerline transition Reynolds number. In contrast, PSE computations with $8 < N < 15$ bracket the flight transition data. Note that the transition Reynolds number for $N = 15$ is 75% higher than for $N = 8$. However, due to the HIFiRE-5 ballistic trajectory, this change in Reynolds number occurs over a short time. For a cruising trajectory, where Reynolds number varies slowly with time, this large transition Reynolds number spread would result in large differences in predicted transition time.

For the leading edge, the wind tunnel predicted transition Reynolds number is lower than in flight, but not as drastically low as for the centerline. This result might, however, be serendipitous due to two competing effects. This is expounded upon in greater detail in Section 3.8.3. PSE predictions again bracket the flight data, with flight transition occurring near the higher end of the *N*-factor range.

Several lessons accrue from this comparison. Wind tunnel tests and predictions will probably never be at the exact conditions as flight. Therefore, some method must be used to extrapolate from one condition to another. A Reynolds number based on freestream conditions is the most simplistic but most accessible transition indicator. An edge Reynolds number, if available, would be a better choice. Wind tunnel transition generally underestimates the flight transition Reynolds number, but this is not always the case. For the leading edge, the wind tunnel transition Reynolds number was reasonably close to flight data. However, this may have merely been the result of off-setting deficiencies in the wind tunnel data.

Used judiciously, PSE-based *N*-factors were a reasonable transition correlator for HIFiRE-5, where the transition was not dominated by roughness. The designer must consider if a PSE method is appropriate, and what correlating *N*-factor to use. *N*-factor predictions for the centerline of HIFiRE-5 were somewhat suspect, due to the complex flow at this location. In the area of the centerline, the spanwise non-homogeneity of the flow violates assumptions made in the derivation of the PSE, therefore eigenmode growth in these areas should be considered in this context. For detailed discussion of this subject see Paredes et al. [91] Likewise, *N*-factor predictions for stationary crossflow must also be taken with caution due to the early nonlinearity typical of stationary crossflow instabilities. Flight data may guide the choice of correlating value for *N*. Because transition is so sensitive to initial and boundary conditions, a range of *N*-factor should be used to bracket expected conditions and provide a probability-based estimate.

3.7.2. Thermocouple Placement

Flight vehicle instrumentation for HIFiRE-5 was limited to surface-mounted sensors and data-collection devices. The weight and internal volume of the vehicle limited the number and type of sensors that can be integrated into the model. Because the flight vehicle was unlikely to be recovered intact, as described in Section 3.4, the data from the flight would also necessarily be telemetered to the ground during the flight. Telemetry by nature is bandwidth limited, meaning that the number of sensors (and data collection rates) able to fit within the bandwidth budget was also limited. A second side effect of non-recovery is that unlike other tests, for example aircraft flight testing, there would be no opportunity to re-instrument the flight vehicle and fly again if more data were desired. The combination of these factors required a high degree of planning to properly instrument the flight vehicle.

The primary instrumentation arrays used on HIFiRE-5 were Medtherm coaxial thermocouples. Thermocouples are able to provide only point measurements, as opposed to a global measurement like an externally taken IR image. [87] Following from the analyses described in Section 3.7.1, it was expected that the transition front that would be observed in flight would not be circumferentially uniform, but would vary depending on the mechanisms responsible for transition in different locations.

The preflight ground tests available at the time of instrumentation design [31, 39] were performed in noisy wind- tunnel environments. These tests showed that the area in the vicinity of 45° of azimuth transitioned due to what was presumed to be crossflow instabilities. Despite the changes known to be often introduced by testing in noisy wind-tunnel facilities, computations provided by Choudhari et al. [27] showed the location of maximum stationary crossflow growth to also located at 45° of azimuth. It could therefore reasonably be inferred that instrumentation placed in a location to measure this lobe, as seen in Figure 13 and scaled to the full flight vehicle would provide accurate information on the crossflow transition behavior.

The final instrumentation layout can be seen in Figure 14 Examination of the flight data [24] shows that the array at 45° of azimuth was well positioned to capture the leading edge of the cross-flow induced transitional front.

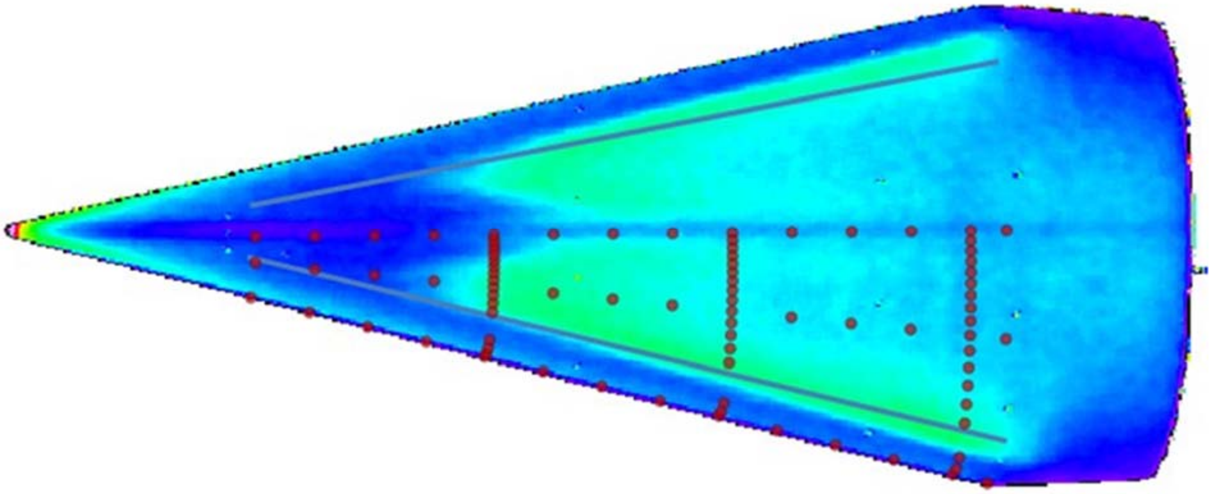

Figure 13 Proposed Thermocouples Overlaid on NASA LaRC Heat Flux Image [22]

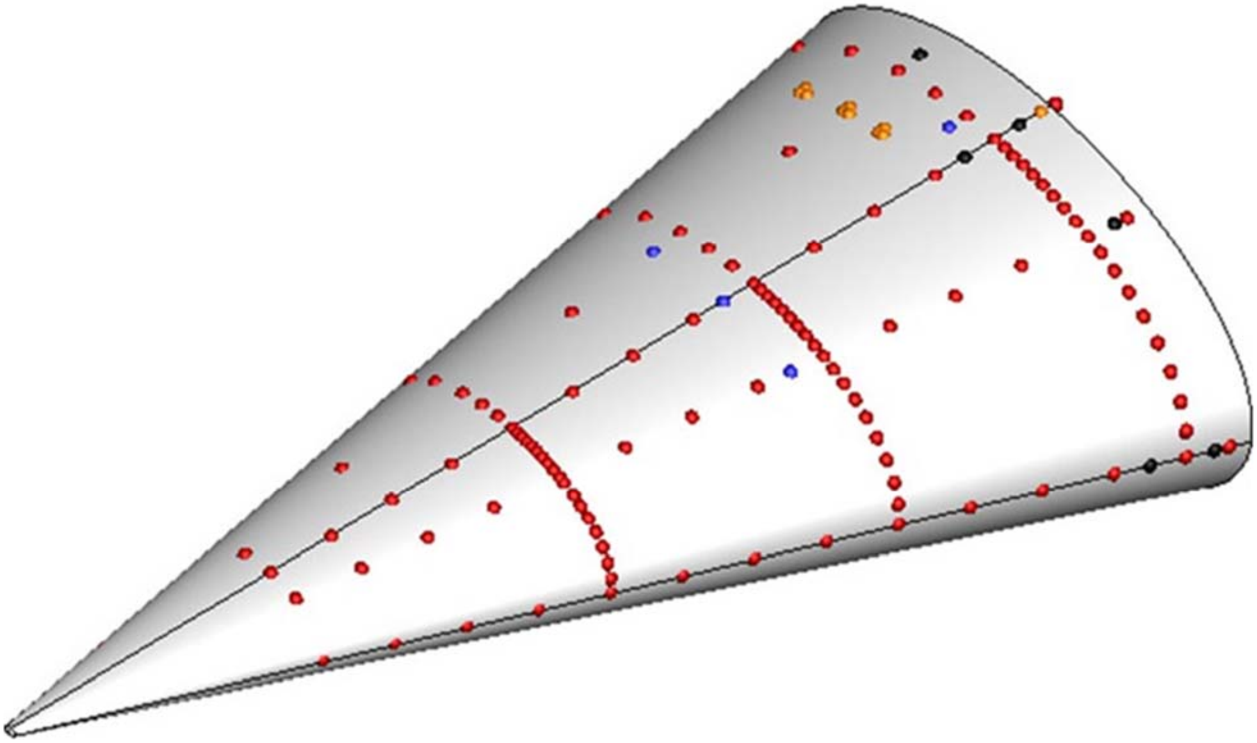

Figure 14 Instrumentation Locations, red dots denote thermocouples, blue dots denote heat-transfer gauges, black dots denote pressure taps

The choice to instrument the flight vehicle in a location where the wind-tunnel model suggests that the phenomena to be measured will occur is a straightforward one. However, in another sense, although the exact location of crossflow-induced transition as would be experienced in flight was not known, the available trends and data from ground tests as well as computations were used to inform the placement of the limited sensor array to best gather data.

Because the HIFiRE-5 had a wealth of preflight ground test and computational data to draw from, despite being a novel geometry being flown in a largely yet-untested environment, the likely outcome was well accounted for.

Given that the body of the vehicle was entirely constructed of aluminum combined with the expected heat-flux levels, it was not expected preflight that fluctuations in heating rates due to individual crossflow vortices could be detected. The azimuthal spacing of the thermocouples was therefore set to resolve the transitional front. However, post- flight it was discovered that individual crossflow vortices periodically meandered over the thermocouple sensors and provided enough of a change in heat flux as to be visible in the data. [21, 24] Additional resolution in these areas would have provided useful information on the wavenumber and physical size of crossflow vortices. In addition, vortices emanating from the vehicle nose created a complex transition field on the test article centerline that varied temporally and spatially due to vehicle dynamics. Denser instrumentation here might have better resolved this transition process.

3.7.3. Probeless Pressure Rake Analysis

A proposed instrumentation feature was a probeless rake to determine boundary-layer characteristics and parameters. [92] This type of rake had provided valuable data on the boundary layer profile in previous experiments. [93, 94] Boundary-layer instabilities are sensitive to the details of the boundary-layer profile, and having information on the state of the boundary layer would aid in analysis of the flight data.

It is known from operational experience that fins and protuberances at high speed experience significant heating rates, however, the quantitative values depend strongly on the geometry of the vehicle and the atmospheric conditions. Prior to the flight, computations made using the US3D flow solver along with an in-house developed conjugate heat transfer subroutine were used to examine the expected heating rates during the nominal conditions of the test window. This was done with the intention of examining the feasibility of installing a probeless rake just aft of the experimental section of the HIFiRE-5 vehicle. A representative contour of the calculated heat transfer is shown in Figure 15.

As can be seen in Figure 15, it was found that indeed the heating rates likely to be experienced by the fin would be very high, on the order of that experienced at the nosetip of the vehicle. A subsequent structural analysis showed that failure of the rake was likely with this level of heat transfer unless constructed from a particularly resilient material as is found on the nosetip, adding to the cost and complexity of installing such a rake.

Given the relative expense and riskiness of building the rake under these constraints, it was decided to investigate other methods of determining the boundary-layer profile. By this time, confidence in the CFD-derived flowfields had increased to the point that CFD-based boundary-layer profiles were seen as a valid method to reconstruct attitude data, heating rates, and transition to turbulence. This decision was later vindicated by the agreement between CFD-derived data [22] to experimentally measured data. [24]

A takeaway from this exercise involves the dynamic between measured and computed conditions in an experiment. As we gain increased confidence in computations, it becomes more reliable and efficient to extract some data from computations, rather than direct measurement. The researcher must judge whether a measurement is worth its cost, or whether these data might be better-derived from computation.

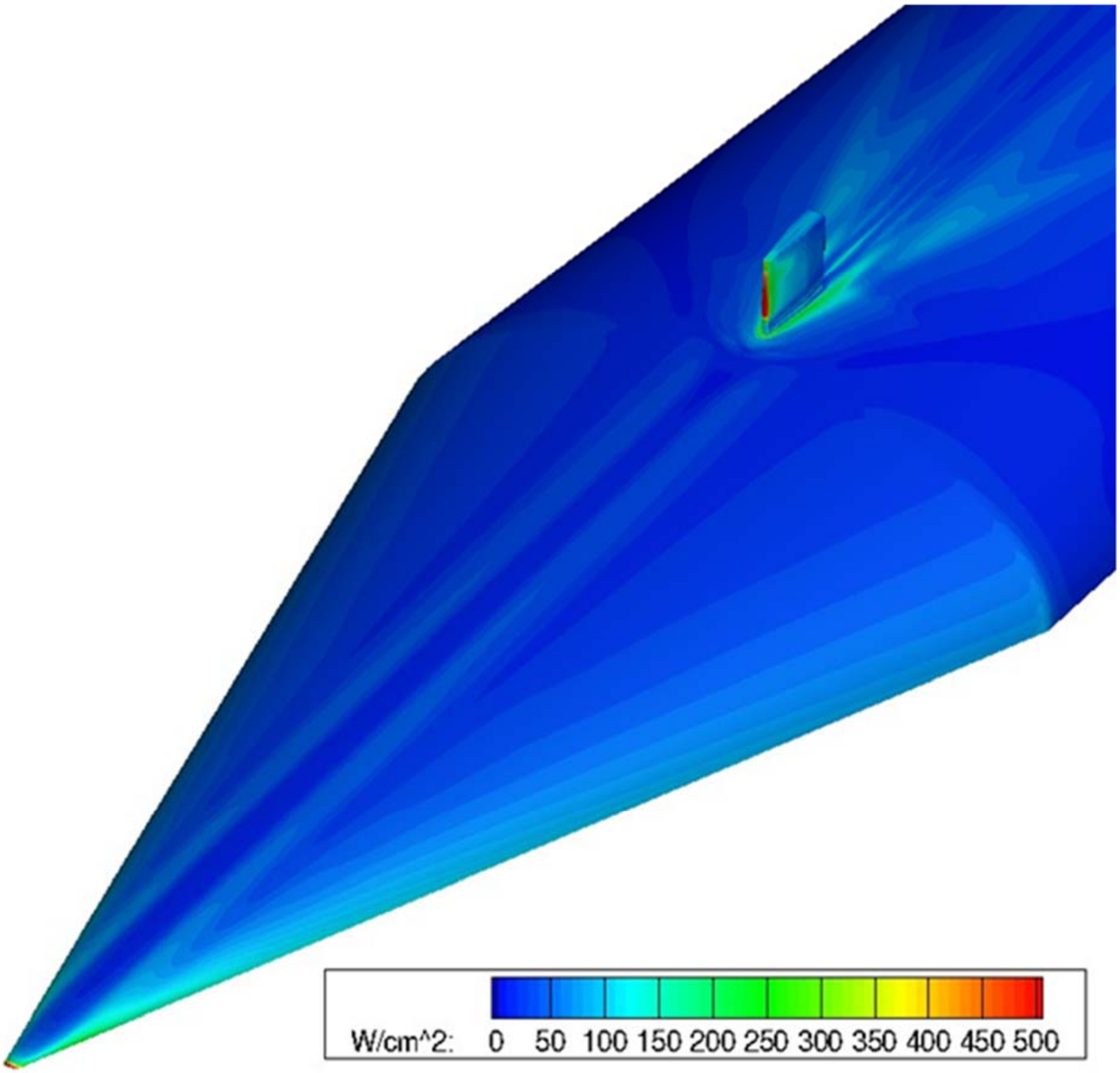

Figure 15 Heat Transfer Contours with Probeless Rake

3.7.4. Tolerances on Surface Roughness

It is known from operational experience that surface roughness can change transition behavior. Historically, the surface features of hypersonic flight vehicles were rarely characterized with sufficient care to quantify the effect roughness played in determining the transition location and pattern. [95] For this reason, there is a dearth of hard data for allowable manufacturing tolerances on hypersonic vehicles. In low-speed flows, it has been demonstrated that the local details of the flow (e.g. pressure gradient [96], relevant instabilities [97, 98, 99]) surrounding the excrescences or roughnesses play a large role in determining their effect. These data suggest that a simple criterion that does not account for these parameters is likely to have large uncertainties associated with it. It is however necessary to set a tolerance for acceptable roughnesses or excrescences from the design outer mold line, despite the difficulties in doing so. To this end, a study specific to the HIFiRE-5 geometry was undertaken.

Correlations developed from tunnel tests and CFD determined allowable roughness on HIFiRE-5b. The test article had to be instrumented and assembled, but could not contain surface fasteners that might prematurely trip the boundary layer. In one sense, the HIFiRE-5 design was more simple than the conical HIFiRE-1. This was because tripped transition due to fasteners could reasonably be expected to be contained to one side of the model, and not propagate around the leading edge attachment line. This permitted one side of HIFiRE-5 to be designed with closeout panels permitting internal access. Nevertheless, prior wind tunnel testing of elliptic cones showed that acreage transition could sometimes contaminate leading edge transition. [49]

HIFiRE-5 possessed another problematic design feature common with HIFiRE-1. Like HIFiRE-1, the HIFiRE-5 nose consisted of three materials, TZM (titanium-zirconium-molybdenum), carbon steel and stainless steel, joined to an aluminum frustum. This assembly created three joints (TZM/carbon steel, carbon steel/stainless steel and stainless steel/aluminum) with materials possessing different coefficients of thermal expansion. The primary concern for HIFiRE-5 was the leading edge of the model (major axis) where the boundary layer was thinnest. The burden on the designers was to specify step tolerances at these joints that would not trip the boundary layer during the primary descent test window.

It was impossible to adequately predict from CFD alone what roughness height would trip the boundary layer, or how transition would spread laterally from a discrete trip like a fastener. Therefore, wind tunnel tests were used to develop roughness-induced transition correlations. These results were reduced and extrapolated to flight with the aid of CFD. Tests were carried out at two wind tunnels, the NASA LaRC 20-inch Mach 6 wind tunnel, [39] and the Purdue University Boeing/Air Force Mach 6 Quiet Ludwieg Tube (BAM6QT). [32] These tunnels provided complementary capabilities. At the time HIFiRE-5 was being designed, the BAM6QT was the only operating hypersonic quiet tunnel. The LaRC tunnel provided a larger test section and higher Reynolds number capability than the BAM6QT. The LaRC model was constructed of ceramic using rapid-prototyping methods to provide thermographic phosphor imaging with multiple low-cost models. The Purdue model was a conventional machined aluminum model that permitted surface instrumentation and possessed a complex structure to create variable-height simulated joint steps.

Quiet tunnel testing was important because previous investigations had indicated that wind tunnel noise impacted tripped transition. [12] Generally, smaller trips were required to trip the flow under noisy conditions. From a designer's point of view, the noisy tunnel results would be conservative, indicating more stringent height requirements than necessary to prevent roughness from influencing transition.

Turbulence spreading was assessed in the LaRC wind tunnel. Presumably wind tunnel noise would not influence the spreading of turbulence from a trip. Discrete trips were placed on the LaRC model. These trips were square-shaped in planform, with 0.05-inch-long sides, and had varying heights. The trips were oriented in a diamond or pizza box configuration. Trips were placed slightly off the model centerline on the windward side of the model, which was at 4° angle of attack. Thermographic phosphor images indicated that the turbulence downstream of these trips did not contaminate the other side of the model. The HIFiRE-5a flight test confirmed this finding. Roughness due to nose joints was simulated on the LaRC and BAM6QT models using narrow tape strips, and also on the BAM6QT model by offsetting the model nose to create forward or backward-facing steps on the model leading edge. Diamond-shaped trips were also placed on the leading edge to explore the effect of trip geometry. The supposition was that the diamond-shaped geometry would trip more aggressively than a 2D strip, and provide a conservative estimate of allowable roughness.

Although the allowable roughness was determined from wind tunnel tests, these results needed to be extrapolated to flight. Wind tunnel results were therefore examined in terms of the critical trip height, k, normalized by the length scale $\eta *$. The critical trip height is defined as the maximum height trip that may be placed on the model without altering the transition from its smooth-body location. The length scale, $\eta *$, [100, 101] is a similarity parameter for yawed cylinders, evaluated at a reference temperature $T *$ where

$$\eta^* = \left[\frac{\nu^*}{dU_e/ds}\right]^{1/2} \tag{1}$$

and

$$T^* = 1 + 0.1(T_w - T_e) + 0.6(T_r - T_e) \tag{2}$$

For the NASA LaRC test and for the HIFiRE-5b flight, $\eta *$ values were calculated using Newtonian theory.[41] CFD solutions for the LaRC test were available, [27] at the time there was no corresponding CFD for the flight cases, and it was deemed more important to have a consistent calculation procedure. Since previous applications of the $\eta *$ scaling were for circular cylinders, there was some concern over its applicability to the HIFiRE-5 leading edge. As a check, CFD-calculated integral boundary layer thicknesses were scaled with $\eta *$ calculated with Newtonian theory to show that $\eta *$ was a consistent length scale. Sufficiently far from the nose, the integral thicknesses were a constant fraction of $\eta *$. In other words, scaling with $\eta *$ was equivalent to scaling with an integral thickness. Borg [32] later showed that, near the model nose, the Newtonian-derived $\eta *$ was about 5% higher than the CFD-derived value.

As anticipated, the 3D leading edge trip was more aggressive than a 2D strip. Noisy flow tests at LaRC indicated the effects of a 3D trip became significant at $k/\eta * \approx 0.6$. For a 2D strip, trip effects did not become significant until $k/\eta * \approx 3$. For HIFiRE-5 during descent at 18 km (the estimated end of the descent test window), these roughness heights equated to allowable 3D roughness of 4.4×10^{-5} m, and a 2D roughness of 2.2×10^{-4} m. HIFiRE-1 had demonstrated that joint steps could be held to less than 8×10^{-5} m. Since the 2D strip was expected to be conservative, the original HIFiRE-1 allowable joint step of $k = 8\times10^{-5}$ m was retained as a conservative specification.

Later tests in noisy and quiet flow in the BAM6QT validated this specification.[32] For noisy flow, allowable trip heights derived from the two wind tunnels were similar. For 3D roughness under noisy flow, the critical 3D trip height was roughly equivalent for the two tunnels, $k/\eta * \approx$

0.6. For noisy flow, the critical height for a 2D tape trip in the BAM6QT ($2.4 < k/\eta* < 2.7$) was slightly lower than in LaRC ($k/\eta* \approx 3$). Given the difficulties of measuring a critical roughness, this was considered reasonable agreement.

As expected, when tested in quiet flow, the allowable height for 3D roughness increased dramatically, from $k/\eta* \approx 0.6$ to $k/\eta* \approx 3$. Somewhat surprisingly, the allowable height for 2D roughness increased only modestly under quiet flow, from $k/\eta* \approx 2.5$ to $k/\eta* \approx 3.4$. Apparently, the effect of noise on roughness-induced transition was more significant for 3D roughness compared to 2D roughness.

This exercise in roughness specification produced several lessons. First, despite the difficulty of executing and interpreting tripped transition wind tunnel tests, they remain the only viable means of making such predictions. However, these results invariably need to be scaled from wind tunnel to flight, to account for such differences as Reynolds number, wall temperature, model scale, Mach number and so on. To perform this extrapolation, a viable scaling parameter must be chosen. The scaling variable should be extracted from the wind tunnel test and flight conditions using the same method, to ensure consistent results.

A second lesson is that wind tunnel noise influences tripped transition. An allowable roughness height based on noisy wind tunnel data is probably conservative. An intentional trip based on noisy wind tunnel data is probably underestimated. Also, the magnitude of this effect may depend on the geometry of the trip. It appears that on the HIFiRE-5 leading edge, wind tunnel noise affected 3D trips more strongly than 2D trip.

3.8. Post-Flight Data Analysis

3.8.1. Reconstruction of Attitudes

Post-flight CFD was used to determine the vehicle attitude during flight. Since angle of attack and yaw strongly influenced boundary layer transition, it was important to know the attitude of the test article. The primary method for determining the payload attitude involved combining GPS and IMU data, as was done on HIFiRE-1 and HIFiRE-5a. In this method, the IMU measured the payload attitude, relative to earth. The GPS provided the flight path angle, also relative to earth. The difference between these two angular measurements provided the vehicle AoA and yaw. [23]

However, the HIFiRE-5b flight suffered GPS and IMU anomalies. First, the vehicle suffered a GPS dropout during second stage burn. GPS data were unavailable from the start of second-stage burn to near the payload apogee. Second, the IMU suffered some drift during the entirety of the flight. The available GPS data, raw IMU acceleration and gyro rates and radar data were combined to provide a best-estimated trajectory (BET) and vehicle attitude. Because the GPS and IMU anomalies created uncertainty over this BET and attitude, CFD and measured surface pressure data provided an alternative measure of payload attitude. [21]

In this method, surface pressures were computed for the test article at a variety of Mach numbers and combinations of AoA and yaw. [22] This technique was originally applied to the HIFiRE-5a flight. [46] At each time step, this matrix of CFD data was interpolated to obtain the

AoA and yaw combination best approximating the measured surface pressure. The best attitude was defined as that which minimized the RMS difference between measured (p_F) and computed (p_{CFD}) pressures at four specified stations:

$$\bar{p} = \frac{1}{p_\infty}\left[\frac{1}{4}\sum_{i=1}^{4}(p_{CFD} - p_F)_i^2\right]^{1/2} \tag{3}$$

These four stations were at diametrically opposed points on the major and minor axes near the back of the test article. In effect, the entire payload served as a large air data probe. A best-estimated atmosphere derived from preflight balloon soundings and satellite data provided the freestream pressure, p_∞. The Mach number was obtained from the BET velocity and BEA temperature. Reynolds number and boundary layer state (laminar or turbulent) had a negligible effect on surface pressure. Measured pressures were smoothed with moving average prior to attitude determination Figure 16 (Ref. [23]) compares AoA derived from the GPS/IMU method and the measured/computed pressure method.

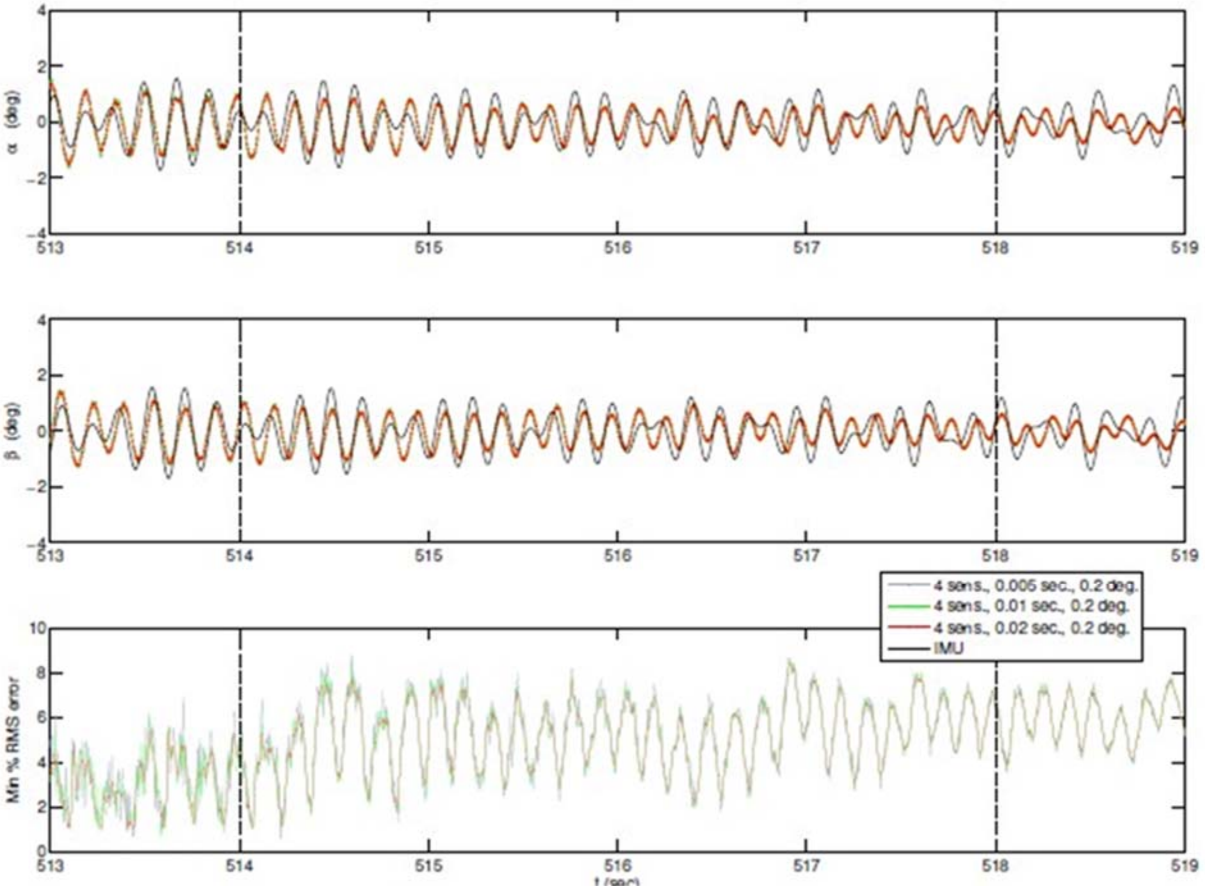

Figure 16 Pressure-based and IMU/GPS-based angle of attack and yaw for the HIFiRE-5b Flight (Jewell et al. [23])

Moving averages of 0.005, 0.01 and 0.02 seconds were applied to the pressure data. The GPS/IMU-derived and pressure-derived attitudes agreed well with each other. For later analysis, the pressure-derived attitudes were preferred over the GPS/IMU-derived attitudes, due to the GPS and IMU anomalies described above.

Several lessons accrue from this exercise. First, surface pressures are a viable means of determining the payload attitude for hypersonic flight. Hypersonic flight tests should, if possible, include some surface pressure measurements, either as a primary or secondary means of attitude determination. Second, vehicle pressure taps might be located to maximize sensitivity to attitude. The HIFiRE-5 pressure taps were located both to provide a circumferential pressure distribution and also to provide the payload attitude as described above. Although HIFiRE-5b contained 15 pressure taps, it was found that just the four diametrically-opposed pressure taps were sufficient to determine the vehicle attitude. Third, the pressure-based attitude method for HIFiRE was never fully integrated with the available GPS, IMU and radar data. In principle, all of these data might be combined using a Kalman filter to provide a best-estimated payload attitude. Fourth, the pressure-based attitude determination method depends on atmospheric observations. Reasonable efforts should be made to obtain the best quality atmospheric data. Fifth, error increased with altitude for the pressure-based attitude determination method, due to lower pressures at altitude. Low-range in addition to high-range pressure transducers might have improved signal-to-noise ratio at high altitude.

3.8.2. Interpretation of Multi-Lobed Transition Front

Because the only data available from the flight test were inferred transition locations as a function of estimated freestream conditions, it was important to use computations to examine these results. Figure 17 illustrates the flight transition front. Upon cursory inspection, the transition front appears to be more or less uniformly occurring in the neighborhood of 500 mm.

However, when viewed through the lens of combined computational data and ground-test results, it becomes apparent that the transitional front is likely made of three separate lobes, corresponding to three separate transitional mechanisms. If one considers the computational results, and sets a threshold *N*-factor at some reasonable level beyond which the flow is considered likely to transition, these can be plotted in a similar fashion to Figure 17. The results of this exercise for stationary crossflow and for Mack's second mode can be seen in Figure 18.

Further support for the causes of the different modes can be gleaned by examining parametric changes. Ground tests were performed to assess the effects of angle of attack and angle of yaw. [25] It was shown that the parametric changes seen in ground test were consistent with those observed in the flight data. For example transition on this geometry appears more sensitive to angle of yaw than to angle of attack, indicating that while the conditions are not perfectly matched, the basic physics (eigenmode growth) are being accurately captured in the ground-test campaign.

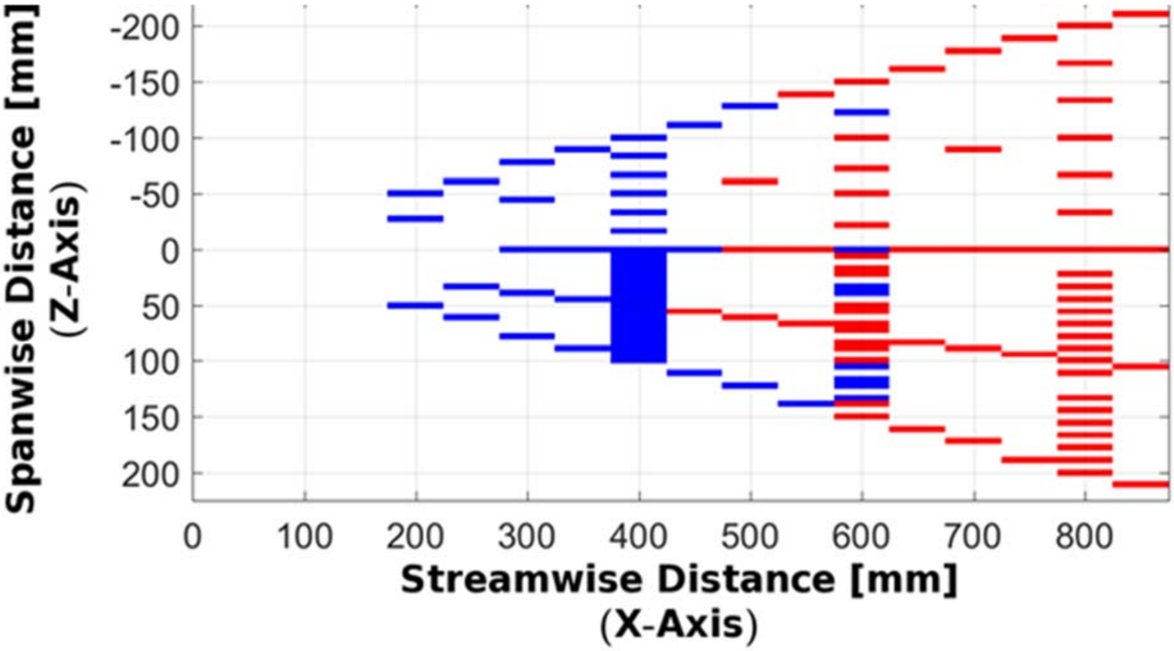

Figure 17 Thermocouple Data In-Flight, Time = 514.83 s

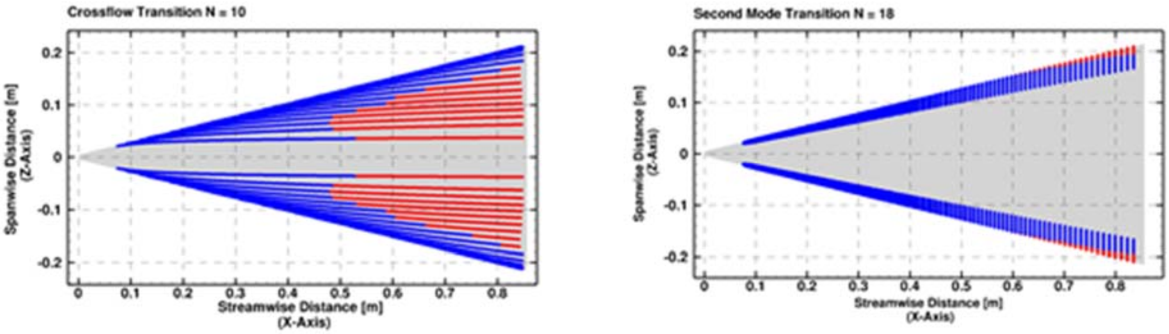

Figure 18 Computational Transition Thresholds, Flight Conditions t = 514.83 s

3.8.3. Leading-Edge Transition

As touched upon in Section 3.7.1, in preflight wind-tunnel tests performed at CUBRC, [31] the model showed a separate leading-edge transitional lobe, occurring at nearly the same Reynolds number as the centerline transitional lobe.

It was noted in Berger et al. [39] however that the leading edge transition in the LaRC tests did not appear as a distinct lobe, as it did in tests at CUBRC [31], and might therefore be a result of contamination from the acreage transition. Quiet wind tunnel tests in the BAM6QT [29, 33], also report that instead of the three-lobed transition front seen in flight, there were only two lobes present, as the leading edges remain laminar.

Because the CUBRC wind tunnel does not maintain quiet flow, and noisy flow conditions have been shown to give results that are non-intuitive in some respects [35] it was initially unclear what the cause of the change in transition front was. It is also known that increased wall-temperature ratio (hot walls) stabilize Mack's second mode instability. In other words the amplification of the initial disturbance is less. It is also thought that decreasing the noise levels experienced by a given geometry will decrease the amplitude of the initial disturbance, even though the amplification is presumably the same. Either one of these changes will push the transition front due to a given instability towards the rear of the cone.

Post-flight it was suggested that the distinct CUBRC leading edge transition lobe was evident due to the high cooling of the model wall, which more closely matched the flight test. [1] It is possible that acreage contamination to the leading edge in the LaRC test may have compensated for the higher wall-to-stagnation temperature ratio in the LaRC case.

To investigate this, a CFD effort calculated a HIFiRE-5 flight vehicle under atmospheric conditions, but using the wind-tunnel wall-temperature ratio. *N*-factors for the Mack's second mode instability along the leading edge can be seen in **Figure 19**. **Figure 19**, shows that if the HIFiRE-5 had flown at the wall-temperature ratio seen in the wind- tunnel tests, leading-edge transition would not be expected due to the low amplification rates. Likewise, calculation of Mack's second mode *N*-factors for the conditions experienced in the quiet-flow BAM6QT cases, [25] seen in Figure 20 indicate that transition is unlikely due to low amplification. This agrees with the results of Borg et al. [33] and Borg & Kimmel [25] which did not observe natural leading edge transition under quiet flow nor noisy flow conditions.

By taking into account the combined picture of ground test results as well as computations, what might have been an unknown anomaly (the disappearance and reappearance of leading edge transition) can reasonably be attributed to the effect of wall-temperature ratio. This allows this change to be accounted for in future interpretations.

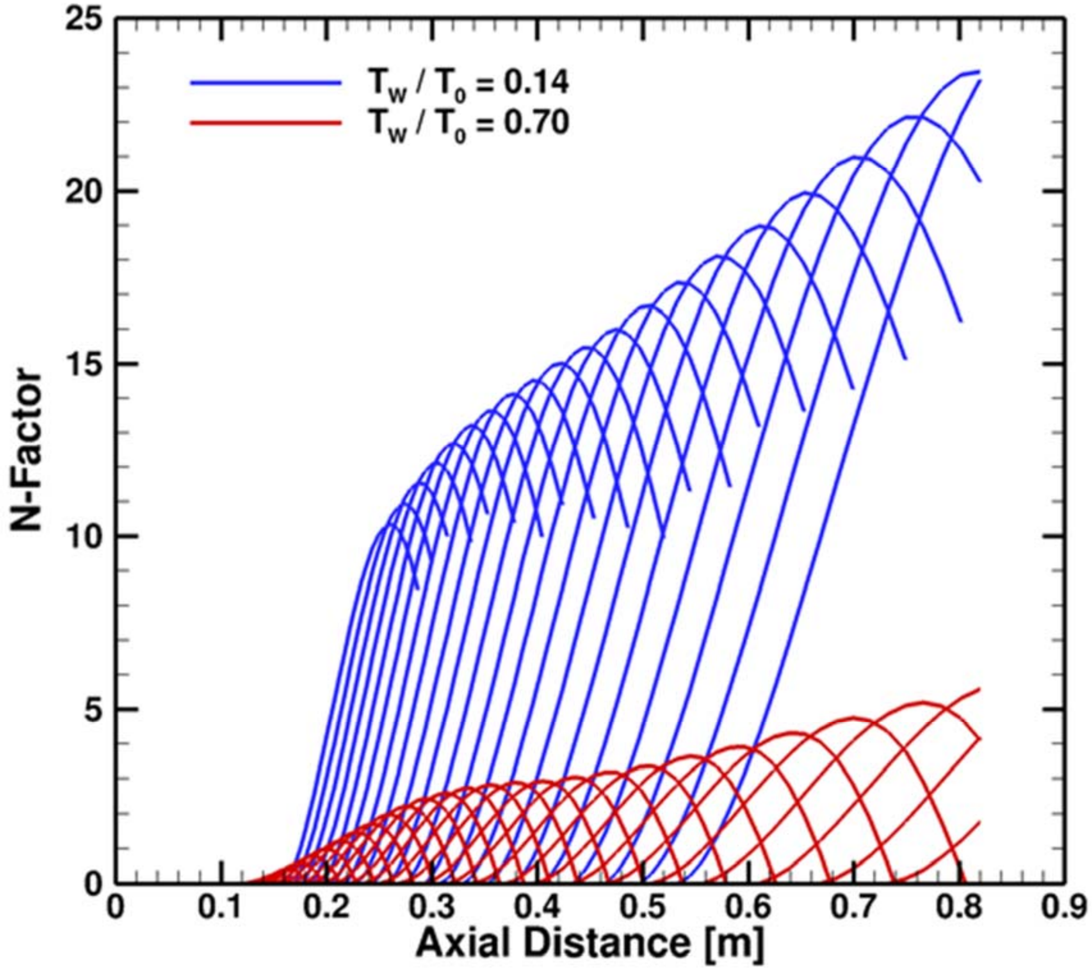

Figure 19 HF5 Attachment Line, 2nd Mode LST N-factors, Flight Conditions

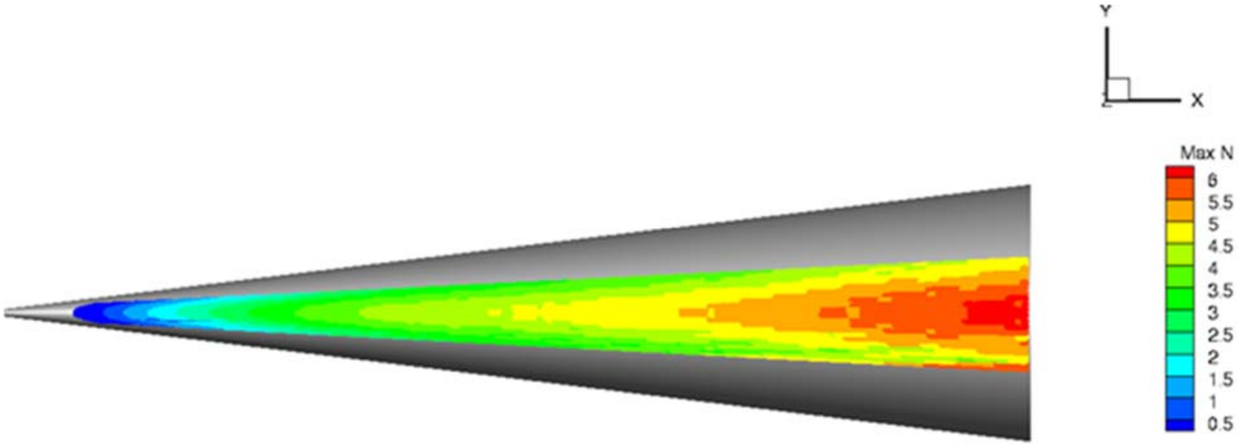

Figure 20 HF5 Attachment Line, 2nd Mode LST N-factor Contours, BAM6QT Conditions

The availability of the flight data also allows for the calibration of transition *N*-factors for hypersonic flight. So in addition to using ground test data and computations to design the experiment and interpret the data correctly, flight test data allows us to calibrate the choice of transition *N*-factors more accurately when new geometries are being considered.

3.9. Summary and Conclusions

Kimmel et al. [1] explicitly states that the most significant contribution from the HIFiRE boundary-layer experiments may be the confirmation of agreement in phenomenological behavior between flight test results, ground test results, and computational results. Although the full transition process has yet to be understood, all three sets of results are consistent with the current understanding of the underlying physics and methods of prediction.

Prior to the HIFiRE flights, two broad categories of data were available. The first category was ground testing data, which provided transition locations, as well as detailed frequency and heat-transfer data for the flow conditions not directly applicable to real flight vehicles. The second category were computational, which provided only the amplification ratios of specifically chosen instabilities. By using computational information to translate the data given by imperfect ground testing results, a fairly complete picture of the expected transitional behavior was able to be formed. Preflight analysis and computations were able to predict the transition location, and thus define the test window for an un-flown geometry, by some measures within about 30% of the actual in-flight data.

After the HIFiRE flights, the community possessed well-characterized flight data to anchor future ground test campaigns and computational efforts. The HIFiRE flights provide calibration data for *N*-factor predictions. The user must consider that the *N*-factor method is fundamentally a correlation, with all the pitfalls and vagaries of any other correlation. Used judiciously, however, HIFiRE might be expected to provide reasoned bounds on *N*-factors for reasonably smooth bodies. Certainly, the flight tests demonstrated the dominant effect of wind tunnel noise on ground tests.

HIFiRE-5 returned only transition location on the surface as a function of estimated freestream conditions. How- ever, with effort to tie these data together with computation and ground test results, one may form a cohesive picture including the mechanisms responsible for transition to turbulence in different locations on the surface that is much more valuable than the sum of its parts.

3.10. Lessons Learned

- Because of the sensitivity of transition to initial conditions, a range of transition N-factors should be used to bracket the expected transition location and provide a probability-based estimate.

- Collaboration was baked into the HIFiRE-5 test from the beginning, an extensive set of preflight ground tests and computational efforts were performed before any flight test took place. Even though the individual efforts provided imperfect data, the limitations of these tests were explicitly identified and considered when implementing findings from each. Thus the inadequate aspects of any individual data set were buttressed by drawing from other available data, and doing so helped ensure a successful outcome of the flight experiments.

- Because the flow conditions for in flight tests are necessarily dependent on atmospheric conditions and the attitude of the vehicle, there should be several redundant methods of determining the vehicle orientation. To this end it is noted that surface pressure measurements are a viable means of determining the payload attitude for hypersonic flight. In the case of HIFiRE-5 despite anomalies in both IMU and GPS data, payload attitude able to be reconstructed, due to surface pressures being available. However, it should be noted that pressure-based attitude determination method depends on atmospheric observations at the time of launch.

- Wind tunnel transition will generally underestimate the flight transition Reynolds number, due to the differences in freestream noise characteristics. This situation is not always the case, however, computations of both wind- tunnel and flight conditions provide guidance on phenomenological trends.

- Despite the difficulty and limitations of intentionally tripped wind tunnel tests, they remain the only viable means of making predictions about roughness heights. Allowable roughness height based on noisy wind tunnel data is probably conservative, while intentional boundary-layer trips based on noisy wind tunnel data are likely to be undersized. The magnitude of this effect may depend on the geometry of the trip.

- Scaling variables used to extrapolate wind-tunnel data to flight, should be extracted using a consistent method.

4. Transition on a Variable Bluntness 7° Cone at High Reynolds Number

4.1. Introduction

Between 1978 and 1982, K. F. Stetson performed a total of 196 sharp- and blunt-cone experiments [102] on a thin-walled 8° half-angle, 4 in.-base cone in the Air Force Research Laboratory (AFRL) Mach 6 High Reynolds Number facility. These experiments were reported in a 1983 paper [63] along with results from AEDC Tunnel F with a larger cone at Mach 9. The AFRL Mach 6 results recently received computational analysis [64] indicating that the Mack second mode was unlikely to be the dominant instability mechanism for nose tips with radius larger than 1 mm. In the present work, a total of 132 sharp- and blunt-cone experiments were performed on a smooth, thick-walled 7° half-angle, 4 in.-base cone at 0° AoA in the same facility, and similar computational analysis indicates that the dominant instability mechanism for the bluntest cases is, again, not the second mode.

The AFRL Mach 6 facility operates at stagnation pressure p_0 from 700 to 2100 psi. Details of these conditions, along with an intermediate case, are presented in Table 3. These conditions encompass the operating envelope of the AFRL Mach 6 High Reynolds Number facility. A total of 65 experiments at unique conditions comprise the present Mach 6 results (see Section 4.3). Mean-flow and stability calculations for each condition were performed at a computational cost of about 100 processor-hours each.

Table 3 Summary of sample inflow conditions computed for each bluntness value, with one intermediate value presented.

p_0		unit Re_∞	M_∞	ρ_∞	P_∞	T_∞	U_∞	T_w/T_0
[psi]	[MPa]	$\times 10^6$/m	-	[kg/m3]	[kPa]	[K]	[m/s]	-
700	4.83	30.7	5.9	0.154	3.40	76.7	1038	0.56
1400	9.65	61.4	5.9	0.308	6.80	76.7	1038	0.56
2100	14.5	92.1	5.9	0.461	10.2	76.7	1038	0.56

4.2. Computational Methods

The mean flow over the cone is computed by the reacting, axisymmetric Navier-Stokes equations with a structured grid, using a version of the NASA Data Parallel-Line Relaxation (DPLR) code [103] which is included as part of the STABL software suite, as described by Johnson [104] and Johnson et al. [105] This flow solver is based on the finite-volume formulation. The use of an excluded volume equation of state is not necessary for the boundary layer solver because the static pressure over the cone is sufficiently low (typically, 10–50 kPa) that the gas can be treated as ideal. The mean flow is computed on a single-block, structured grid (see Figure 21) with dimensions of 361 cells by 359 cells in the streamwise and wall-normal directions, respectively. For clarity, every fifth wall-normal cell is shown. The inflow gas composition in each case is air with 0.233 O_2 and 0.767 N_2 mass fractions. While the computation includes chemistry, the impact of chemical reactions is negligible, as the local maximum temperature does not exceed 611 K for any case.

Grids for the sharp 7° half angle cone and each of the 6 bluntness conditions (see Table 4) were generated using STABL's built-in grid generator, and mean flow solutions examined to ensure that at least 100 points were placed in the boundary layer for each stagnation pressure. For simplicity and to match the Stetson [63] nomenclature, bluntness as a percentage of the base radius of 2.0 inches is used to label the cases analyzed in the present work. The boundary-layer profiles and edge properties were extracted from the mean flow solutions during post-processing. The wall-normal span of the grid increased down the length of the cone, from 0.25 mm at the tip to 50 mm at the base, allowing for the shock to be fully contained within the grid for all cases tested. The grid was clustered at the wall as well as at the nose in order to capture the gradients in these locations. The Δy^+ value for the grid, extracted from the DPLR solution for each case, is everywhere less than 1, where Δy^+ is a measure of local grid quality at the wall in the wall-normal direction.

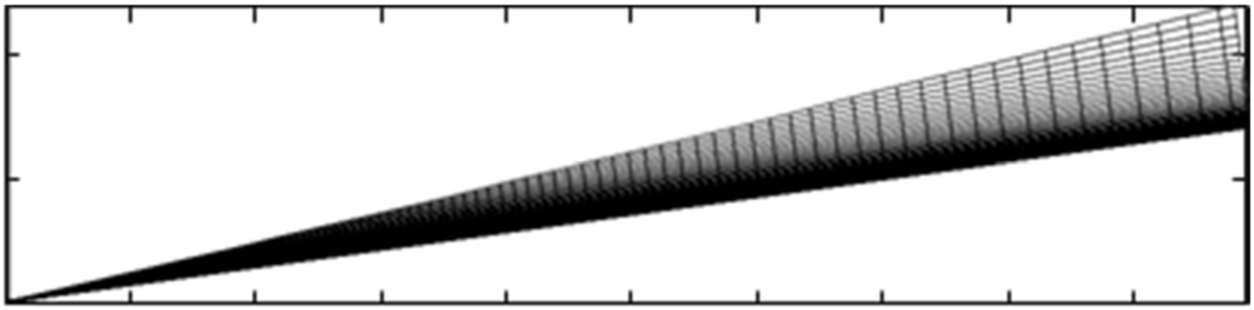

Figure 21 Grid for the sharp cone case with 361 streamwise and 359 wall-normal cells.

Table 4 Summary of grids generated for the present study, each corresponding to a different sharp or blunt nose tip used in the present study.

R_N		Bluntness
in.	mm	%
0	0	0
0.02	0.508	1
0.06	1.524	3
0.10	2.540	5
0.20	5.080	10
0.40	10.16	20
0.60	15.24	30

4.3. Mean Flow-Based Transition Correlations

Following Stetson [63] and Jewell and Kimmel [64] results were reported by normalizing the transition Reynolds numbers for blunted cones by the transition Reynolds numbers for sharp cones at the same inflow conditions, which were calculated as:

$$\frac{x_{Tr_b}}{x_{Tr_s}} = \frac{(Re_{x_e})_{Tr_b}}{(Re_{x_e})_{Tr_s}} \frac{(Re_{unit})_{e_s}}{(Re_{unit})_{e_b}} \tag{4}$$

Here, subscript *S* indicates values for a sharp tip, *B* values for a given blunt tip at the same condition, and *e* conditions at the boundary layer edge. The boundary layer edge, throughout the present work, is defined as the point at which the derivative of the enthalpy along a line extending orthogonally from the surface of the cone approaches zero.

The entropy layer swallowing length estimate of Rotta [106] (X_{SW}), as applied by Stetson and Rushton, [69] is also used to correlate the results. The entropy layer is depicted directly by using the DPLR solution for each case (gas composition, temperature, and pressure) as the input for an entropy calculation at each cell, which is performed using the Cantera [107] thermodynamics software.

Figure 9 in Stetson [63] summarizes his results, and was recreated using the transition locations reported in Stetson [102] and new condition computations in Figures 5 and 6 of Jewell and Kimmel. [64] The present 7° results are compared to the historical data below as Figure 22 and Figure 23. Data in these figures are normalized by the swallowing length of Rotta [106].

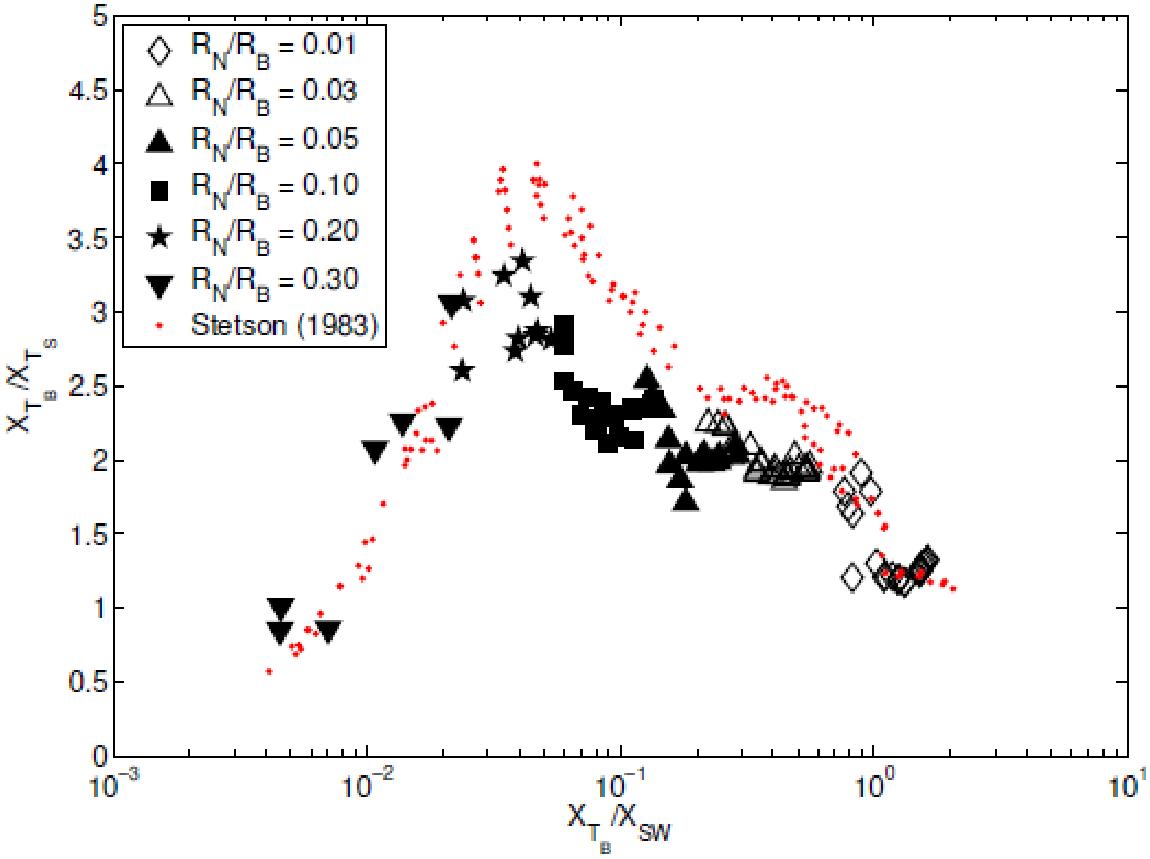

Figure 22 Ratio of blunt-to-sharp transition location on an 8° cone (red dots) from Figure 9(a) of Stetson [63] recalculated in Jewell and Kimmel [64] and 7° cone.

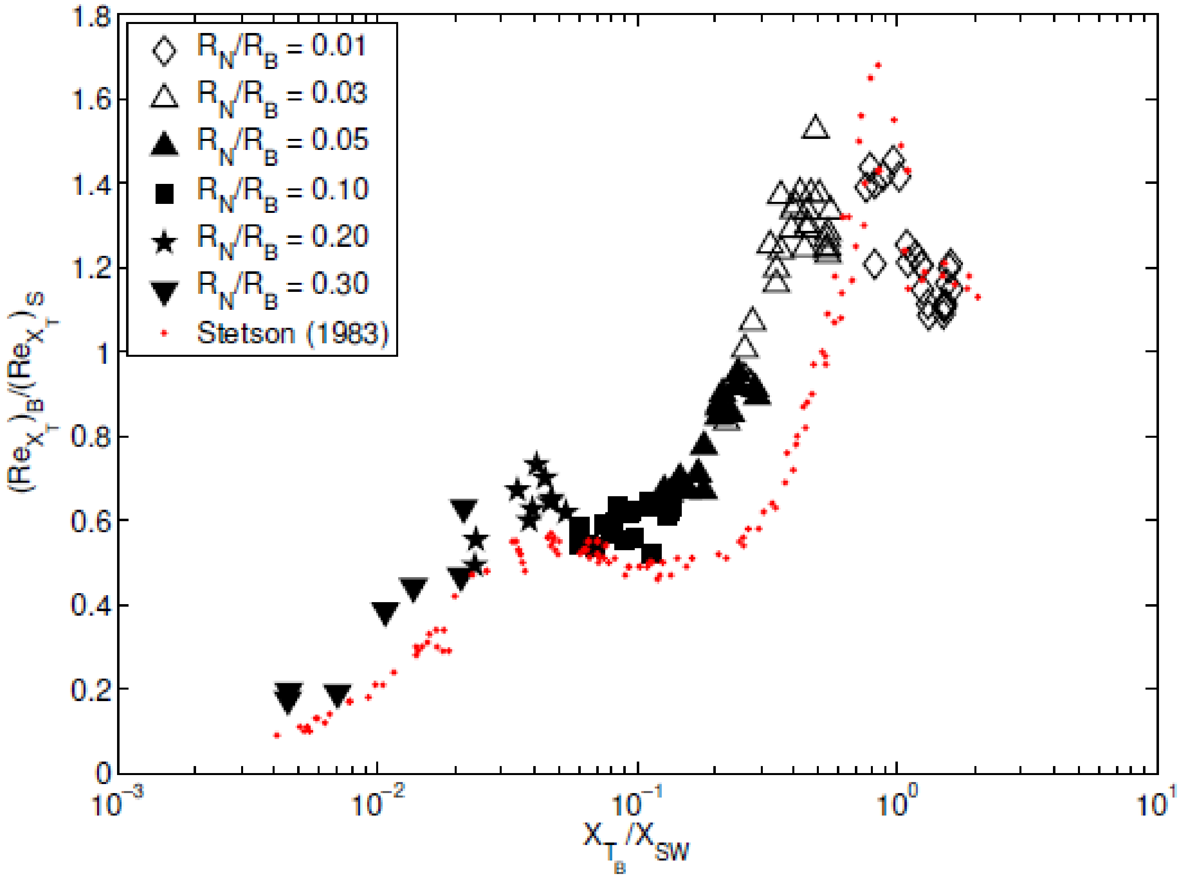

Figure 23 Ratio of blunt-to-sharp transition Reynolds number on an 8° cone (red dots) from Figure 9(a) of Stetson [63] recalculated in Jewell and Kimmel [64] and 7° cone.

4.4. Stability Computations

The stability analyses are performed using the PSE-Chem solver, which is also part of the STABL software suite. PSE-Chem [108] solves the reacting, two-dimensional, axisymmetric, linear parabolized stability equations (PSE) to predict the amplification of disturbances as they interact with the boundary layer. The PSE-Chem solver includes finite-rate chemistry and translational-vibrational energy exchange. The parabolized stability equations predict the amplification of disturbances as they interact with the boundary layer.

The band of amplified frequencies within the boundary layer predicted by Linear Stability Theory (LST) is presented in a contour plot in terms of amplification $-\alpha_i$ in Figure 24 for three cases equivalent to experiments in the present data set. The most amplified frequency predicted by a simple model based on edge velocity and boundary layer thickness is also plotted for each case, and shows generally good agreement with the detailed computations. The unstable region rises slightly in frequency space with increasing pressure over the range of these three cases, as the boundary layer thins. The subset of these plots from $s = 0.1217$–0.2276 m is comparable to the experimental data presented in Figure 29 for the same conditions.

In the present work the focus was on the 2D second mode, which should be dominant above approximately Mach 4.5 [109] for conical geometry with significant wall cooling. Frequencies low enough to include the 2D first mode were also examined comprehensively, and oblique first modes were included in the computation for a subset of the blunt cases, but significant amplification was not observed in the computational results for any of these. Marineau et al. [70] also did not observe strong first-mode activity in experimental results derived from a ray of surface mounted pressure transducers, and Jewell and Kimmel [64] performed oblique mode analysis that excluded these modes as the dominant instability mechanism for the blunter cases as well. Similar systematic analysis of the present data set also confirms their exclusion as the dominant instability mechanism.

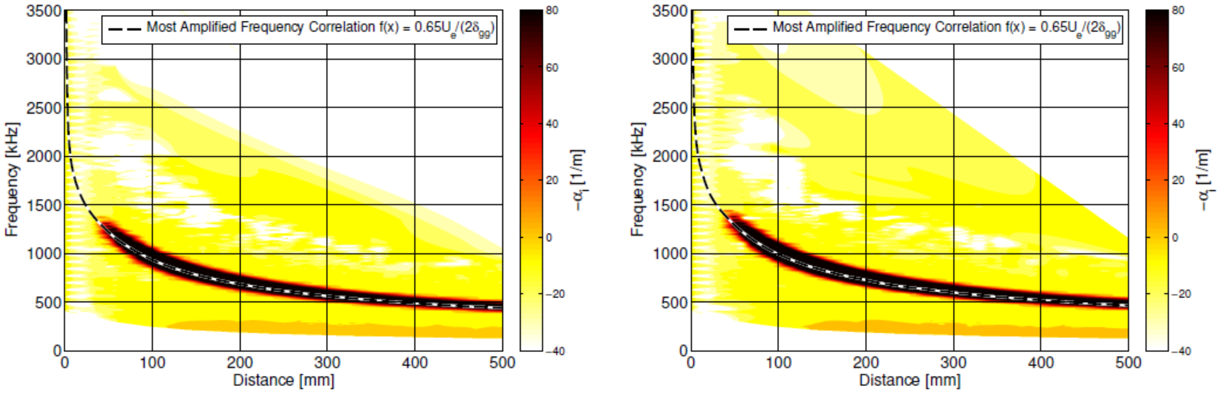

(a) Run 450 (p_0 =706.3 psi)

(b) Run 452 (p_0 =802.1 psi)

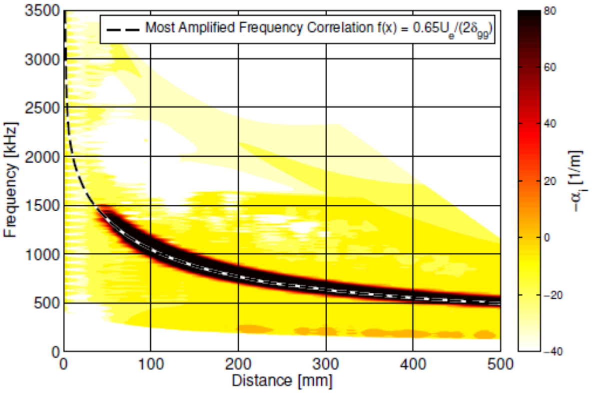

(c) Run 453 (p_0 =902.6 psi)

Figure 24 LST contours of α^i for R_N = 0.508 mm (1%) for three inflow conditions, showing good agreement with a simple frequency correlation for this mildly-blunt case. (Compare with Figure 29).

Computed second mode *N*-factors at the experimental transition location are presented in Figure 24. A strong trend with both nose tip bluntness and swallowing length ratio is observed. Note that the sharp data points (noted with an arrow) are located at infinity on the *x*-axis, as the swallowing length approaches infinity, and appear to be the asymptotic value for *N*-factor at transition with decreasing nose tip bluntness. Three regions are evident: for $X_T/X_{SW} < 0.3$, the computed *N*-factors at transition are less than one, indicating that modal growth is minimal and implying that an alternate transition mechanism is important in this region, which is populated by the blunter cases. Marineau et al.,[70] who observed a similar effect, propose that transient growth [110] or entropy-layer instability [111] may be plausible candidate mechanisms. From $0.3 < X_T/X_{SW} < 1.0$, the computed N-factor of transition rapidly increases. In this region, significant modal growth occurs and may compete with other mechanisms to provoke laminar-turbulent transition. For $X_T/X_{SW} > 1.0$, which includes the sharpest cones in the data set, a consistent computed transition N-factor, falling within a range of 6.3 to 7.7, is observed. This result is consistent with Mack's second mode [109] as the dominant instability mechanism for the sharpest cases, and also agrees with the analysis of Jewell and Kimmel. [64]

The region in which the second mode is significant may be defined by Mach number at the boundary layer edge, which in Figure 25a is presented at the measured point of transition as a function of X_T/X_{SW}. Figure 25b presents the variation of computed N-factor at the measured transition location as a function of edge Mach number, with the edge Mach number computed at the peak enthalpy overshoot, as described in Jewell and Kimmel. [64] This consistent definition of the boundary layer is useful for examining trends, although it may understate boundary layer height, and therefore edge Mach number. The maximum computed second mode N-factors occur for $M_e > 4.5$, while small second mode N-factors are computed for $M_e < 3.9$, which is consistent with the predictions of Mack [109] for the variation in the strength of the second-mode instability with Mach number. As bluntness and resultant entropy layer swallowing length effectively mediate the edge Mach number, this may be the effect by which the second mode is emphasized or de-emphasized in the transition process, but it does not indicate the alternate mechanism for instability which is important in the blunter cases with lower edge Mach number. This analysis is consistent with Jewell and Kimmel. [64]

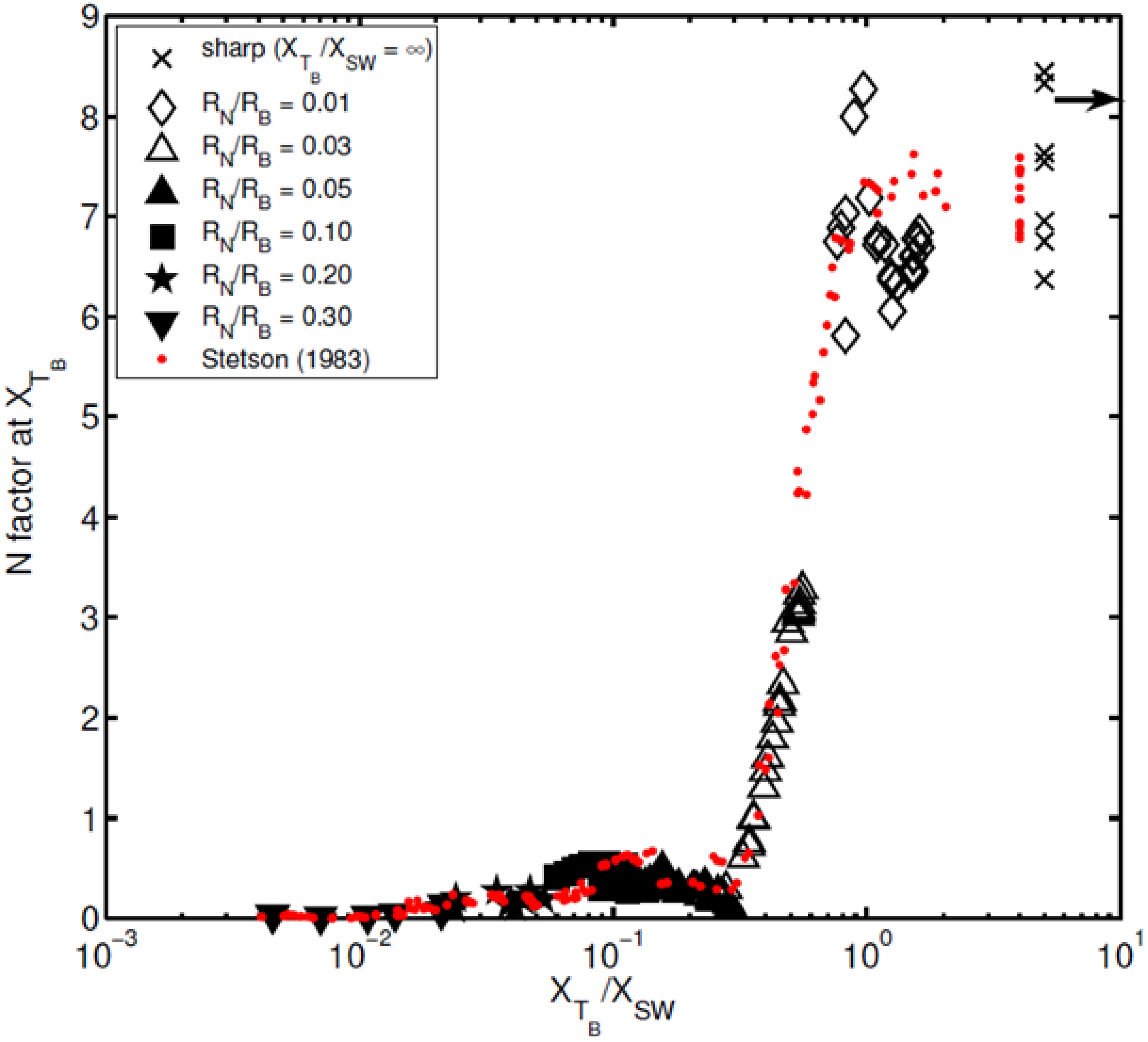

Figure 25 Computed N-factor at experimental transition location compared with data (red dots) from Jewell and Kimmel [64]

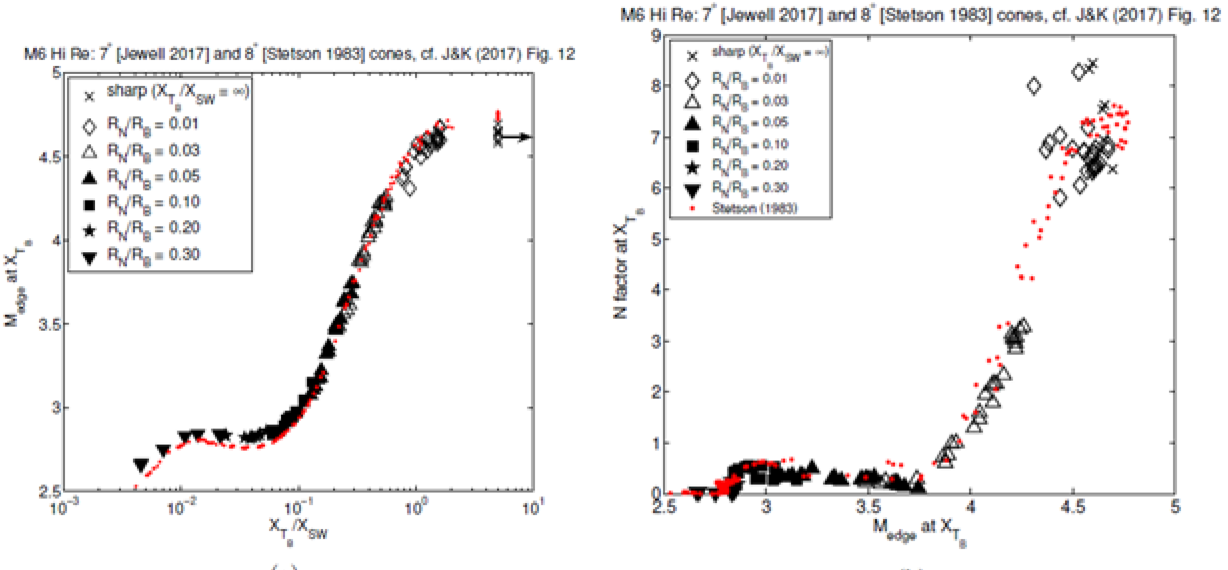

(a) (b)

Figure 26 Edge Mach number effects in the present data set.

4.5. High Speed Schlieren Analysis

Recently, the development of second-mode instabilities within hypersonic boundary layers has been examined using high-speed schlieren visualizations. [112, 113, 114] This technique has enabled the reduction of quantitative data on harmonic content and propagation speeds from schlieren videos acquired at Mach 10 and Mach 14. Similar analysis has been carried out for a subset of the experiments described above, using a Phantom v2512 camera recording at 368,421 frames per second (i.e., a 2.71 µs period). The camera resolution was 1280 48 pixels at 0.0827 mm/pixel, with a viewing area along the cone from s = 0.1217–0.2276 m. The illumination source was a synchronized Cavilux HF laser (810 nm wavelength) with pulse width 30 ns.

Following the procedure of Kennedy et al., [114] the resulting schlieren images were enhanced (see Figure 27 for an example, enlarged in Matlab using bicubic interpolation to 4 times the original size) and examined for regions of quiescent flow, laminar flow with visible instabilities, and turbulent flow. Figure 27 displays (left to right) laminar flow with rope-like second mode instability features, an apparently quiescent region, and a turbulent region. The boundary layer in this image, and in Figure 28 is 6 pixels or ~0.50 mm thick, and the viewing area is *s*=0.1525-0.2024 m. The boundary layers imaged in the present study are approximately 0.50 mm (6 pixels) thick in the region where second mode instability features are visible, which is substantially thinner than the boundary layers imaged by Kennedy et al., [114] which ranged from 5.0 to 7.5 mm thick.

Figure 28 presents a sequence of 11 schlieren video frames covering covering 27.1 µs from an experiment with R_N = 0.508 mm (1%). These images have been enhanced via subtracting an average image, generated by averaging 1000 images, from each image of interest. In this figure two white lines marking the left and right edges of a wavepacket have been added to facilitate visual tracking. The white lines in the first image indicate the extent of the identified wavepacket, and they are propagated downstream in subsequent images using the average calculated wavepacket propagation speed. Figure 28 covers 27.1 μs. Each image is 10.59 cm long.

Wavepacket propagation speeds are calculated using a cross correlation between sequential images. Speeds were calculated from 5000 images (13.6 ms, or ~12.2 m of flow length) in the middle of each run time.

Wavepackets are identified through a Matlab implementation of the MUSIC (Multiple Signal Classification) algorithm. [115] The number of wavepackets used for the calculation is different for each run, because more than one strong wavepacket may be present in a single image. Typically, the standard deviations are 5–7% (95% confidence interval), which would improve with more pixels in the boundary layer, which would increase the correlation coefficient through a higher-fidelity recording of the waves. Propagation speed calculation results from four experiments are presented in Table 5. Turbulent convection velocities are not calculated, because the cross-correlation does not produce a peak. The calculated disturbance speeds are about 93% of the computed boundary layer edge velocity, which is close to previously reported second mode wavepacket propagation speeds at higher Mach number, [114] as well as leading-edge values for turbulent spot propagation speeds at similar Mach numbers. [116]

Spatial and frequency features of the wavepacket ensembles reported in Table 5 were analyzed. Pixel intensity versus time signals were reconstructed at the y/δ location of largest disturbance amplitude and interpolation was used to remain at the fixed y/δ location as the boundary layer grew downstream. The signals were generated, as above, from 5000 images (13.6 ms) from each run. Spectra were computed using Welch's method averaging 200 windows with 50% overlap, with a Blackman windowing function applied. Results of this analysis for three conditions are presented in Figure 29. Note that the color scale is uncalibrated logarithmic arbitrary units. As in Figure 24, the unstable region rises slightly in frequency space with increasing pressure over the range of these three cases, as the boundary layer thins. The transition front, visible as a region of broadband disturbances downstream of the narrowband instability, also clearly moves forward with increasing pressure (this feature does not appear in the Figure 24 contours, as LST does not model turbulence).

Results become more noisy with higher p_0, and the highest pressure at which data that were deemed suitable for wavepacket analysis were acquired was the p_0 = 902.6 psi case. While experiments were performed at higher pressures, the cross-correlation and frequency extraction for these cases were significantly more noisy. This noise may be associated with insufficient pixel resolution in the boundary layer - the minimum number of pixels at p_0 = 902.6 psi was about 4.5 in the upstream region, and there were even fewer in the thinner boundary layers at higher pressure. Furthermore, there are no clear harmonics present in the spectra presented in Figure 29 and Figure 30. This may also be a consequence of relatively low pixel counts in the extremely thin boundary layers. The banding at 400 kHz observed at higher Reynolds numbers may be an artifact, but is also possibly subharmonic resonance of the second mode. [117]

Figure 30(a) presents spectra observed from Run 450 (p_0 =706.3 psi) at four different streamwise stations from s = 0.141–0.165 m. As the boundary layer thickens with increasing downstream distance, the peak frequency decreases and the magnitude of the peak (again, in arbitrary units) increases. The peak frequencies for this case at these four locations are compared with interpolated LST and PST peak instability frequencies, computed with STABL-2D in Section 4.5, in Figure 30(b). For LST, the reported frequencies are taken from the peak of the contour plot in Figure 24. For PSE, the reported frequencies are those associated with the largest predicted *N*-factor at each *s*-location. Both LST and PSE curves exhibit the same general trend as the schlieren-derived peaks, but the PSE frequencies agree much more closely with the experimentally measured case. LST has a lower frequency as the peak growth occurs at a lower frequency than the peak amplitude. [118]

Figure 27 Run 450 (P0 = 706.3 psi) enhanced schlieren detail

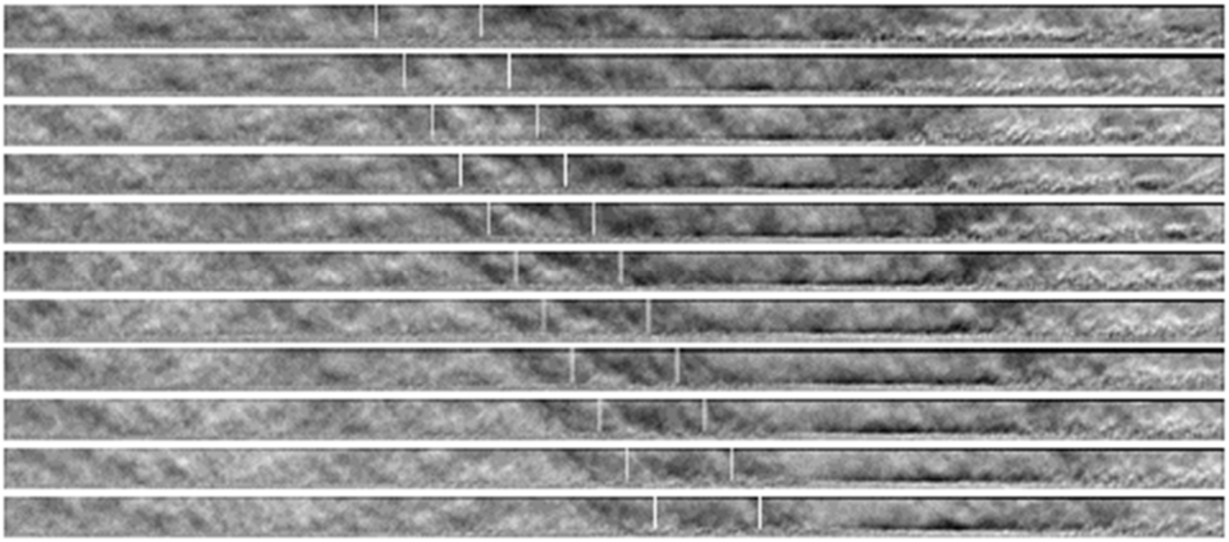

Figure 28 Run 450 (P0 = 706.3 psi) enhanced schlieren sequence (full)

Table 5 Mean wavepacket propagation speeds calculated by cross correlating 5000 sequential images (135.5 ms) from each experiment.

Run	p_0 psi	T_0 °R	$\bar{U}_{prop}$ m/s	$\bar{U}_{prop}/U_e$	σ m/s	2σ error %	No. of wavepackets
450	706.3	1009	890.8	0.922	26.5	5.96	5615
451	705.6	1008	893.8	0.929	26.3	5.88	5742
452	802.1	1007	896.6	0.932	33.3	7.42	7010
453	902.6	1008	892.2	0.927	27.0	6.06	7000

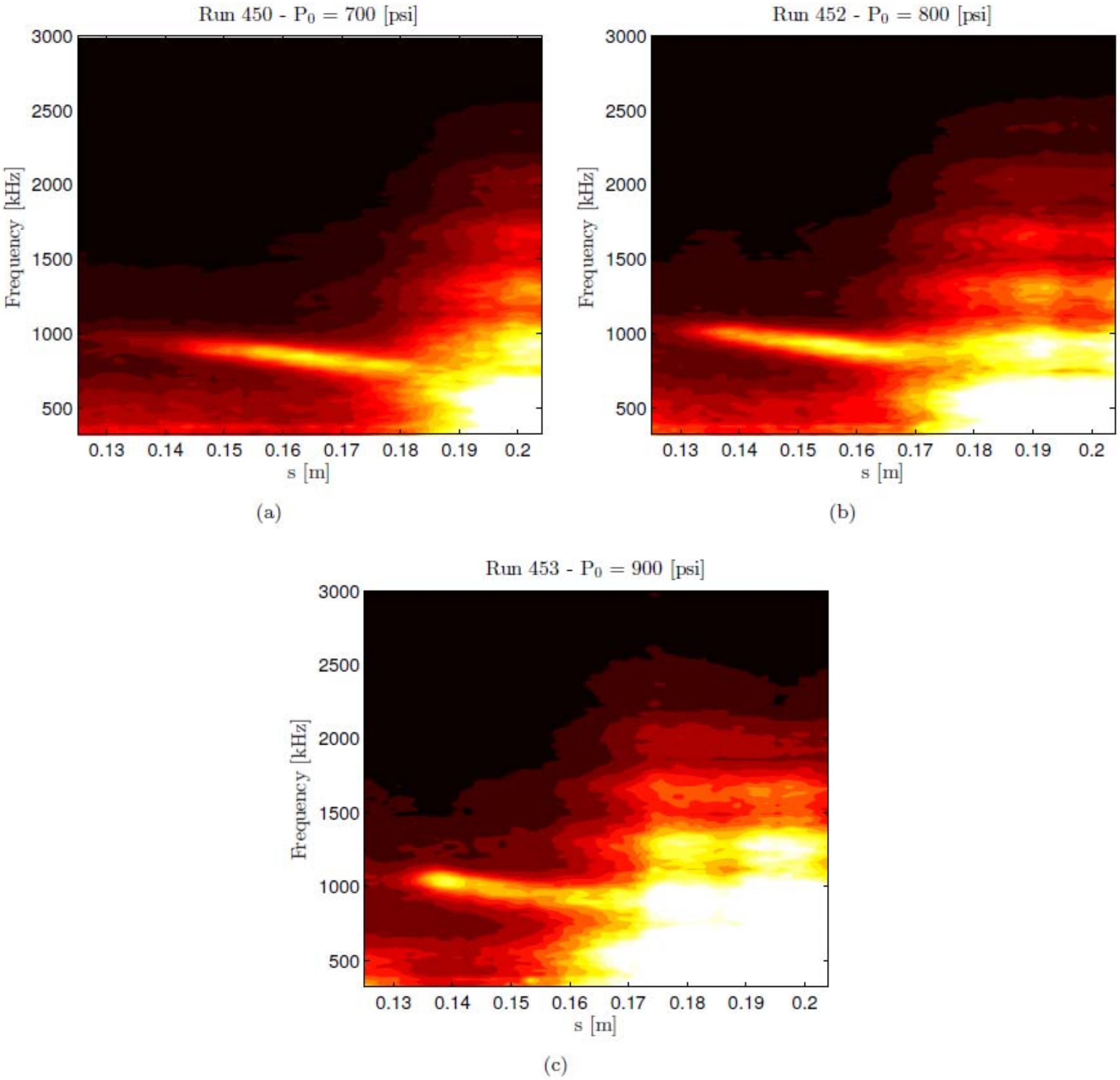

(a)

(b)

(c)

Figure 29 Spatial development of second-mode frequencies for a) Run 450 (p0 =706.3 psi), b) Run 452 (p0 =802.1 psi), and c) Run 453 (p0 =902.6 psi).

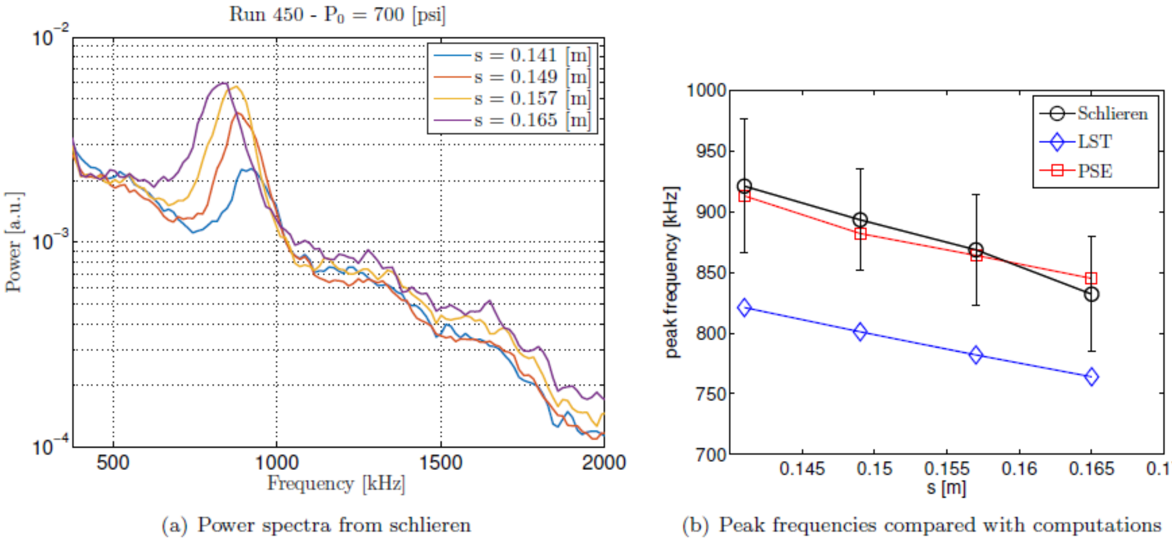

(a) Power spectra from schlieren (b) Peak frequencies compared with computations

Figure 30 Power spectra (arbitrary units) for four different streamwise locations from Run 450 (p0 =706.3 psi), and observed peak frequencies compared with LST and PST peak frequencies.

4.6. Conclusions

A strong trend in transition *N*-factor for both nose tip bluntness and swallowing length ratio is observed in the results computed. As bluntness increases and the calculated swallowing distance lengthens, the computed *N*-factor at the experimentally-observed transition location drops below the level at which Mack's second mode [109] would be expected to lead to transition. [119, 120] These results indicate that the dominant instability mechanism for the bluntest cases is likely not the second mode, which is consistent with recent blunt cone results [70] at different conditions. Alternate instability mechanisms include transient growth, [110] perhaps induced through particulate in the flow, [121] and entropy-layer instability. [111]

Based upon the computed second-mode amplification factors e^N, transition onset in the AFRL Mach 6 High Reynolds Number facility is estimated to correspond to $N \approx 7$ for the sharp and nearly sharp cases.

These amplification values are high as compared to the more typical value of $N \approx 5$–6 usually characterizing a noisy tunnel, [122] but are consistent with previous results reported in the same facility by Jewell and Kimmel. [64]

High-speed schlieren visualizations were acquired, and disturbance propagation speeds for second mode wavepackets at several cases with $R_N = 0.508$ mm (1%) were calculated by cross-correlating video frames. Spectra were also computed from the same images. These results represent the thinnest boundary layers (0.50 mm and smaller), and highest frequencies (~1 MHz), at which this technique has been applied to date. The observed peak disturbance frequencies agree well with the predicted peak *N*-factor disturbance frequencies as computed by PSE-Chem.

List of Acronyms, Abbreviations, Symbols
f = frequency, units as noted
h = convective heating coefficient, or altitude (meters) as noted
$h_{F\text{-}R}$ = reference convective heating coefficient
k = roughness height
M = Mach number, dimensionless
N = dimensionless disturbance amplitude, ln(A/A_0), where A_0 is amplitude at lower neutral bound
p = pressure, Pa
$\bar{p}$ = averaged pressure
Re = freestream unit Reynolds number, per meter
$\mathrm{R_N}$ = nose radius, units as noted
$\mathrm{Re_e}$ = unit Reynolds number based on boundary layer edge conditions, per meter
$\mathrm{Re_{RN}}$ = Reynolds number based on freestream (upstream of bow shock) conditions and nose radius
$\mathrm{Re_x}$ = Reynolds number based on freestream (upstream of bow shock) conditions and axial length
$\mathrm{Re_{x,tr}}$ = transition Reynolds number based on freestream (upstream of bow shock) conditions and axial length
s = surface coordinate perpendicular to cylinder axis in definition of h*, or streamwise surface arc length on model surface, m
T_w = wall temperature, K
T_0 = stagnation temperature, K
t = time, seconds
U = velocity, m/s
x = axial length, units as noted
Δy^+ = normalized grid spacing normal to model surface, nondimensional
z = spanwise distance, units as noted
x_T = transition location, meters

α = angle-of-attack, degrees
α_ι = instability amplification rate, units as noted
η^* = similarity length scale for swept cylinder based on attachment line boundary-layer edge density and viscosity and velocity gradient, meters

Φ = azimuthal coordinate in wind-fixed reference frame, degrees
ϕ = azimuthal coordinate in body-fixed coordinate system, degrees
ρ = density, kg/m^3
σ = standard deviation, units as noted

Subscripts
B = blunt
CFD=computed pressure at sensor location
e = evaluated at boundary layer edge
F = measured at transducer
i = index number

n = nose
r = recovery value
S = sharp
sw = swallowing
T = transition
tr = transition
w = wall
0 = stagnation conditions
∞ = free stream, upstream of model bow shock
* = evaluated at reference temperature

Acronyms

ACE	Actively-Controlled Expansion
AEDC	Arnold Engineering Development Complex
AFRL	Air Force Research Laboratory
AoA	angle of attack
BAM6QT	Boeing/AFOSR Mach 6 Quiet Wind Tunnel
BEA	Best estimated atmosphere
BET	Best estimated trajectory
CFD	computational fluid dynamics
CUBRC	Calspan / University of Buffalo Research Center
DPLR	Data Parallel-Line Relaxation
GPS	global positioning system
HIFiRE	Hypersonic International Flight Research Experiments
HT	heat transfer (heat transfer gauge identifier)
IMU	inertial measurement unit
IR	infrared
LaRC	Langley Research Center
LENS	Large Enthalpy National Shock Tunnel
LST	linear stability theory
NASA	National Aeronautics and Space Administration
PSE	parabolized stability equation
TSP	temperature-sensitive paint
TZM	titanium zirconium molybdenum
VKF	von Karman facility

End Notes

1 Kimmel, R. L., Adamczak, D. W., Borg, M. P., Jewell, J. S., Juliano, T. J., Stanfield, S., and Berger, K. T., "HIFiRE-1 and -5 Flight and Ground Tests, AIAA paper 2018-0056, January 2018. DOI: 10.2514/6.2018-0056

2 Tufts, M. W., Borg, M. P., Gosse, R. C., and Kimmel, R. L., "Collaboration Between Flight Test, Ground Test, and Computation on HIFiRE-5," AIAA paper 2018- 3807, June 2018. DOI: 10.2514/6.2018-3807

3 Jewell, J. S., Kennedy, R. E., and Laurence, S. J. and Kimmel, R. L., "Transition on a Variable Bluntness 7-Degree Cone at High Reynolds Number," AIAA paper 2018-1822

4 Dolvin, D. "Hypersonic International Flight Research and Experimentation (HIFiRE) Fundamental Science and Technology Development Strategy," AIAA Paper 2008-2581, April 2008. DOI: 10.2514/6.2008-2581

5 Dolvin, D. J., "Hypersonic International Flight Research and Experimentation Technology Development and Flight Certification Strategy," AIAA paper 2009-7228, October 2009. DOI: 10.2514/6.2009-7228

6 Kimmel, R. L., Adamczak, D., Gaitonde, D., Rougeux, A., Hayes, J. R., "HIFiRE-1 Boundary Layer Transition Experiment Design," AIAA paper 2007-0534, January 2007. DOI: 10.2514/6.2007-534

7 Wadhams, T. P., MacLean, M. G., Holden, M.S., and Mundy, E., "Pre-Flight Ground Testing of the Full-Scale FRESH FX-1 at Fully Duplicated Flight Conditions," AIAA paper 2007-4488, June 2007. DOI: 10.2514/6.2007-4488

8 Johnson, H. B., Alba, C. R., Candler, G. V., MacLean, M., Wadhams, T, and Holden, M. "Boundary Layer Stability Analysis of the Hypersonic International Flight Research Transition Experiments," *AIAA Journal of Spacecraft and Rockets*, vol. 45, no. 2, March-April 2008, pp. 228-236. DOI: 10.2514/1.31878

9 Holden, M. S., Wadhams, T. P., MacLean, M., "Experimental Studies in the LENS Supersonic and Hypersonic Tunnels for Hypervelocity Vehicle Performance and Code Validation," AIAA paper 2008-2505, April 2008. DOI: 10.2514/6.2008-2505

10 Kimmel, R. L., "Aerothermal Design for the HIFiRE-1 Flight Vehicle," AIAA paper 2008-4034, June 2008. DOI: 10.2514/6.2008-4034

11 Casper, K. M., Wheaton, B. M., Johnson, H. B., and Schneider, S. P., "Effect of Freestream Noise on Roughness-Induced Transition at Mach 6," AIAA paper 2008-4291 June 2008. DOI: 10.2514/6.2008-4291

12 Casper, K. M., Johnson, H. B., and Schneider, S. P., "Effect of Freestream Noise on Roughness-Induced Transition for a Slender Cone," *AIAA Journal of Spacecraft and Rockets*, vol. 48, no. 3, May-June 2011, pp 406-413. DOI: 10.2514/1.48300

13 Kimmel, R. L., "Roughness Considerations for the HIFiRE-1 Vehicle," AIAA Paper 2008-4293, June 2008. DOI: 10.2514/6.2008-4293

14 Alba, C. R., Johnson, H. B., Bartkowicz, M. D., Candler, G. V., and Berger, K. T. "Boundary-Layer Stability Calculations for the HIFiRE-1 Transition Experiment," *AIAA Journal of Spacecraft and Rockets*, vol. 45, no. 6, November-December 2008, pp. 1125-1133. DOI: 10.2514/1.37445

15 Wadhams, T. P., Mundy, E., MacLean, M. G., and Holden, M. S., "Ground Test Studies of the HIFiRE-1 Transition Experiment Part1: Experimental Results," *AIAA Journal of Spacecraft and Rockets*, vol. 45, no. 6, November-December 2008, pp. 1134-1148. DOI: 10.2514/1.38338

16 MacLean, M., Wadhams, T., Holden, M., and Johnson, H., "Ground Test Studies of the HIFiRE-1 Transition Experiment Part 2: Computational Analysis," *AIAA Journal of Spacecraft and Rockets*, vol. 45, no. 6, November-December 2008, pp. 1149-1164. DOI: 10.2514/1.37693

17 Berger, K. T., Greene, F. A., Kimmel, R. L., Alba, C., and Johnson, H., "Erratum on Aerothermodynamic Testing and Boundary-Layer Trip Sizing of the HIFiRE Flight 1 Vehicle," *AIAA Journal of Spacecraft and Rockets*, vol. 46, no., 2, March-April, 2009, pp. 473-480. DOI: 10.2514/1.43927

18 Adamczak, D., Alesi, H., Frost, M., "HIFiRE-1: Payload Design, Manufacture, Ground Test, and Lessons Learned," AIAA paper 2009-7294, October 2009. DOI: 10.2514/6.2009-7294

19 Kimmel, R. L., Adamczak, D., Paull, A., Paull, R., Shannon, J., Pietsch, R., Frost, M., and Alesi, H., "HIFiRE-1 Ascent-Phase Boundary-Layer Transition," *AIAA Journal of Spacecraft and Rockets*, vol. 52, no. 1, Jan-Feb 2015, pp 217-230. DOI: 10.2514/1.A32851

20 Stanfield, S. A., Kimmel, R. L., Adamczak, D. and Juliano, T. J., "HIFiRE-1 Data Analysis: Boundary Layer Transition Experiment During Reentry," *AIAA Journal of Spacecraft and Rockets*, vol. 52, no. 3, May-June 2015, pp 637-649. DOI: 10.2514/1.A33197

21 Kimmel, R. L., Adamczak, D. A., and DSTG AVD Brisbane Team, "HIFiRE-5b Flight Overview," AIAA paper 2017-3131, June 2017. DOI: 10.2514/6.2017-3131

22 Porter, K. M., Poggie, J., and Kimmel, R. L., "Laminar and Turbulent Flow Calculations for the HIFiRE-5b Flight Test," AIAA paper 2017-3132, June 2017. DOI: 10.2514/6.2017-3132

23 Jewell, J. S., Kimmel, R. L., Poggie, J., Porter, K. M., and Juliano, T. J., "Correlation of HIFiRE-5b Flight Data With Computed Pressure and Heat Transfer for Attitude Determination," AIAA paper 2017-3133, June 2017. DOI: 10.2514/6.2017-3133

24 Juliano, T., Poggie, J., Porter, K., Jewell, J., Kimmel, R.L., Adamczak, D. A., "HIFiRE-5B Heat Flux and Boundary-Layer Transition," AIAA paper 2017-3134, June 2017. DOI: 10.2514/6.2017-3134

25 Borg, M. and Kimmel, R. L., "Ground Test Measurements of Boundary-Layer Instabilities and Transition for HIFiRE-5 at Flight-Relevant Attitudes," AIAA paper 2017-3135, June 2017. DOI: 10.2514/6.2017-3135

26 Tufts, M. P., Gosse, R., and Kimmel, R. L., "PSE Analysis of Crossflow Instability on HIFiRE 5b Flight Test," AIAA paper 2017-3136, June 2017. DOI: 10.2514/6.2017-3136

27 Choudhari, M., Chang, C.-L., Jentink, T., Li, F., Berger, K., Candler, G., and Kimmel, R., "Transition Analysis for the HIFiRE-5 Vehicle," AIAA paper 2009-4056, June 2009. DOI: 10.2514/6.2009-4056

28 Gosse, R., Kimmel, R., and Johnson, H. B., "Study of Boundary-Layer Transition on Hypersonic International Flight Research Experimentation 5," *AIAA Journal of Spacecraft and Rockets*, vol. 51, no. 1, January 2014, pp 151-162. DOI: 10.2514/1.A32371

29 Juliano, T. J., Schneider, S., "Instability and Transition on the HIFiRE-5 in a Mach 6 Quiet Tunnel," AIAA paper 2010-5004, June 2010. DOI: 10.2514/6.2010-5004

30 Juliano, T. J., "Instability and Transition on the Hifire-5 in A Mach-6 Quiet Tunnel," Ph.D. Dissertation, Purdue University, West Lafayette, IN, August 2010.

31 Holden, M. S., Wadhams, T. P., MacLean, M., Mundy, E., "Review of Studies of Boundary Layer Transition in Hypersonic Flows Over Axisymmetric And Elliptic Cones Conducted in the CUBRC Shock Tunnels," AIAA paper 2009-0782, January 2009. DOI: 10.2514/6.2009-782

32 Borg, M., Kimmel, R. L., and Stanfield, S., "Instability and Transition for HIFiRE-5 in a Hypersonic Quiet Wind Tunnel," 2011-3247, June 2011. DOI: 10.2514/6.2011-3247

33 Borg, M. P., Kimmel, R. L., Stanfield, S., "Crossflow Instability for HIFiRE-5 in a Quiet Hypersonic Wind Tunnel," AIAA paper 2012-2821, June 2012. DOI: 10.2514/6.2012-2821

34 Borg, M. P., Kimmel, R. L., and Stanfield, S., "Traveling Crossflow Instability for HIFiRE-5 in a Quiet Hypersonic Wind Tunnel," AIAA 2013-2737, June 2013. DOI: 10.2514/6.2013-2737

35 Borg, M. P., Kimmel, R. L., Hofferth, J. W., Bowersox, R. D., and Mai, C. L., "Freestream Effects on Boundary Layer Disturbances for HIFiRE-5," Paper 2015-0278, AIAA, January 2015. DOI: 10.2514/6.2015-0278

36 Borg, M. P., and Kimmel, R. L., “Traveling Crossflow Instability for the HIFiRE-5 Elliptic Cone,” *AIAA Journal of Spacecraft and Rockets*, vol. 52, no. 3, May-June 2015, pp. 664-673. DOI: 10.2514/1.A33145

37 Borg, M.P., and Kimmel, R. L., “Simultaneous Infrared and Pressure Measurements of Crossflow Instability Modes for HIFiRE-5,” AIAA paper 2016-0354, January 2016. DOI: 10.2514/6.2016-0354

38 Borg, M. P., and Kimmel, R. L., “Measurements of Crossflow Instability Modes for HIFiRE-5 at Angle of Attack,” AIAA paper 2017-1681, January 2017. DOI: 10.2514/6.2017-1681

39 Berger, K. T., Rufer, S. J., Kimmel, R. and Adamczak, D., “Aerothermodynamic Characteristics of Boundary Layer Transition and Trip Effectiveness of the HIFiRE Flight 5 Vehicle,” AIAA paper 2009-4055, June 2009. DOI: 10.2514/6.2009-4055

40 Lakebrink, M. T., Borg, M. P., “Traveling Crossflow Wave Predictions on the HIFiRE-5 at Mach 6: Stability Analysis vs. Quiet Tunnel Data,” AIAA paper 2016-0356, January 2016. DOI: 10.2514/6.2016-0356

41 Kimmel, R. L, Adamczak, D., Berger, K., and Choudhari, M., “HIFiRE-5 Flight Vehicle Design,” AIAA paper 2010-4985, June 2010. DOI: 10.2514/6.2010-4985

42 Juliano, T. J., Borg, M. P. and Schneider, S. P., “Quiet Tunnel Measurements of HIFiRE-5 Boundary-Layer Transition,” *AIAA Journal*, vol. 53, no. 4, April 2015, pp.832-846. DOI: 10.2514/1.J053189

43 Dinzl, D. J. and Candler, G. V., “Direct Simulation of Hypersonic Crossflow Instability on an Elliptic Cone,” *AIAA J.*, vol. 55, no. 6, June 2017, pp. 1769-1782. DOI: 10.2514/1.J055130

44 Kimmel, R. L., Adamczak, D., Juliano, T. J., DSTO AVD Brisbane Team, “HIFiRE-5 Flight Test Preliminary Results,” AIAA paper 2013-0377, January 2013. DOI: 10.2514/6.2013-377

45 Juliano, T. J., Adamczak, D. and Kimmel, R. L., “HIFiRE-5 Flight Test Heating Analysis,” AIAA paper 2014-0076, January 2014. DOI: 10.2514/6.2014-0076

46 Jewell, J.S., Miller, J.H. and Kimmel. R.L., "Correlation of HIFiRE-5a Flight Data With Computed Pressure and Heat Transfer." *AIAA Journal of Spacecraft and Rockets*, Vol. 54, No. 5, pp. 1142-1152, 2017. DOI: 10.2514/1.A33725

47 Juliano, T. J., Adamczak, D., and Kimmel, R. L., “HIFiRE-5 Flight Test Results,” *AIAA Journal of Spacecraft and Rockets*, vol. 52, no. 3, 2015, pp. 650-663. DOI: 10.2514/1.A33142

48 Schneider, S. P., “Flight Data for Boundary-Layer Transition at Hypersonic and Supersonic Speeds,” *AIAA Journal of Spacecraft and Rockets*, vol. 36, no. 1, January-February 1999, pp 8-20. DOI: 10.2514/2.3428

49 Kimmel, R. L., and Poggie, J., "Transition on an Elliptic Cone at Mach 8," American Society of Mechanical Engineers ASME FEDSM97-3111, June 1997.

50 Kimmel, R. L., and Poggie, J., "Three-Dimensional Hypersonic Boundary Layer Stability and Transition," Air Force Research Laboratory Technical Report, WL-TR-97-3111, December 1997, Wright-Patterson Air Force Base, Ohio.

51 Kimmel, R. L., and Poggie, J., Schwoerke, S. N., "Laminar-Turbulent Transition in a Mach 8 Elliptic Cone Flow," *AIAA Journal*, vol. 37, no. 9, Sep. 1999, pp. 1080-1087. DOI: 10.2514/2.836

52 Schmisseur, J. D., "Receptivity of the Boundary Layer on a Mach-4 Elliptic Cone to Laser-Generated Localized Freestream Perturbations," Doctoral Dissertation, Purdue University Aerospace Sciences Laboratory, December 1997.

53 Holden, M., "Experimental Studies of Laminar, Transitional, and Turbulent Hypersonic Flows Over Elliptic Cones at Angle of Attack," Air Force Office of Scientific Research Technical Report AFRL-SR-BL-TR-98-0142, Bolling Air Force Base, DC, 1998.

54 Schmisseur, J. D., Schneider, S. P., and Collicott, S. H., "Receptivity of the Mach 4 Boundary Layer on an Elliptic Cone to Laser-Generated Localized Freestream Perturbations," AIAA paper 1998-0532, January 1998. DOI: 10.2514/6.1998-532

55 Schmisseur, J. D., Schneider, S. P., and Collicott, S. H., "Response of the Mach 4 boundary layer on an elliptic cone to laser-generated freestream perturbations," AIAA paper 1999-0410, January 1999. DOI: 10.2514/6.1999-410

56 Lyttle, I. J., and Reed, H. L., "Use of Transition Correlations for Three-Dimensional Boundary Layers Within Hypersonic Flows," AIAA-95-2293, June 1995. DOI: 10.2514/6.1995-2293

57 Li, F., Choudhari, M., Chang, C.-L., Kimmel, R., Adamczak, D., and Smith, M., "Transition Analysis for the Ascent Phase of HIFiRE-1 Flight Experiment," *AIAA Journal of Spacecraft and Rockets*, vol. 52, no. 5, September-October 2015, pp. 1283-1293. DOI: 10.2514/1.A33258

58 Johnson, H. B., Candler, G. V., "Analysis of Laminar-Turbulent Transition in Hypersonic Flight Using PSE-Chem," AIAA paper 2006-3057, June 2006. DOI: 10.2514/6.2006-3057

59 Malik, M. R., "Hypersonic Flight Transition Data Analysis Using Parabolized Stability Equations with Chemistry Effects," *AIAA Journal of Spacecraft and Rockets*, Vol. 40, No. 3, May-June 2003, pp 332-344. DOI: 10.2514/2.3968

60 Bushnell, D., "Notes on Initial Disturbances Fields for the Transition Problem," *Instability and Transition*, Vol. 1, edited by M. Y. Hussaini, and R. G. Voigt, Springer–Verlag, Berlin, 1990, pp. 217–232.

61 Fedorov, A. and Tumin, A., "Receptivity of High-Speed Boundary Layers to Kinetic Fluctuations, *AIAA Journal*, vol. 55, no. 7, July, 2017, pp. 2335-2348. DOI: 10.2514/1.J055326

62 Marineau for 2nd Mode Dominated Boundary Layer Transition in Hypersonic Wind Tunnels," *AIAA Journal*, vol. 55, no. 2, Feb. 2017, pp. 484-499. DOI: 10.2514/1.J055061

63 Stetson, K. F., "Nosetip Bluntness Effects on Cone Frustum Boundary Layer Transition in Hypersonic Flow," AIAA paper 83-1763, July 1983. DOI: 10.2514/6.1983-1763

64 Jewell, J. S., and Kimmel, R. L., "Boundary Layer Stability Analysis for Stetson's Mach 6 Blunt Cone Experiments," *AIAA Journal of Spacecraft and Rockets*, vol. 54, no. 1, January-February 2017, pp. 258-265.

65 Stetson, K. F., "Mach 6 Experiments of Transition on a Cone at Angle of Attack," *AIAA Journal of Spacecraft and Rockets*, vol. 19, no. 5, Sep.-Oct. 1982, pp. 397-403. DOI: 10.2514/3.62276

66 Willems, S., Gülhan, A., Juliano, T. J., and Schneider, S. P., "Laminar to turbulent transition on the HIFiRE-1 cone at Mach 7 and high angle of attack," AIAA 2014-0428, January 2014. DOI: 10.2514/6.2014-0428

67 Juliano, T. J., Kimmel, R. L., Willems, S. Gülhan, A., and Schneider, S. P., "HIFiRE-1 Surface Pressure Fluctuations from High Reynolds, High Angle Ground Test," AIAA paper 2014-0429, January 2014. DOI: 10.2514/6.2014-0429

68 Juliano, T. J., Kimmel, R. L., Willems, S., Gülhan, A., and Wagnild, R. M., "HIFiRE-1 Boundary-Layer Transition: Ground Test Results and Stability Analysis," AIAA-2015-1736, 2015. DOI: 10.2514/6.2015-1736

69 Stetson, K. F., and Rushton, G. H., "Shock Tunnel Investigation of Boundary-Layer Transition at M=5.5," *AIAA Journal*, vol. 5, no. 5, May 1967, pp. 899-906. DOI: 10.2514/3.4098

70 Marineau, E. C., Moraru, C. G., Lewis, D. R., Norris, J. D., Lafferty, J. L., Wagnild, R. M., and Smith, J. A., "Mach 10 Boundary-Layer Transition Experiments on Sharp and Blunted Cones," AIAA paper 2014-3108, June 2014. DOI: 10.2514/6.2014-3108

71 Holden, M. S., "Experimental Studies of the Effects of Asymmetric Transition on the Aerothermal Characteristics of Hypersonic Blunted Slender Cones," AIAA paper 1985-0325, January 1985. DOI: 10.2514/6.1985-325

72 Schneider, S. P., "Effects of High-Speed Tunnel Noise on Laminar-Turbulent Transition," *Journal of Spacecraft and Rockets*, vol. 38, no. 3, May-June 2001, pp. 323-333. DOI: 10.2514/2.3705

73 Holden, M. S., Bower, D., and Chadwick, K., "Measurements of Boundary Layer Transition on Cones at Angle of Attack for Mach Numbers from 11 to 13," AIAA 95-2294, June 1995. DOI: 10.2514/6.1995-2294

74 DiCristina, V., "Three-Dimensional Boundary Layer Transition on a Sharp 8o Cone at Mach 10," *AIAA Journal*, vol. 8, no. 5, May 1970, pp. 852-856. DOI: 10.2514/3.5777

75 Creel, T. R., Beckwith, I. E., and Chen, F. J., "Transition on Swept Leading Edges at Mach 3.5," *AIAA J. Aircraft*, vol. 24, no. 10, Oct. 1987, pp. 710-717. DOI: 10.2514/3.45511

76 Gosse, R., and Kimmel, R., "CFD Study of Three-Dimensional Hypersonic Laminar Boundary Layer Transition on a Mach 8 Elliptic Cone," AIAA paper 2009-4053, June 2009. DOI: 10.2514/6.2009-4053

77 Lakebrink, M. T., "Numerical Investigation of Crossflow Instability on the HIFiRE-5," Ph. D. dissertation, Purdue University, West Lafayette, Indiana, 2016.

78 Kimmel, R. L., Adamczak, D. A., Hartley, D., Alesi, H., Frost, M. A., Pietsch, R. Shannon, J. and Silvester, T., "HIFiRE-5b Flight Overview," accepted for publication, *AIAA Journal of Spacecraft and Rockets*.

79 Neel, I. T., Leidy, A. N. and Bowersox, R. D. W., "Preliminary Study of the Effect of Environmental Disturbances on Hypersonic Crossflow Instability on the HIFiRE-5 Elliptic Cone," AIAA paper 2017-0767, January 2017. DOI: 10.2514/6.2017-0767

80 Stetson, K. F., Thompson, E. R., Donaldson, J. C., and Siler, L. G., "Laminar Boundary Layer Stability Experiments on a Cone at Mach 8, Part 4: on Unit Reynolds Number and Environmental Effects," AIAA paper 1986-1087, May 1986. DOI: 10.2514/6.1986-1087

81 Li, F., Choudhari, M., Chang, C.-L., White, J., Kimmel, R., Adamczak, D., Borg, M., Stanfield, S., and Smith, M., "Stability Analysis for HIFiRE Experiments," AIAA paper 2012-2961, June 2012. DOI: 10.2514/6.2012-2961

82 Moyes, A. J., Kocian, T. S., Mullen, and Reed, H. L., "Boundary Layer Stability Analysis of HIFiRE-5b Flight Geometry," AIAA paper 2017-4301, June 2017. DOI: 10.2514/6.2017-4301

83 Morkovin, M. V., Reshotko, E., and Herbert, T., "Transition in open flow systems-a reassessment," *Bull. Am. Phys. Soc.*, 18 Vol. 39, No. 9, 1994, pp. 1882.

84 Reshotko, E., "Transition Issues at Hypersonic Speeds," AIAA-2006-707, 2006.

85 Reed, H. L., Reshotko, E., and Saric, W. S., "Receptivity: The Inspiration of Mark Morkovin," AIAA-2015-2471, 2015.

86 Zhong, X. and Wang, X., “Direct Numerical Simulation on the Receptivity, Instability, and Transition of Hypersonic Boundary Layers,” *Annual Rev. Fluid Mechanics*, Vol. 44, 2012, pp. 527–561.

87 Horvath, T. J., Tomek, D. M., Berger, K. T., Zalameda, J. N., Splinter, S. C., Krasa, P. W., Schwartz, R. J., Gibson, D. M., Tietjen, A. B., and S., T., “The HYTHIRM Project: Flight Thermography of the Space Shuttle During Hypersonic Re-entry,” AIAA-2010-0241, 2010.

88 Saric, W. S., West, D. E., Tufts, M. W., and Reed, H. L., “Flight Test Experiments on Discrete Roughness Element Technology for Laminar Flow Control,” AIAA-2015-0539, 2015.

89 Kocian, T. S., Moyes, A. J., Mullen, D., and Reed, H. L., “PSE and Spatial Biglobal Instability Analysis of Reduced Scale and Flight HIFiRE-5 Geometry,” AIAA-2017-0768, 2017.

90 Berry, S. A., Kimmel, R. L., and Reshotko, E., “Recommendations for Hypersonic Boundary Layer Transition Flight Testing,” AIAA-2011-3415, 2011.

91 Paredes, P., Gosse, R., Theofilis, V., and Kimmel, R. L., “Linear Modal Instabilities of Hypersonic Flow Over an Elliptic Cone,” *Journal of Fluid Mechanics*, Vol. 804, 2016, pp. 442–466, doi:10.1017/jfm.2016.536.

92 Keener, E. R. and Hopkins, E. J., “Accuracy of Pitot-Pressure Rakes for Turbulent Boundary-Layer Measurements in Supersonic Flow,” NASA Technical Note TN D-6229, 1971.

93 Bertelrud, A., de la Tova, G., Hamory, P. J., Young, R., Noffz, G. K., Dodson, M., Graves, S. S., Diamond, J. K., Noack, R., and Knoblock, D., “Pegasus Wing-Glove Experiment to Document Hypersonic Crossflow Transition – Measurement System and Selected Flight Results,” AIAA-2000-0505, 2000.

94 Berry, S. A., Chen, F.-J., Wilder, M. C., and Reda, D. C., “Boundary Layer Transition Experiments in Support of the Hypersonics Program,” AIAA-2007-4266, 2007.

95 Schneider, S. P., “Flight Data for Boundary-Layer Transition at Hypersonic and Supersonic Speeds,” *AIAA Journal of Spacecraft and Rockets*, vol. 36, no. 1, January-February 1999, pp 8-20. DOI: 10.2514/2.3428

96 Drake, A., Bender, A. M., Korntheuer, A. J., Westphal, R. V., McKeon, B. J., Geraschenko, S., Rohe, W., and Dale, G., “Step Excrescence Effects for Manufacturing Tolerances on Laminar Flow Wings,” AIAA-2010-375, January 2010.

97 Duncan Jr., G. T., Crawford, B. K., Tufts, M. W., Saric, W. S., and Reed, H. L., “Effects of Step Excrescences on Swept-Wing Transition,” AIAA-2013-2412, 2013.

98 Crawford, B. K., Duncan Jr., G. T., Tufts, M. W., Saric, W. S., and Reed, H. L., “Effects of Step-Excrescence Location on Swept-Wing Transition,” AIAA-2015-1233, January 2015.

99 Tufts, M. W., Reed, H. L., Crawford, B. K., and Duncan Jr., G. T., “Computational Investigation of Step Excrescence Sensitivity in a Swept-Wing Boundary Layer,” AIAA-2015-2775, 2015.

100 Poll, D. I. A., “The Development of Intermittent Turbulence on a Swept Attachment Line Including the Effects of Compressibility,” *The Aeronautical Quarterly*, vol. 34, Feb. 83, pp. 1-23.

101 Poll, D. I. A., “Some Observations of the Transition Process on the Windward Face of a Long Yawed Cylinder,” *Journal of Fluid Mechanics*, Vol. 150, No. 1, 1985, pp. 329–356.

102 Stetson, K. F., “Notes related to previous AIAA papers on blunt cones,” Personal communication to S. P. Schneider, December 2001, Purdue University.

103 Wright, M. J., Candler, G. V., and Bose, D., “Data-parallel line relaxation method for the Navier-Stokes equations,” *AIAA Journal* , Vol. 36, No. 9, 1998, pp. 1603–1609.

104 Johnson, H. B., Thermochemical Interactions in Hypersonic Boundary Layer Stability, Ph.D. thesis, University of Minnesota, Minneapolis, MN, 2000.

105 Johnson, H. B., Seipp, T. G., and Candler, G. V., “Numerical study of hypersonic reacting boundary layer transition on cones,” *Physics of Fluids*, Vol. 10, 1998, pp. 2676–2685.

106 Rotta, N. R., “Effects of nose bluntness on the boundary layer characteristics of conical bodies at hypersonic speeds,” New York University Report NYUAA-66-66, 1966.

107 Goodwin, D., “Cantera: An object-oriented software toolkit for chemical kinetics, thermodynamics, and transport processes,” Available: http://code.google.com/p/cantera, 2009, Accessed: 12/12/2012.

108 Johnson, H. B. and Candler, G. V., “Hypersonic boundary layer stability analysis using PSE-Chem,” 35th Fluid Dynamics Conference and Exhibit , AIAA, 2005, AIAA-2005-5023.

109 Mack, L. M., “Boundary-layer linear stability theory: Special course on stability and transition of laminar flow advisory group for aerospace research and development,” Tech. rep., 1984, AGARD Report No. 709, NATO, Neuilly sur Seine, France.

110 Reshotko, E., “Transient growth: A factor in bypass transition,” *Physics of Fluids*, Vol. 13, No. 5, 2001, pp. 1067–1075.

111 Kufner, E. and Dallmann, U., “Entropy-and Boundary Layer Instability of Hypersonic Cone Flows-Effects of Mean Flow Variations,” Laminar-Turbulent Transition, Springer, 1995, pp. 197–204.

112 Laurence, S. J., Wagner, A., and Hannemann, K., “Schlieren-based techniques for investigating instability development and transition in a hypersonic boundary layer,” *Experiments in Fluids*, Vol. 55, No. 1782, 2014.

113 Laurence, S., Wagner, A., and Hannemann, K., “Experimental study of second-mode instability growth and breakdown in a hypersonic boundary layer using high-speed schlieren visualization,” *Journal of Fluid Mechanics*, Vol. 797, 2016, pp. 471–503.

114 Kennedy, R. E., Laurence, S. J., Smith, M. S., and Marineau, E. C., “Feedback Stabilized Laser Differential Interferometry for Supersonic Blunt Body Receptivity Experiments,” AIAA SciTech 2017 , AIAA-2017-1683, Grapevine, TX, 2017.

115 Shumway, N. M. and Laurence, S. J., “Methods for Identifying Key Features in Schlieren Images from Hypersonic Boundary- Layer Instability Experiments,” Proceedings of 53rd AIAA Aerospace Sciences Meeting, AIAA-2015-1787, Orlando, FL, 2015.

116 Jewell, J. S., Leyva, I. A., and Shepherd, J. E., “Turbulent spots in hypervelocity flow,” *Experiments in Fluids*, Vol. 58, No. 32, 2017.

117 Shiplyuk, A. N., Bountin, D. A., Maslov, A. A., and Chokani, N., “Nonlinear Mechanisms of the Initial Stage of the Laminar- Turbulent Transition at Hypersonic Velocities,” *Journal of Applied Mechanics and Technical Physics*, Vol. 44, No. 5, 2003, pp. 654–659.

118 Stetson, K. F., Thompson, E. R., Donaldson, J. C., and Siler, L. G., “Laminar Boundary Layer Stability Experiments on a Cone at Mach 8, Part 1: Sharp Cone,” Proceedings of the AlAA 16th Fluid and Plasma Dynamics Conference , AIAA-83-1761, Danvers, Massachusetts, 1983.

119 Fedorov, A. V., “Receptivity of a High-Speed Boundary Layer to Acoustic Disturbances,” *Journal of Fluid Mechanics*, Vol. 491, September 2003, pp. 101–129.

120 Fedorov, A. and Tumin, A., “High-Speed Boundary-Layer Instability: Old Terminology and a New Framework,” *AIAA Journal*, Vol. 49, 2011, pp. 1647–1657.

121 Jewell, J. S., Parziale, N. J., Leyva, I. A., and Shepherd, J. E., “Effects of Shock-Tube Cleanliness on Hypersonic Boundary Layer Transition at High Enthalpy,” *AIAA Journal*, Vol. 55, No. 1, 2017, pp. 332–338.

122 Schneider, S. P., “Effects of High-Speed Tunnel Noise on Laminar-Turbulent Transition,” *AIAA Journal of Spacecraft and Rockets*, Vol. 38, No. 3, 2001, pp. 323–333.